Electronic Supplementary Information (ESI)

Underwater Luminescent Labeling Materials Constructed from Supramolecular Approach

Qiao Zhang,[a] Wenbo Wang,[a] Changyong Cai,[a] Shuanggen Wu,[a] Jialing Li,[a] Fenfang Li,[b] Shengyi Dong[a]*

[a]College of Chemistry and Chemical Engineering, Hunan University, Changsha 410082, Hunan, P. R. China.

[b]College of Chemistry and Chemical Engineering, Central South University, Changsha 410083, Hunan, P. R. China.

*Corresponding author. Email: Email: dongsy@hnu.edu.cn (S.Y.D).

Table of Contents

1. Materials and methods

All reagents were commercially available and used as supplied without further purification. **TPE**s were prepared according to the reported methods.[1,2] Tetraphenylethene (**E**) was commercially available and used as supplied without further purification. ^{1}H NMR spectra were collected on a Varian Unity INOVA-400 or Bruker-AV400 with TMS as the internal standard. Two-dimensional COSY and NOESY experiments were performed on a Bruker-A V400 MHz spectrometer. ^{13}C NMR spectra were recorded on a Bruker-AV400 spectrometer at 100 MHz. Fourier-transform IR (FT-IR) spectra were recorded on a Nicolet Avatar 320 FT-IR. Scanning electron microscopy (SEM) experiments were performed on a high-resolution HITACHI SU 8030 scanning electron microscope. Powder X-Ray diffraction (PXRD) patterns were collected in transmission mode on samples held on thin Mylar film in aluminum well plates on a Panalytical X'Pert PRO MPD equipped with a high-throughput screening XYZ stage, x-ray focusing mirror, and PIXcel detector using Ni-filtered Cu Kα radiation. Data were measured over the range of 5° to 60° in ~0.013° steps over 60 min. Thermogravimetric analysis (TGA) measurements were carried out using a TA Instruments Q5000IR analyzer with an automated vertical overhead thermobalance. The samples were heated at a rate of 10.0 °C/min in nitrogen atmosphere. Transition temperatures of materials were determined on a TA Instruments Q200F3 differential scanning calorimetry (DSC) under nitrogen. Each sample (~ 5 mg) was heated at a rate of 10 °C/min. Contact angle experiments were performed on a contact angle measuring instrument (XG-CAMC1). Rheology measurements were done on an Anton Paar MCR 92. The laminator model PP25 was chosen with a diameter of 25 mm with the gap at 0.051 mm. Dynamic mechanical analysis (DMA) experiments were performed on DMA8000. Quantitative adhesion experiments were performed on a pull-off adhesion tester with a pull rate of 100 mm/s (each adhesion test was carried out five times, HY-0580). Transmittance experiments were performed on LENS Transmission Meter (SDR 850) at 550 nm. UV-Vis spectra were recorded on a Varian Cary 50 Conc UV-Visible Spectrophotometer with Peltier. Fluorescent emission spectra were recorded on a Thermo Scientific Lumina. The solid-state fluorescent emission spectra were measured on an Edinburgh FLS1000 machine. The solid-state absolute fluorescence quantum yields were measured using an integrating sphere by an Edinburgh FLS1000 machine. Single-crystal X-ray diffraction (XRD) experiment was collected on a Rigaku Oxford Diffraction SuperNova with Atlas Diffractometer, and crystal structure was solved with Olex2. UV irradiation intensities were recorded on a photoelectric instrument (UV-A).

2. Synthetic routes of TPEs

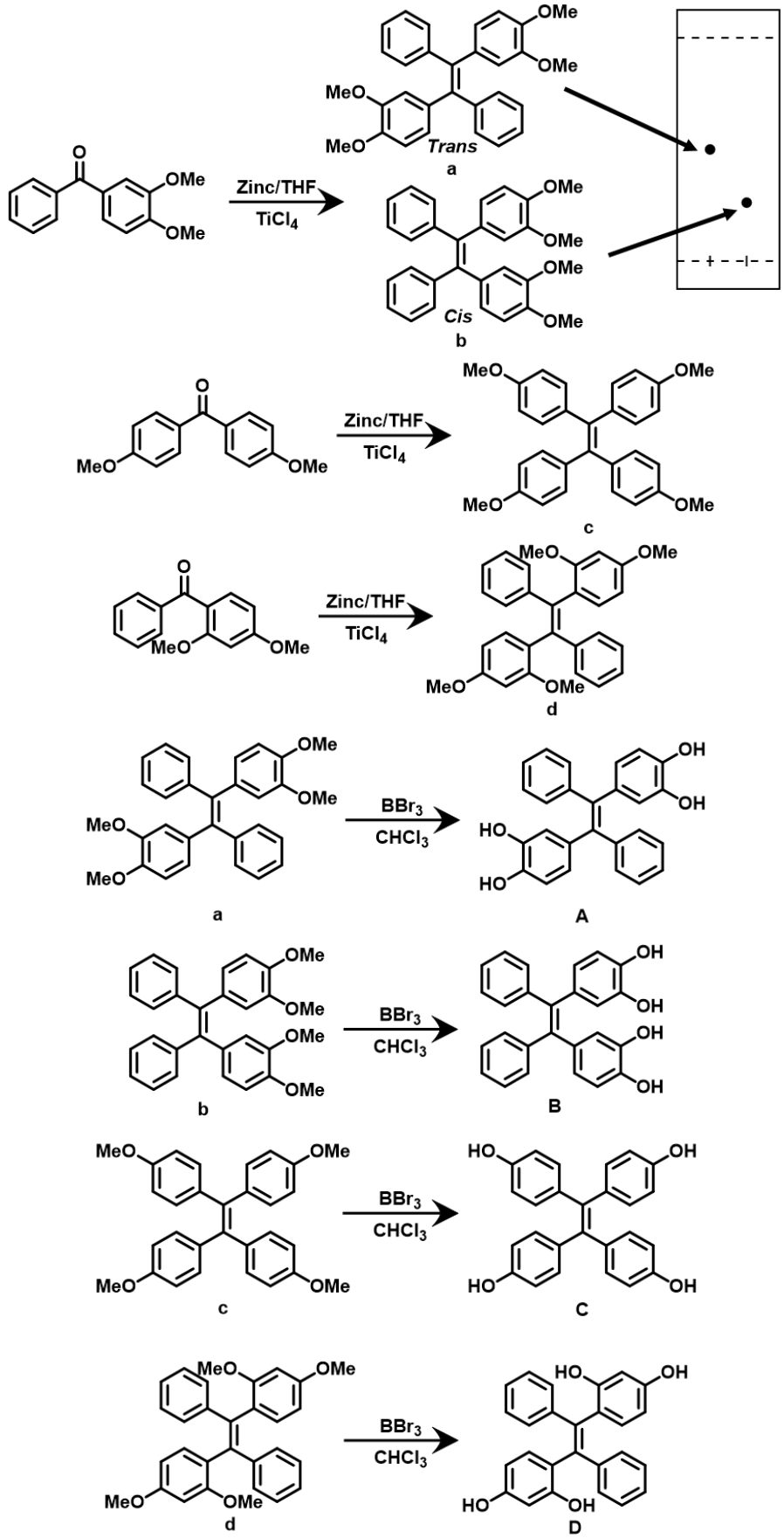

Scheme S1. Synthetic routes of **TPEs**.

a and **b** were prepared according to the reported methods.[1] Zn (14.05 g, 216.2 mmol) was dispersed in anhydrous THF (250 mL) in a 500 mL three-neck flask and cooled in an ice bath. To it, $TiCl_4$ (24 mL) was added dropwise. Thereafter, the ice-bath was removed and the system was refluxed for 2 hours. (3,4-dimethoxyphenyl)(phenyl)methanone (13.09 g, 54.0 mmol) dissolved in anhydrous THF (50 mL) was added dropwise and the solution was then refluxed overnight and cooled to room temperature, poured into water (500 mL) and finally extracted with dichloromethane (3×500 mL). The organic phase was combined and dried with $MgSO_4$. The solvent was removed by rota-evaporation and the residue was purified by column chromatography (silica gel, dichloromethane/hexane = 5/1, *v*:*v*). **a** (4.10 g, yield: 33.6%) was obtained as a white powder. TLC: dichloromethane/hexane = 2/1, R_f = 0.47. **b** (2.23 g, yield: 18.3%) was obtained as a white powder. TLC: dichloromethane/hexane = 2/1, R_f = 0.33. ^{1}H NMR (400 MHz, $CDCl_3$, room temperature) of **a**: δ 7.16 – 7.07 (m, 10H), 6.62 (d, J = 8.0 Hz, 2H), 6.54 – 6.52 (m, 4H), 3.81 (s, 6H), 3.46 (s, 6H). ^{13}C NMR (100 MHz, $CDCl_3$, room temperature) of **a**: δ 147.81, 147.50, 144.24, 139.90, 136.33, 131.28, 127.82, 126.36, 123.96, 115.16, 110.23, 55.66, 55.53. ^{1}H NMR (400 MHz, $CDCl_3$, room temperature) of **b**: δ 7.10 – 7.03 (m, 10H), 6.65 (d, J = 12.0 Hz, 2H), 6.59 – 6.56 (m, 4H), 3.82 (s, 6H), 3.54 (s, 6H). ^{13}C NMR (100 MHz, $CDCl_3$, room temperature) of **b**: δ 148.15, 147.61, 143.80, 140.03, 136.77, 131.41, 127.58, 126.33, 123.86, 114.87, 110.46, 55.77, 55.70.

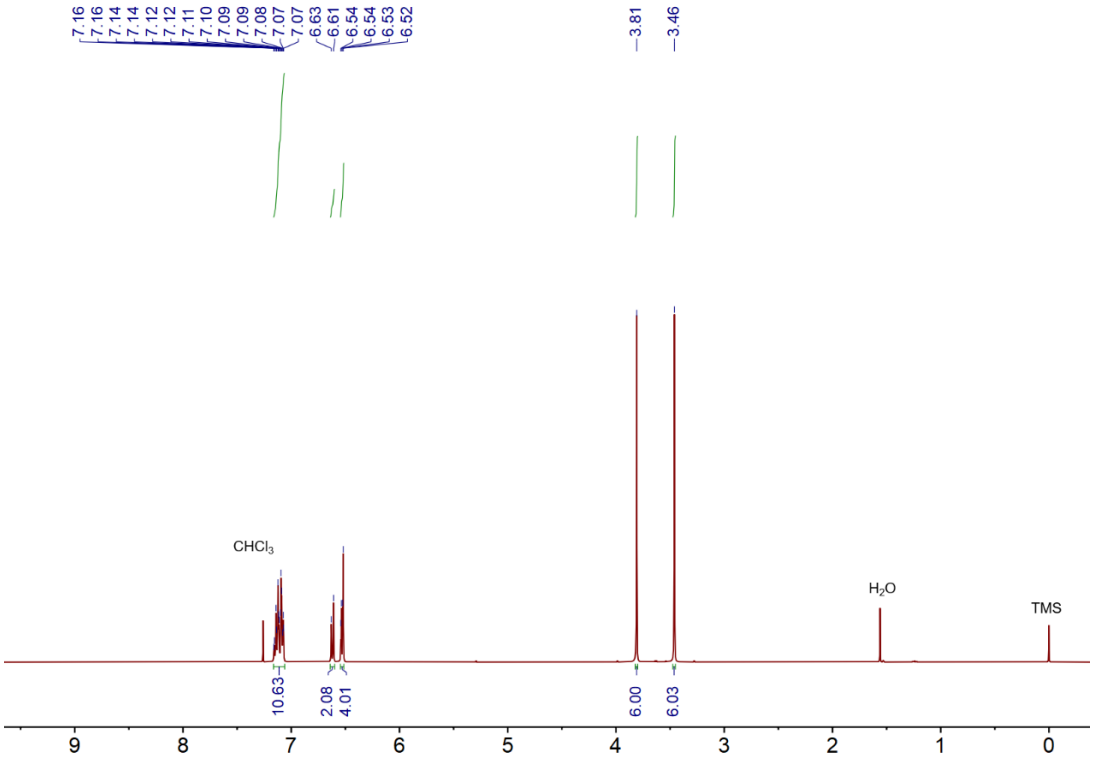

Figure S1. ^{1}H NMR spectrum (400 MHz, $CDCl_3$, room temperature) of **a**.

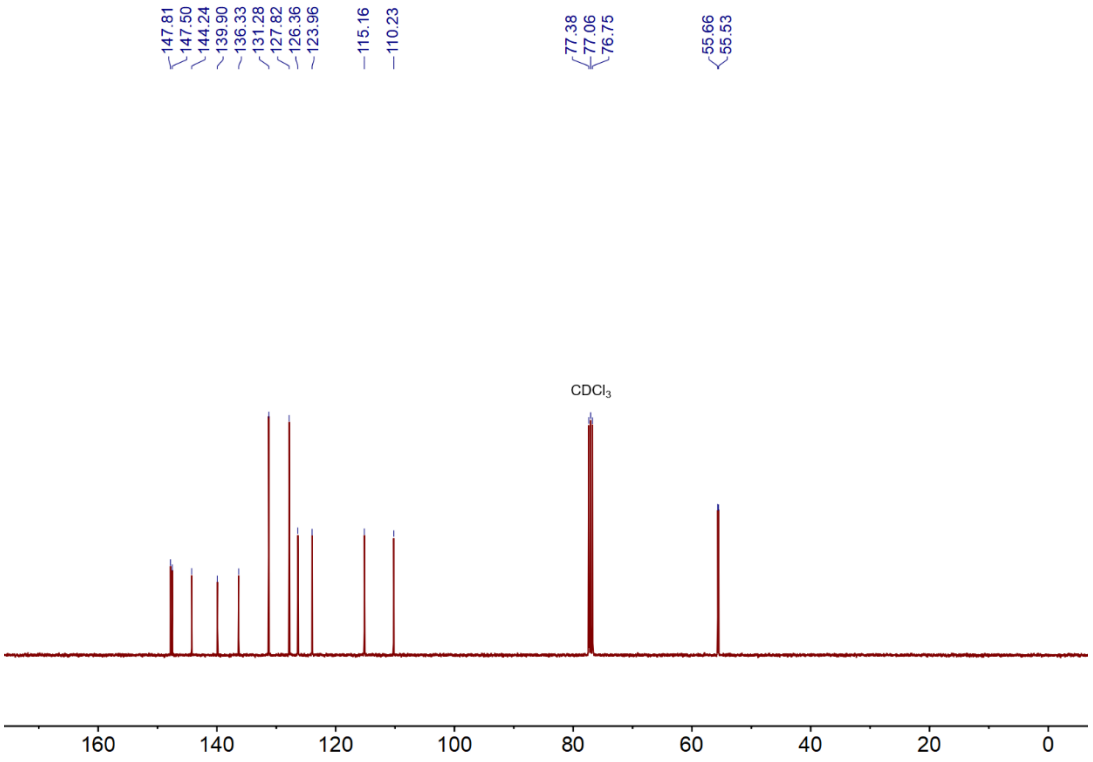

Figure S2. ^{13}C NMR spectrum (100 MHz, $CDCl_3$, room temperature) of **a**.

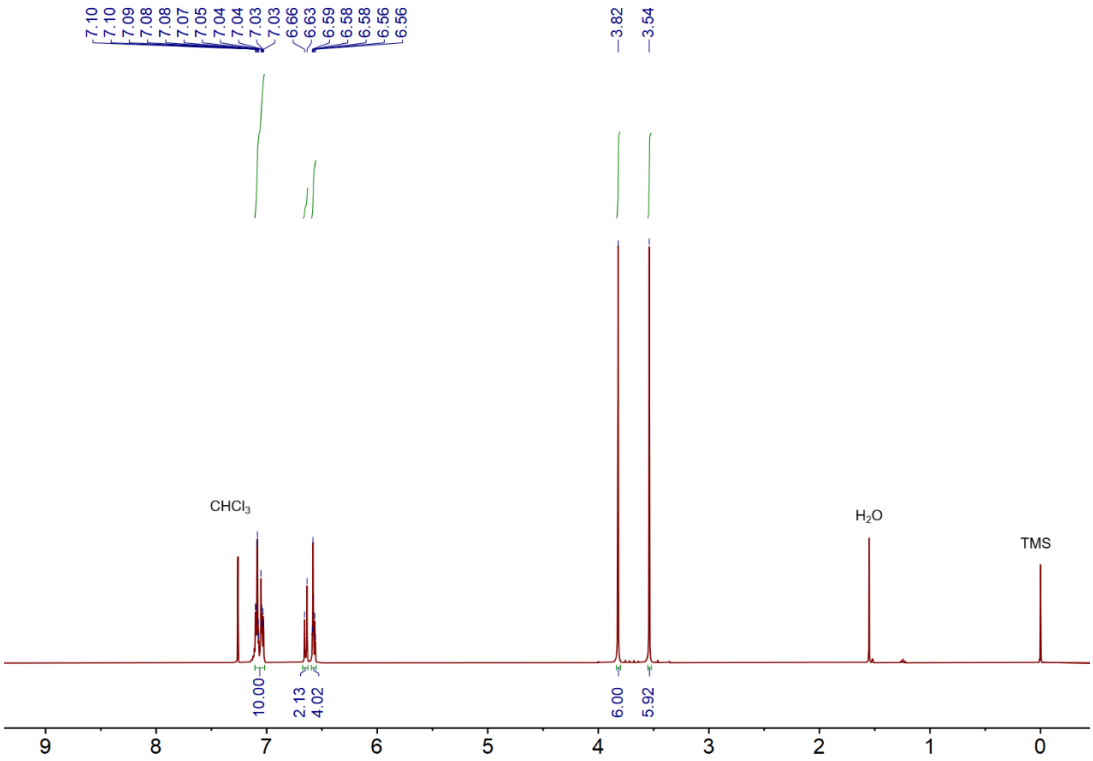

Figure S3. ^{1}H NMR spectrum (400 MHz, $CDCl_3$, room temperature) of **b**.

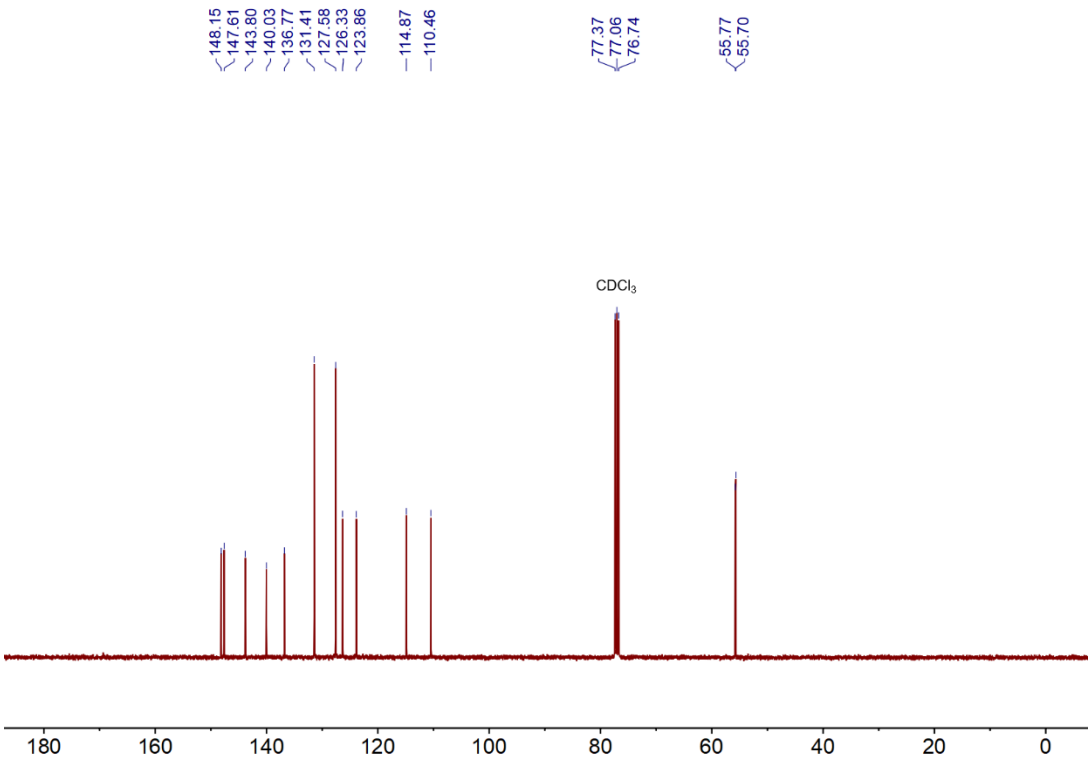

Figure S4. ^{13}C NMR spectrum (100 MHz, $CDCl_3$, room temperature) of **b**.

c was prepared according to the reported methods.[1] Zn (10.81 g, 166.3 mmol) was dispersed in anhydrous THF (250 mL) in a 500 mL three-neck flask and cooled in an ice bath. To it, $TiCl_4$ (19 mL) was added dropwise. Thereafter, the ice-bath was removed and the system was refluxed for 2 hours. Bis(4-methoxyphenyl)methanone (10.07 g, 41.6 mmol) dissolved in anhydrous THF (50 mL) was added dropwise and the solution was then refluxed overnight and cooled to room temperature, poured into water (500 mL) and finally extracted with dichloromethane (3×500 mL). The organic phase was combined and dried with $MgSO_4$. The solvent was removed by rota-evaporation and the residue was purified by column chromatography (silica gel, dichloromethane/hexane = 5/1, *v*:*v*). **c** (3.85 g, yield: 41.0%) was obtained as a white powder. TLC: dichloromethane/hexane = 1/1, R_f = 0.40. ^1H NMR (400 MHz, $CDCl_3$, room temperature) of **c**: δ 6.94 (d, J = 8.0 Hz, 8H), 6.65 (d, J = 8.0 Hz, 8H), 3.75 (s, 12H). ^{13}C NMR (100 MHz, $CDCl_3$, room temperature) of **c**: δ 157.81, 138.41, 136.92, 132.56, 113.05, 55.10.

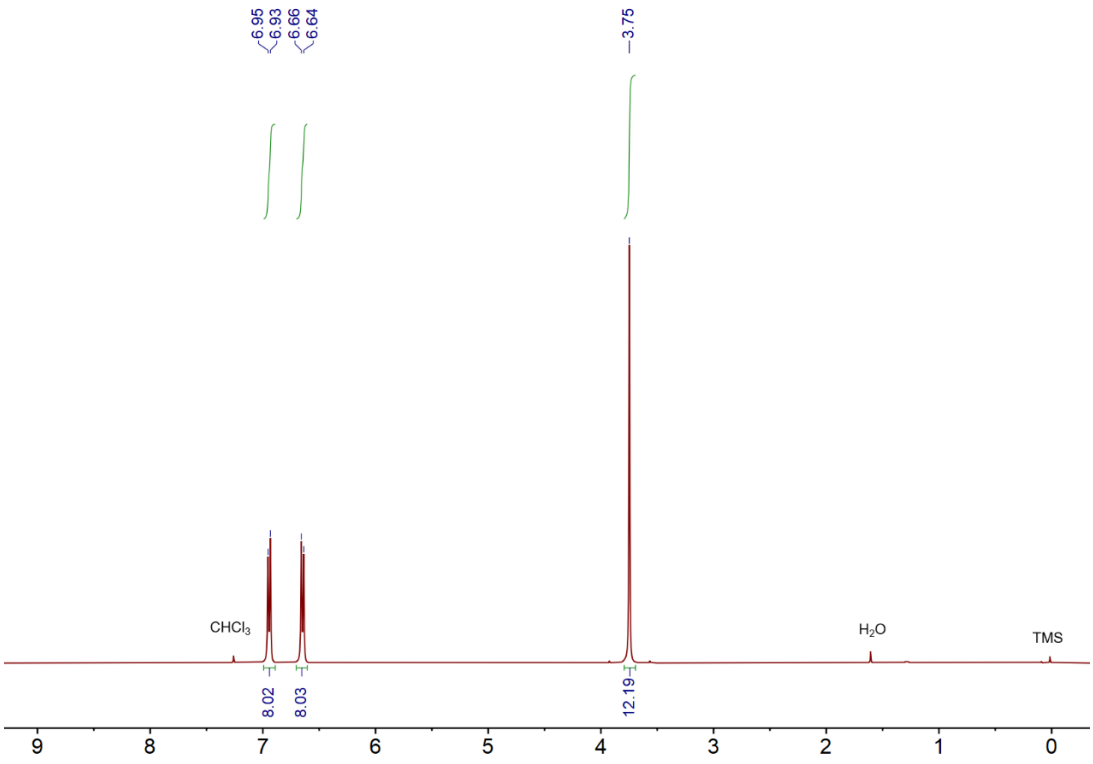

Figure S5. ^{1}H NMR spectrum (400 MHz, $CDCl_3$, room temperature) of **c**.

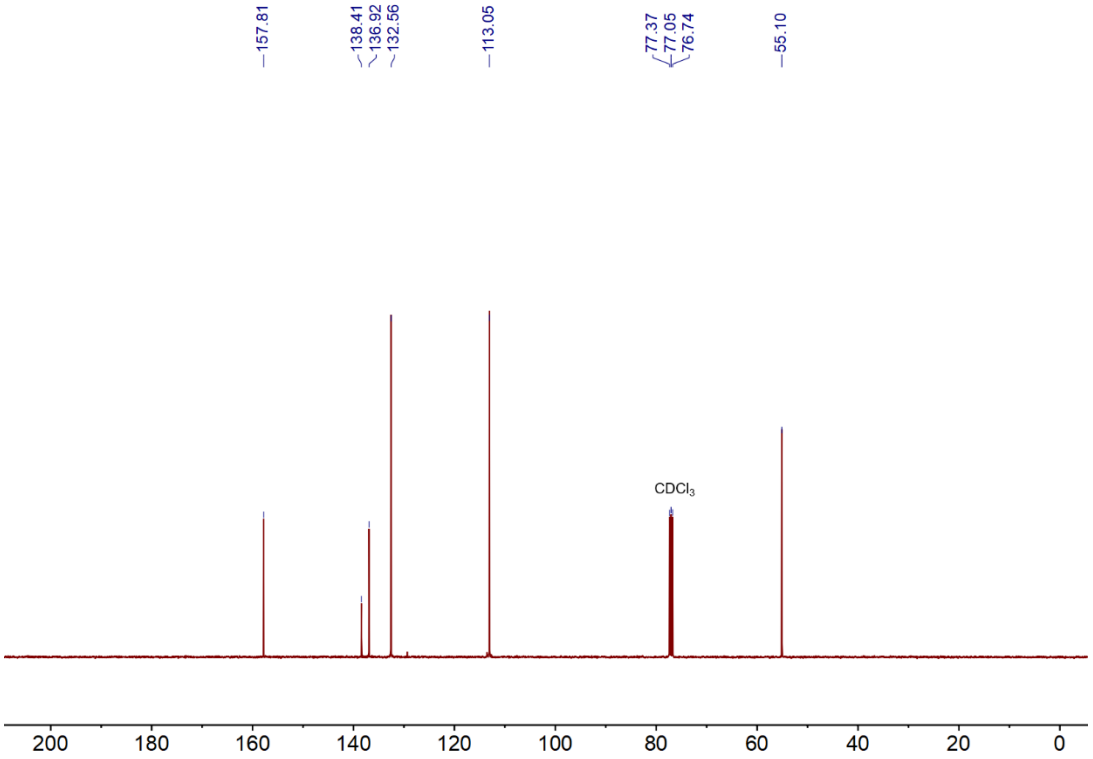

Figure S6. ^{13}C NMR spectrum (100 MHz, $CDCl_3$, room temperature) of **c**.

d was prepared according to the reported methods.[2] Zn (11.88 g, 182.8 mmol) was dispersed in anhydrous THF (250 mL) in a 500 mL three-neck flask and cooled in an ice bath. To it, $TiCl_4$ (20 mL) was added dropwise. Thereafter, the ice-bath was removed and the system was refluxed for 2 hours. (2,4-dimethoxyphenyl)(phenyl)methanone (11.07 g, 45.7 mmol) dissolved in anhydrous THF (50 mL) was

added dropwise and the solution was then refluxed overnight and cooled to room temperature, poured into water (500 mL) and finally extracted with dichloromethane (3×500 mL). The organic phase was combined and dried with $MgSO_4$. The solvent was removed by rota-evaporation and the residue was purified by column chromatography (silica gel, dichloromethane/hexane = 5/1, *v*:*v*). **d** (1.67 g, yield: 21.4%) was obtained as a white powder. TLC: dichloromethane/hexane = 1/1, R_f =0.34. ^{1}H NMR (400 MHz, $CDCl_3$, room temperature) of **d**: δ 7.04 – 7.01 (m, 10H), 6.93 (d, J = 8.0 Hz, 2H), 6.27 – 6.24 (m, 4H), 6.07 (s, 6H), 3.44 (s, 6H). ^{13}C NMR (100 MHz, $CDCl_3$, room temperature) of **d**: δ 159.62, 158.21, 143.26, 137.79, 132.01, 130.56, 127.16, 126.57, 125.68, 103.96, 98.84, 55.45, 55.17.

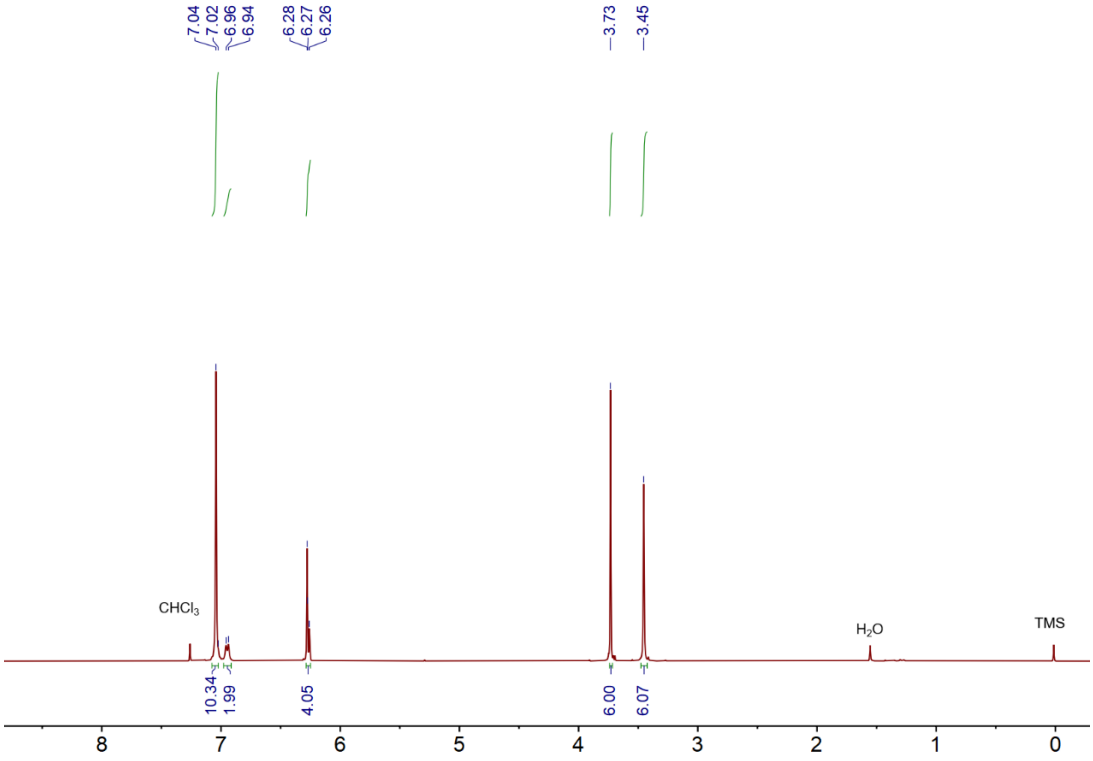

Figure S7. ^{1}H NMR spectrum (400 MHz, $CDCl_3$, room temperature) of **d**.

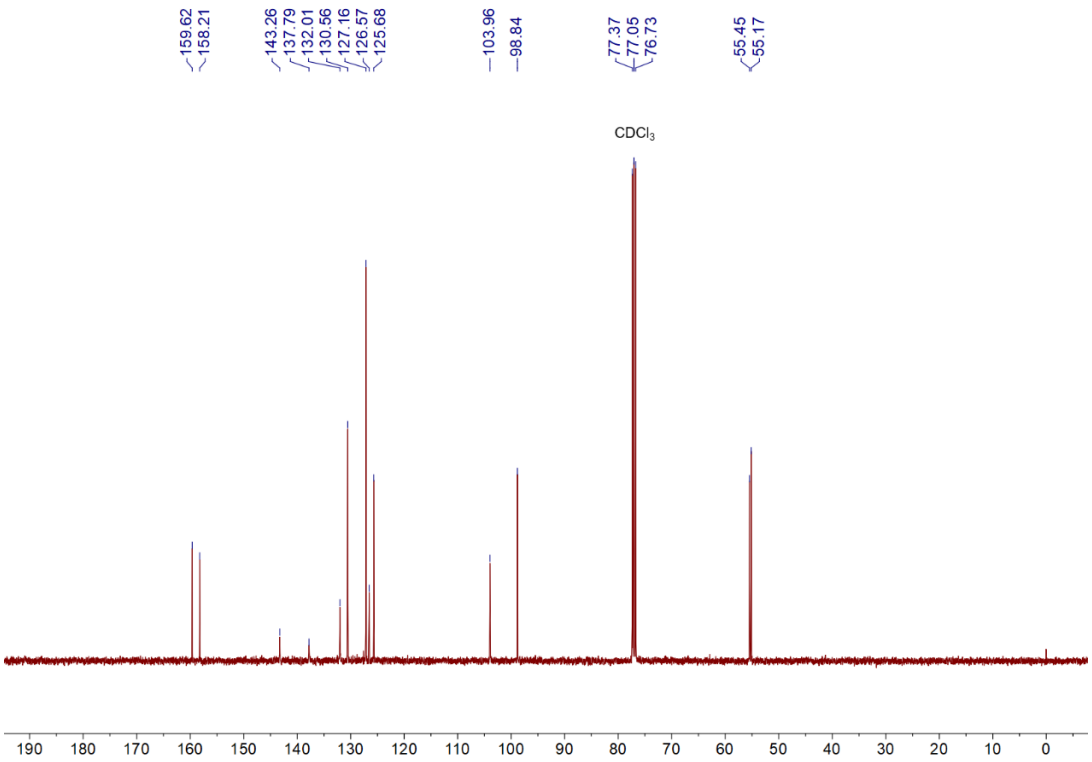

Figure S8. ^{13}C NMR spectrum (100 MHz, $CDCl_3$, room temperature) of **d**.

A was prepared according to the reported methods.[1] **a** (2.00 g, 4.42 mmol) was dissolved in 50 mL $CHCl_3$ and cooled in an ice-bath. To it, BBr_3 (4.1 mL) was added dropwise. The solution was stirred at room temperature overnight and then poured into 500 mL water. The $CHCl_3$ was removed by N_2 flow and the remaining solid was filtrated, and dried in a vacuum. **A** was obtained as a white powder (1.62 g, yield: 92.3%). Melting point: 158.2 – 160.7 °C. ^1H NMR (400 MHz, CD_3COCD_3, room temperature) of **A**: δ 7.18 – 7.02 (m, 10H), 6.64 – 6.36 (m, 6H). ^{13}C NMR (100 MHz, CD_3COCD_3, room temperature) of **A**: δ 144.66, 144.13, 143.58, 139.74, 135.94, 131.18, 130.99, 127.46, 125.99, 123.23, 123.05, 118.18, 114.41.

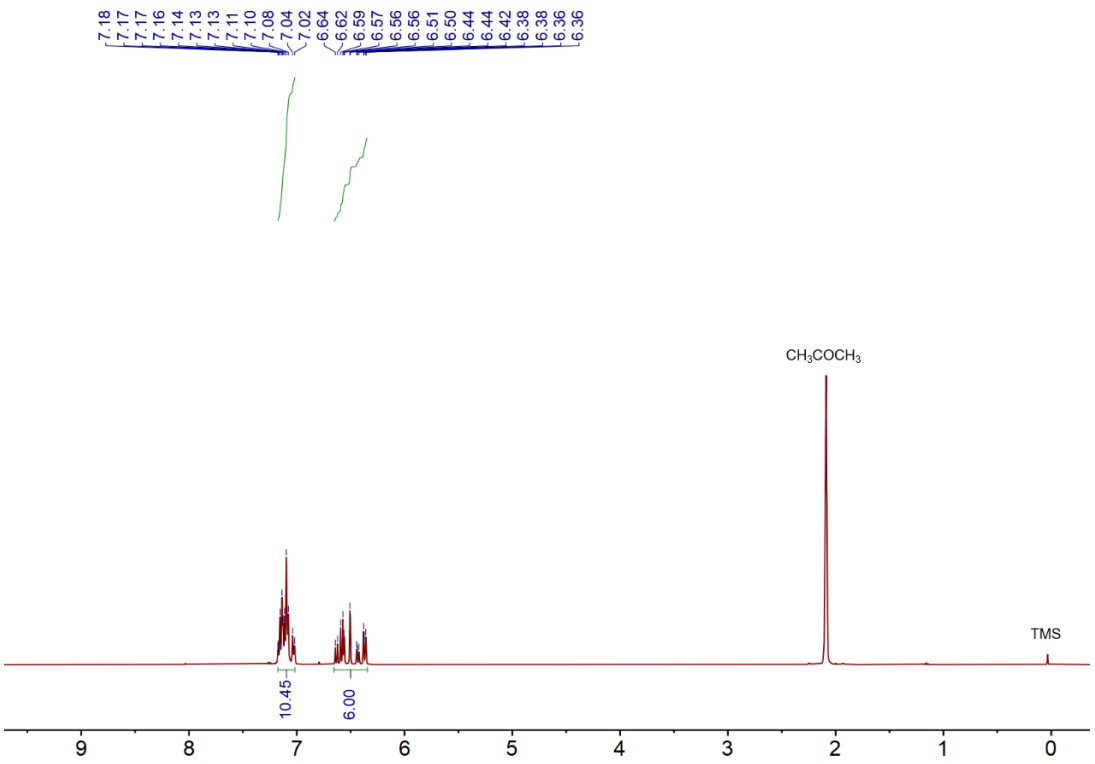

Figure S9. ^{1}H NMR spectrum (400 MHz, CD_3COCD_3, room temperature) of **A**.

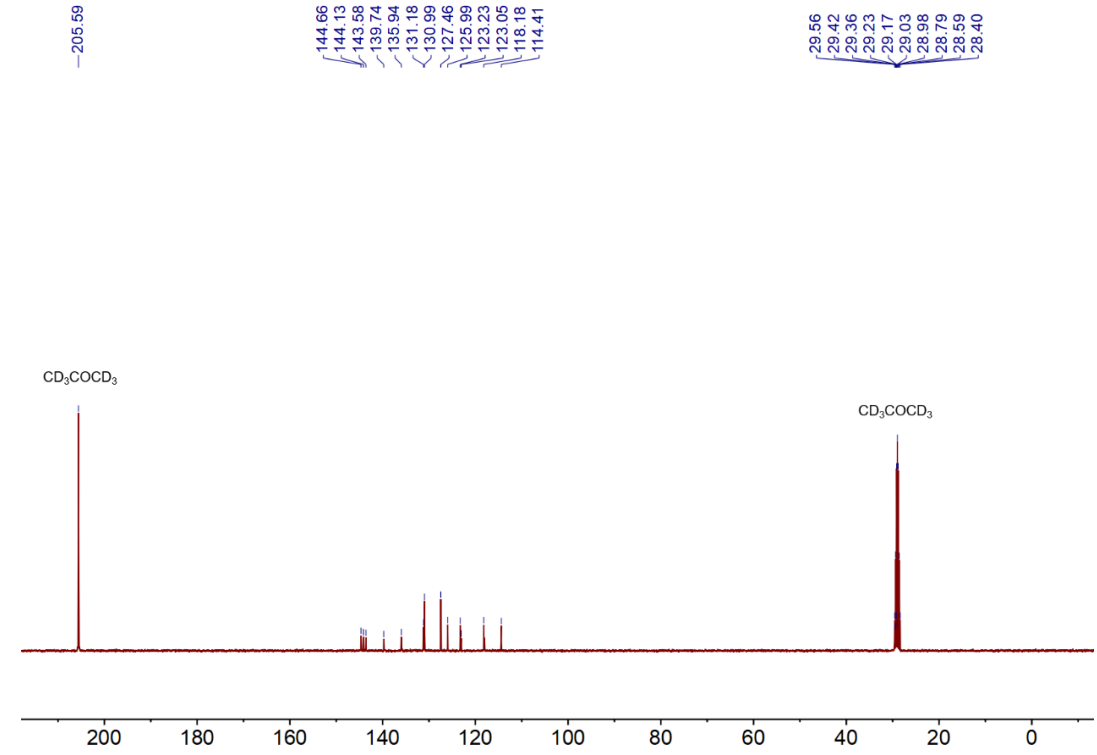

Figure S10. ^{13}C NMR spectrum (100 MHz, CD_3COCD_3, room temperature) of **A**.

B was prepared according to the reported methods.[1] **b** (2.00 g, 4.42 mmol) was dissolved in 50 mL $CHCl_3$ and cooled in an ice-bath. To it, BBr_3 (4.1 mL) was added dropwise. The solution was stirred at room temperature overnight and then poured into 500 mL water. The $CHCl_3$ was removed by N_2 flow and the remaining solid was filtrated, and dried in a vacuum. **B** was obtained as a white powder (1.57 g, yield: 90.2%). Melting point: 157.4 – 159.8 °C. ^{1}H NMR (400 MHz, CD_3COCD_3, room temperature) of

B: δ 7.12 – 6.89 (m, 10H), 6.60 – 6.32 (m, 6H). ^{13}C NMR (100 MHz, CD_3COCD_3, room temperature) of **B**: δ 144.61, 144.18, 143.75, 139.66, 136.03, 131.19, 131.00, 127.42, 125.95, 123.24, 123.06, 118.10, 114.51.

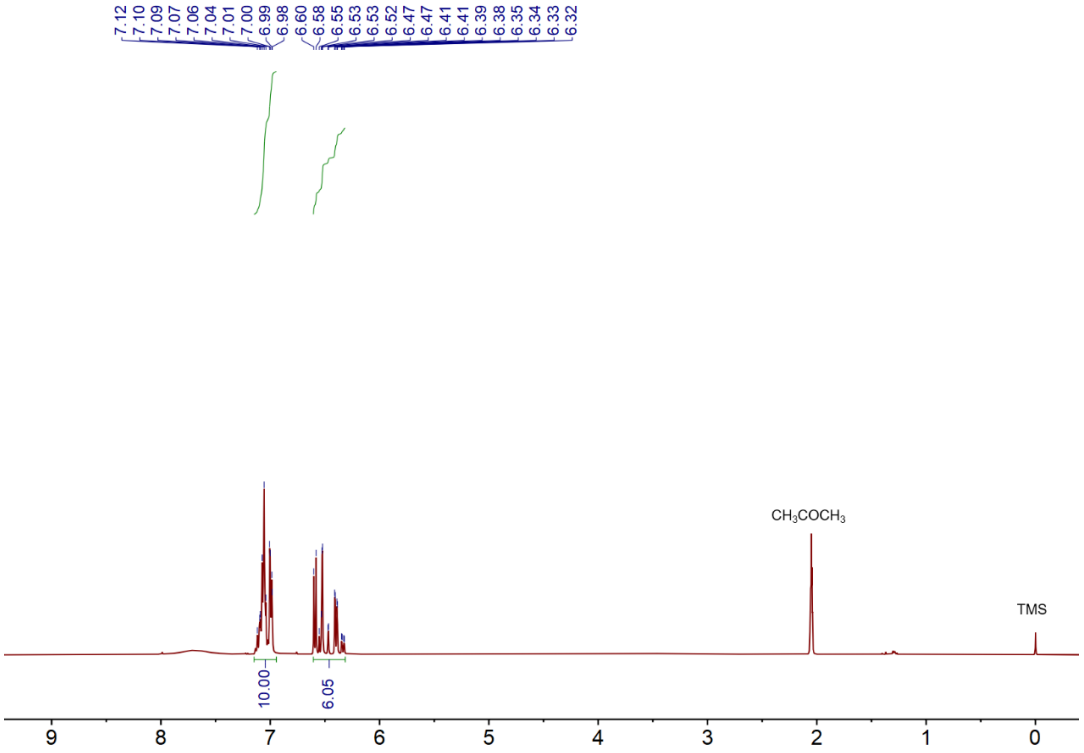

Figure S11. ^{1}H NMR spectrum (400 MHz, CD_3COCD_3, room temperature) of **B**.

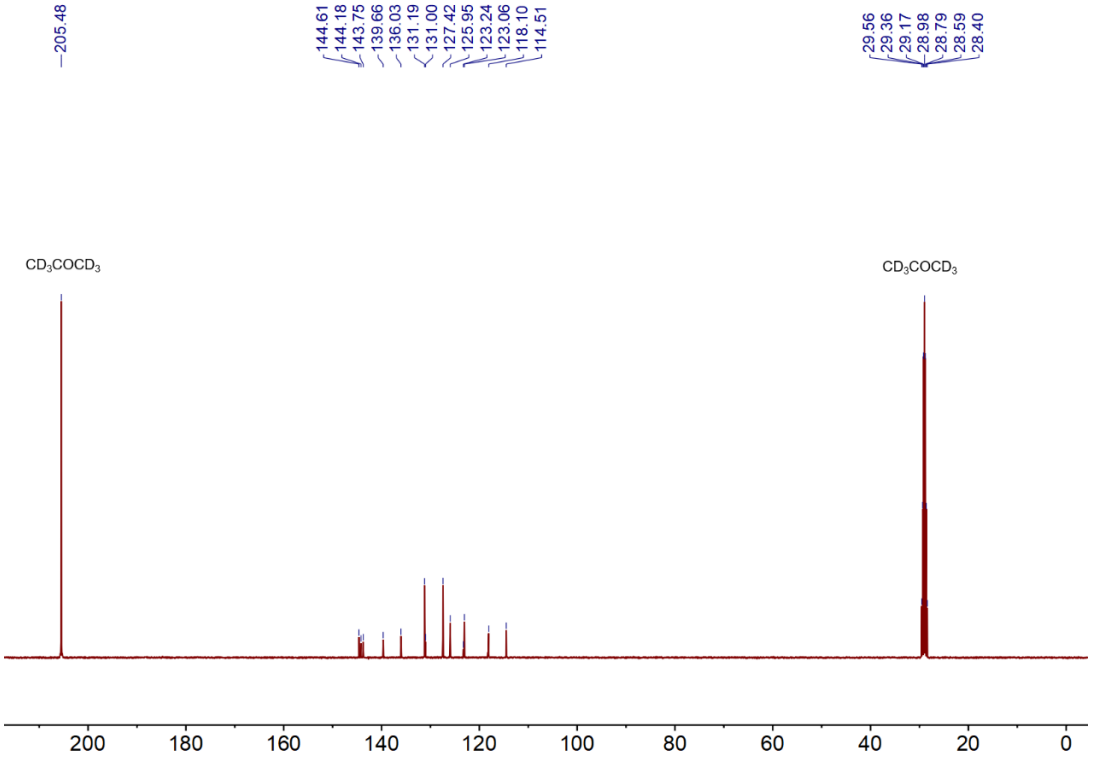

Figure S12. ^{13}C NMR spectrum (100 MHz, CD_3COCD_3, room temperature) of **B**.

C was prepared according to the reported methods.[1] **c** (2.00 g, 4.42 mmol) was dissolved in 50 mL $CHCl_3$ and cooled in an ice-bath. To it, BBr_3 (4.1 mL) was added dropwise. The solution was stirred at

room temperature overnight and then poured into 500 mL water. The $CHCl_3$ was removed by N_2 flow and the remaining solid was filtrated, and dried in a vacuum. **C** was obtained as a white powder (1.59 g, yield: 91.2%). Melting point: 347.9 – 348.7 °C. ^{1}H NMR (400 MHz, CD_3SOCD_3, room temperature) of **C**: δ 9.25 (s, 8H), 6.69 (s, 8H), 6.48 (s, 8H). ^{13}C NMR (100 MHz, CD_3COCD_3, room temperature) of **C**: δ 155.83, 138.20, 135.56, 132.43, 114.97.

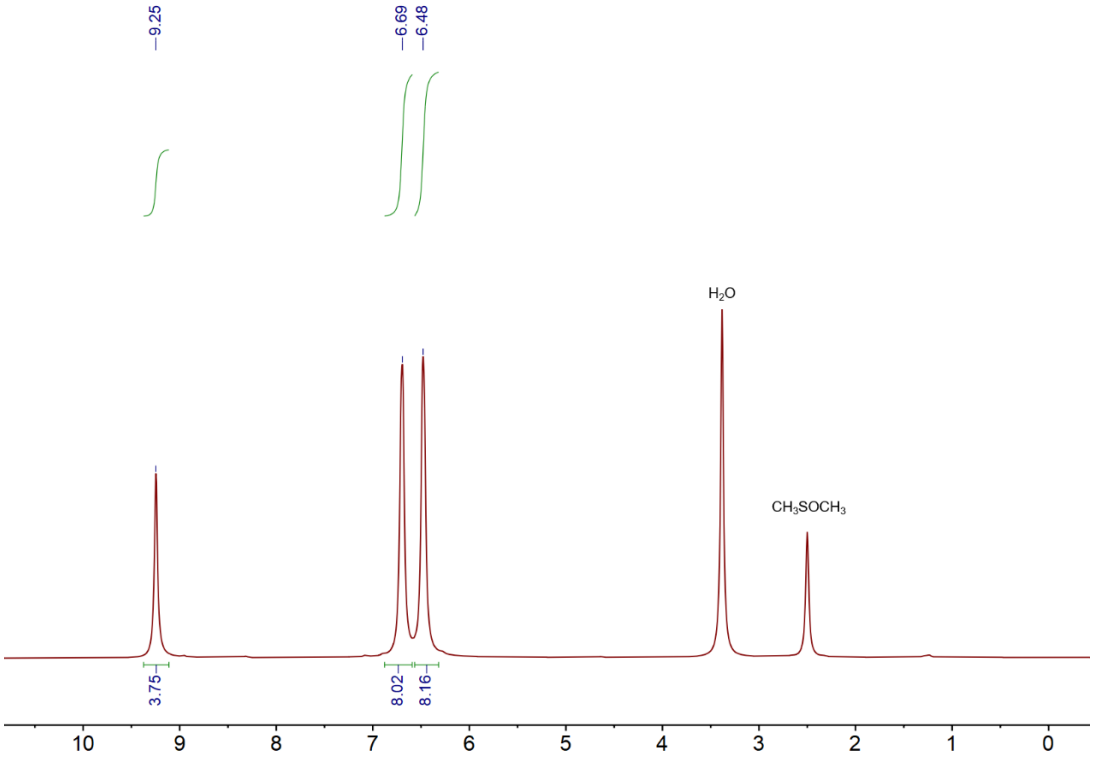

Figure S13. ^{1}H NMR spectrum (400 MHz, CD_3SOCD_3, room temperature) of **C**.

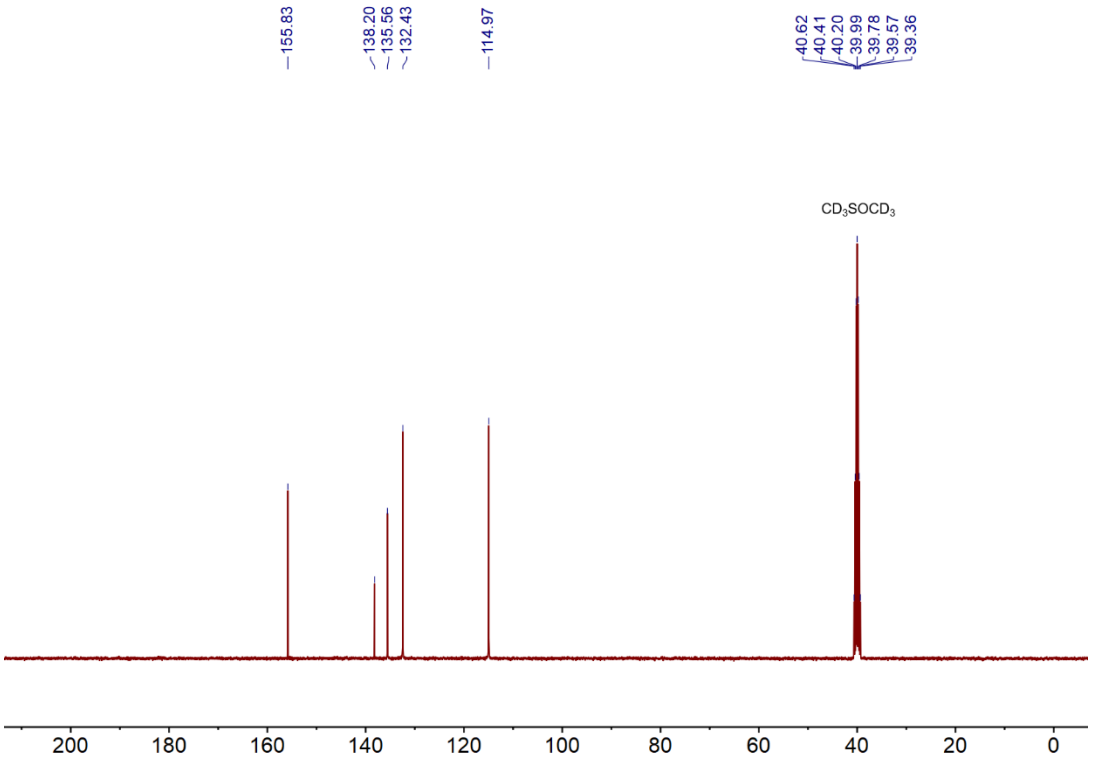

Figure S14. ^{13}C NMR spectrum (100 MHz, CD_3SOCD_3, room temperature) of **C**.

D was prepared according to the reported methods.[1] **d** (2.00 g, 4.42 mmol) was dissolved in 50 mL $CHCl_3$ and cooled in an ice-bath. To it, BBr_3 (4.1 mL) was added dropwise. The solution was stirred at room temperature overnight and then poured into 500 mL water. The $CHCl_3$ was removed by N_2 flow and the remaining solid was filtrated, and dried in a vacuum. **D** was obtained as a white powder (1.40 g, yield: 80.2%). Melting point: 204.5 – 206.2 °C. ^{1}H NMR (400 MHz, CD_3COCD_3, room temperature) of **D**: δ 7.16 – 7.02 (m, 10H), 6.91 – 6.88 (m, 2H), 6.32 – 6.21 (m, 4H). ^{13}C NMR (100 MHz, CD_3COCD_3, room temperature) of **D**: δ 157.42, 154.97, 142.91, 138.65, 132.02, 130.46, 129.72, 127.28, 127.12, 126.19, 126.00, 102.42, 102.06.

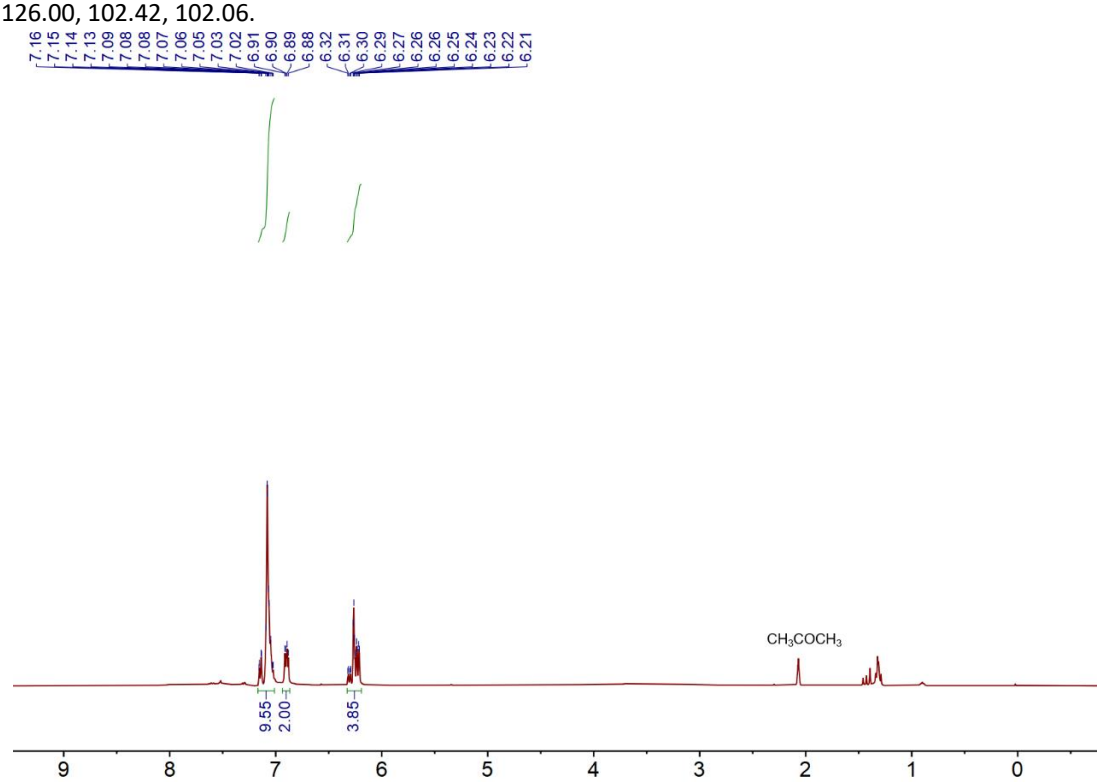

Figure S15. ^{1}H NMR spectrum (400 MHz, CD_3COCD_3, room temperature) of **D**.

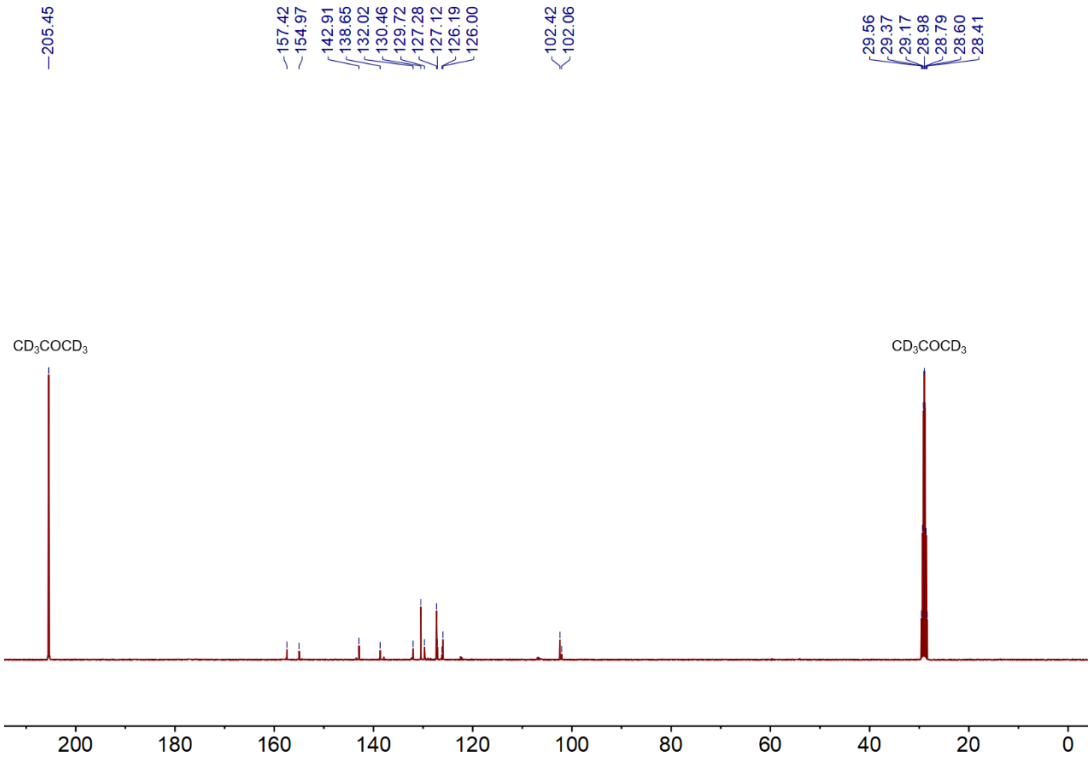

Figure S16. ^{13}C NMR spectrum (100 MHz, CD_3COCD_3, room temperature) of **D**.

3. NOESY spectra of monomers a and b

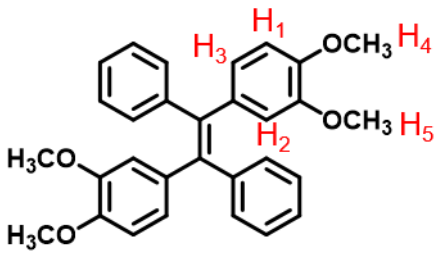

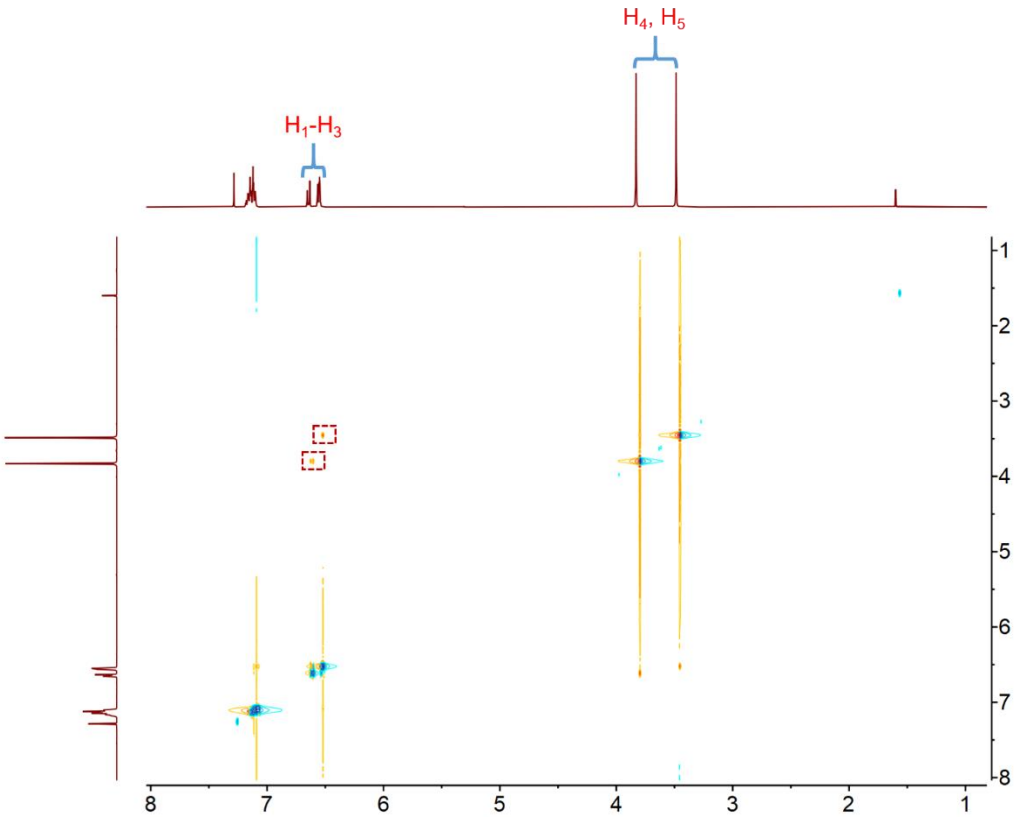

Figure S17. NOESY spectra (100 MHz, $CDCl_3$, room temperature) of **a**.

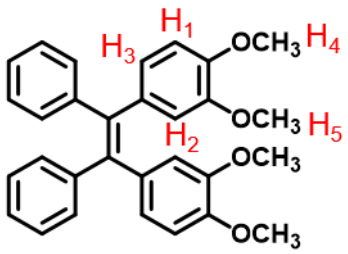

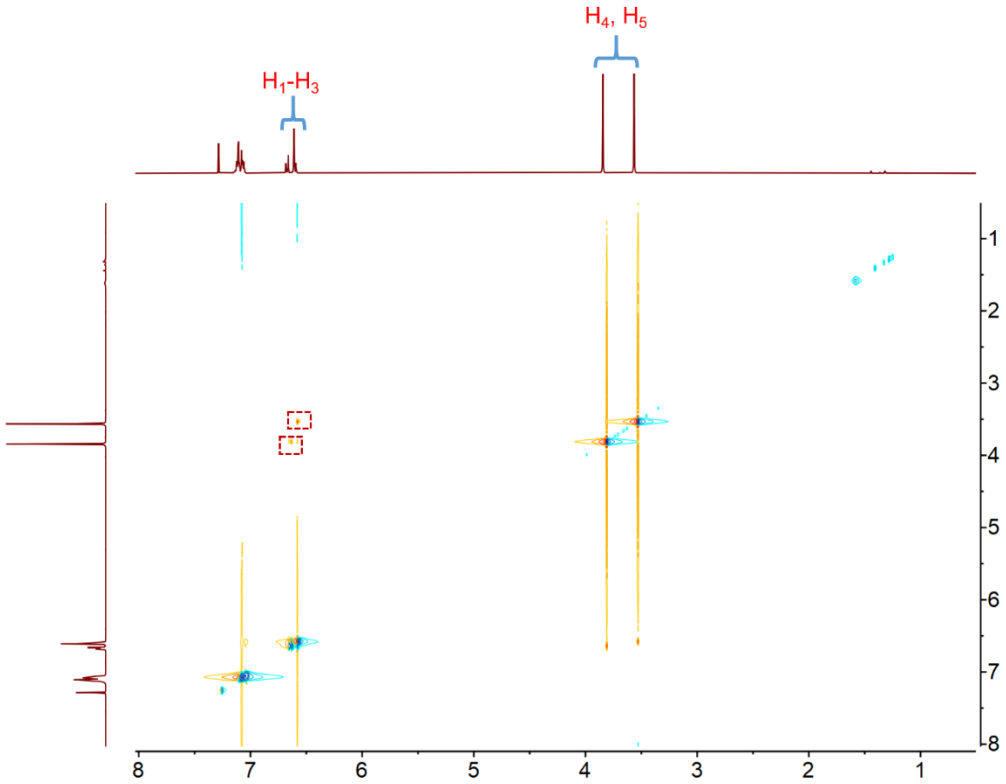

Figure S18. NOESY spectra (100 MHz, $CDCl_3$, room temperature) of **b**.

4. Single crystal of monomers b and d

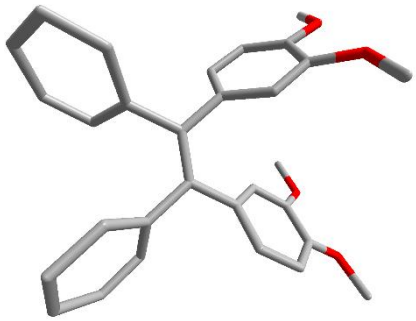

Figure S19. Single crystal structure of **b** (red: **O**, glay: **C**).

Single crystal of monomer **b** was shown in **Figure S9**, demonstrating that the configuration of **b** is a *cis*-isomer.

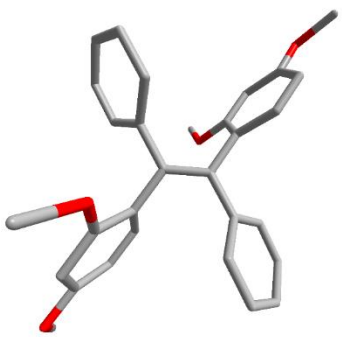

Figure S20. Single crystal structure of **d** (red: **O**, glay: **C**).

Single crystal of monomer **d** was shown in **Figure S9**, demonstrating that the configuration of **d** is a *trans*-isomer.

5. Preparation and characterization of poly(TA-TPE)s

Table S1. Poly(**TA-TPE**)s prepared from synthesized monomer and **TA**.

Number	Acids	Ratio	**TPE**s	Abbreviation	Formation of poly(**TA-TPE**)s
1	**TA**	1:1	**A**	Poly(**TA-A**)$_{1/1}$	No
2	**TA**	8:1	**A**	Poly(**TA-A**)$_{8/1}$	Yes
3	**TA**	16:1	**A**	Poly(**TA-A**)$_{16/1}$	Yes
4	**TA**	24:1	**A**	Poly(**TA-A**)$_{24/1}$	Yes
5	**TA**	32:1	**A**	Poly(**TA-A**)$_{32/1}$	Yes
6	**TA**	1:1	**B**	Poly(**TA-B**)$_{1/1}$	No
7	**TA**	8:1	**B**	Poly(**TA-B**)$_{8/1}$	Yes
8	**TA**	16:1	**B**	Poly(**TA-B**)$_{16/1}$	Yes
9	**TA**	24:1	**B**	Poly(**TA-B**)$_{24/1}$	Yes
10	**TA**	32:1	**B**	Poly(**TA-B**)$_{32/1}$	Yes
11	**TA**	1:1	**C**	Poly(**TA-C**)$_{1/1}$	No
12	**TA**	8:1	**C**	Poly(**TA-C**)$_{8/1}$	No
13	**TA**	16:1	**C**	Poly(**TA-C**)$_{16/1}$	No
14	**TA**	24:1	**C**	Poly(**TA-C**)$_{24/1}$	No
15	**TA**	32:1	**C**	Poly(**TA-C**)$_{32/1}$	No
16	**TA**	1:1	**D**	Poly(**TA-D**)$_{1/1}$	No
17	**TA**	8:1	**D**	Poly(**TA-D**)$_{8/1}$	Yes
18	**TA**	16:1	**D**	Poly(**TA-D**)$_{16/1}$	Yes
19	**TA**	24:1	**D**	Poly(**TA-D**)$_{24/1}$	Yes
20	**TA**	32:1	**D**	Poly(**TA-D**)$_{32/1}$	Yes
21	**TA**	1:1	**E**	Poly(**TA-E**)$_{1/1}$	No
22	**TA**	8:1	**E**	Poly(**TA-E**)$_{8/1}$	Yes
23	**TA**	16:1	**E**	Poly(**TA-E**)$_{16/1}$	Yes
24	**TA**	24:1	**E**	Poly(**TA-E**)$_{24/1}$	Yes
25	**TA**	32:1	**E**	Poly(**TA-E**)$_{32/1}$	Yes

The mixture of **TPE**s (**A**-**E**) and thioctic acid (**TA**) was heated at 120 °C for 20-30 minutes, and then cooled to room temperature to obtain bulk poly(**TA-TPE**)s (**Figure S21**). All poly(**TA-TPE**)s were listed in **Table S1** and **Figure S22**.

Figure S21. Preparation process of poly(**TA-A**)$_{8/1}$.

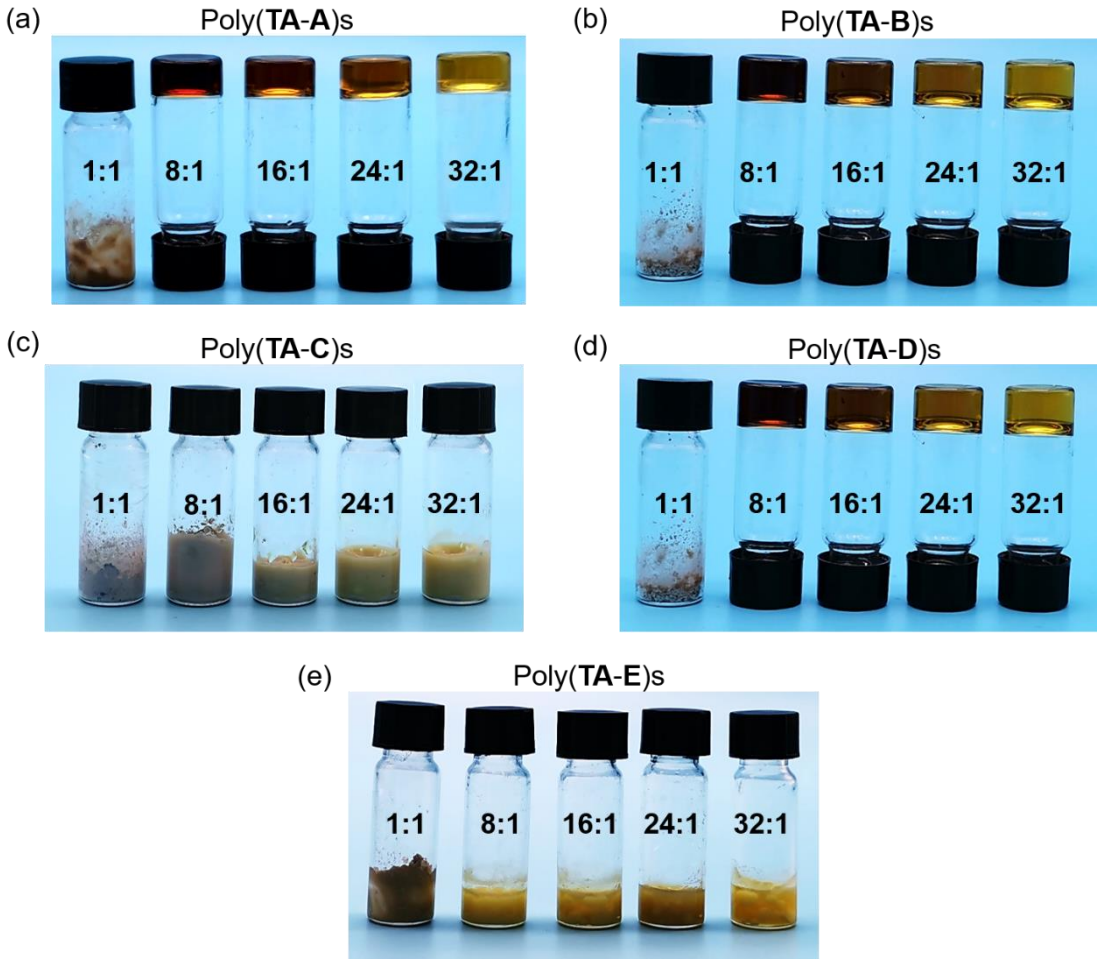

Figure S22. Macroscopic views of poly(**TA-TPE**)s: (a) poly(**TA-A**)s; (b) poly(**TA-B**)s; (c) poly(**TA-C**)s; (d) poly(**TA-D**)s; (e) poly(**TA-E**)s.

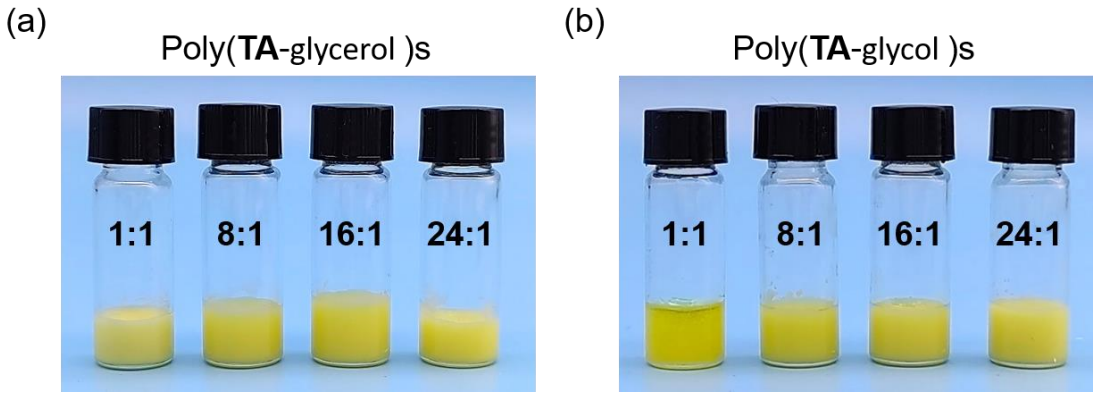

Figure S23. The polymerization behavior of (a) poly(**TA**-glycerol)s and (b) poly(**TA**-glycol)s.

6. ^{1}H NMR spectra of poly(TA-TPE)s

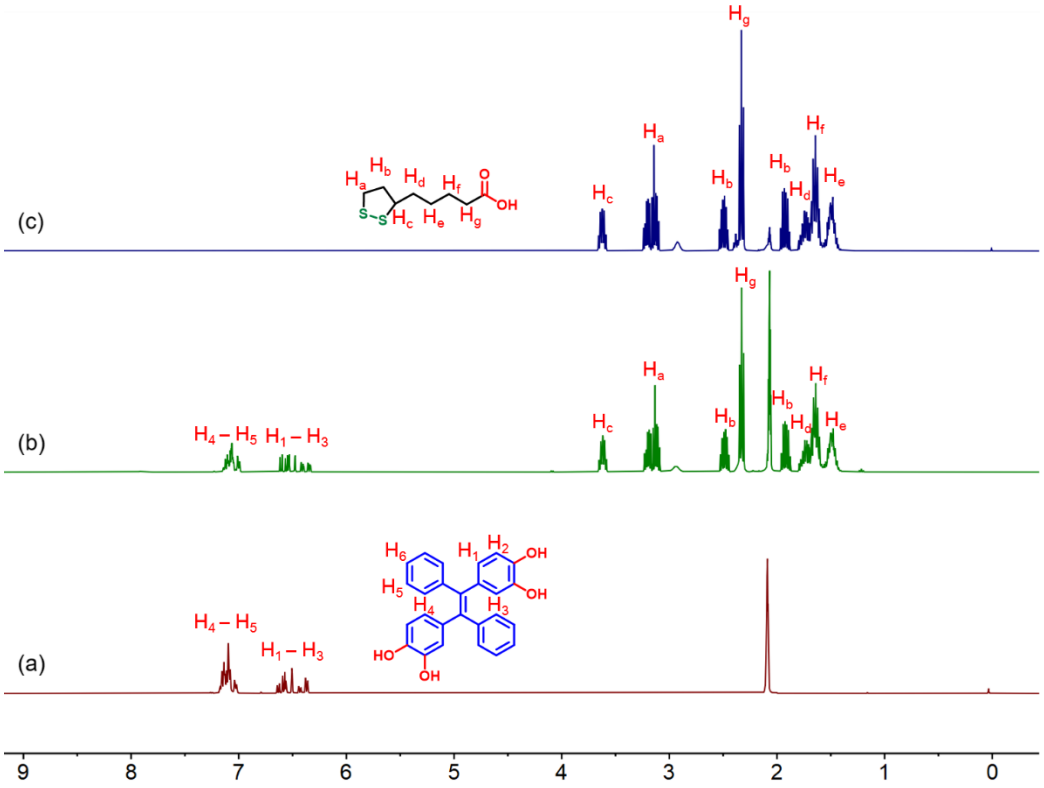

Figure S24. ^{1}H NMR spectra (400 MHz, CD_3COCD_3, room temperature): (a) **A** (30 mg/mL); (b) poly(**TA**-**A**)$_{8/1}$ (155 mg/mL); (c) **TA** (125 mg/mL).

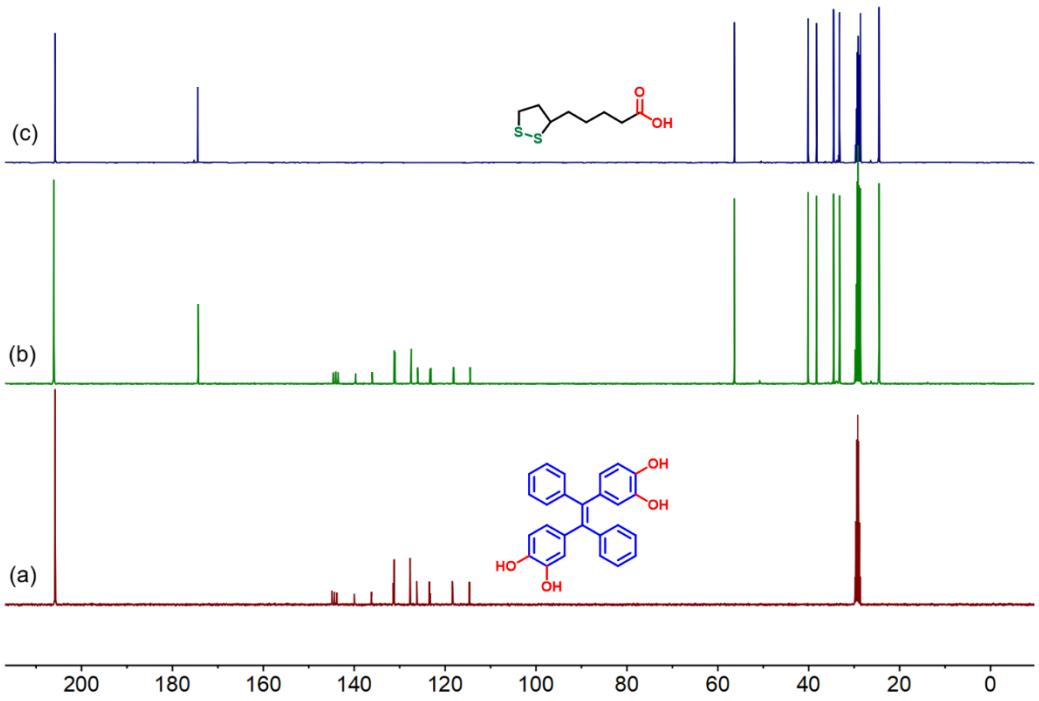

Figure S25. ^{13}C NMR spectra (400 MHz, CD_3COCD_3, room temperature): (a) **A** (30 mg/mL); (b) poly(**TA**-**A**)$_{8/1}$ (155 mg/mL); (c) **TA** (125 mg/mL).

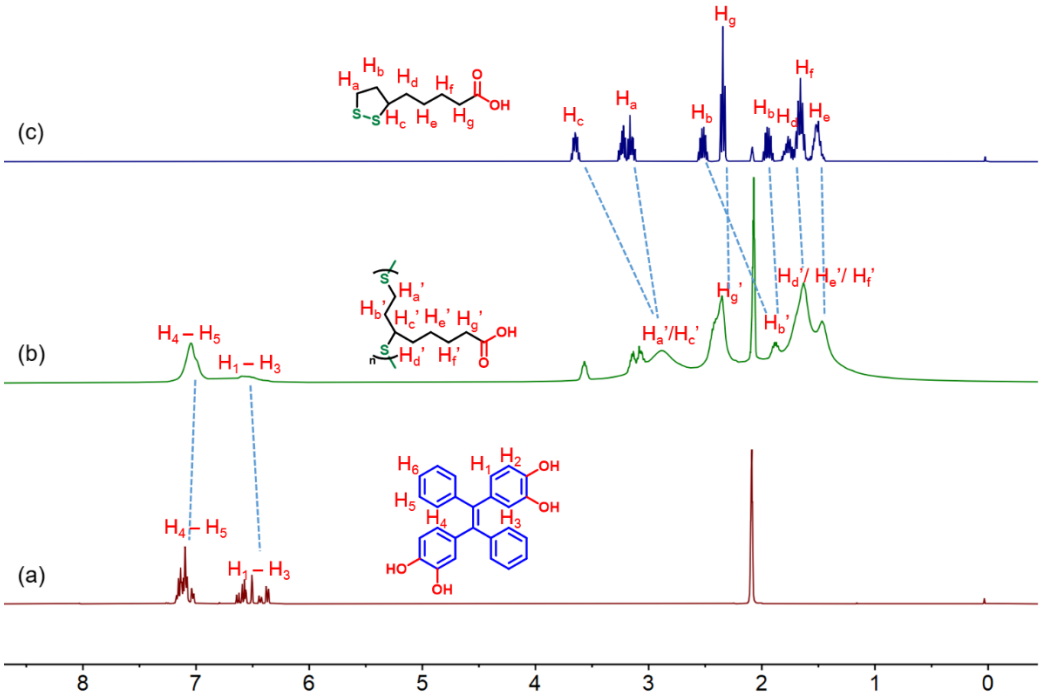

Figure S26. ^{1}H NMR spectra (400 MHz, CD_3COCD_3, room temperature): (a) **A** (30 mg/mL); (b) poly(**TA**-**A**)$_{8/1}$ (800 mg/mL); (c) **TA** (200 mg/mL).

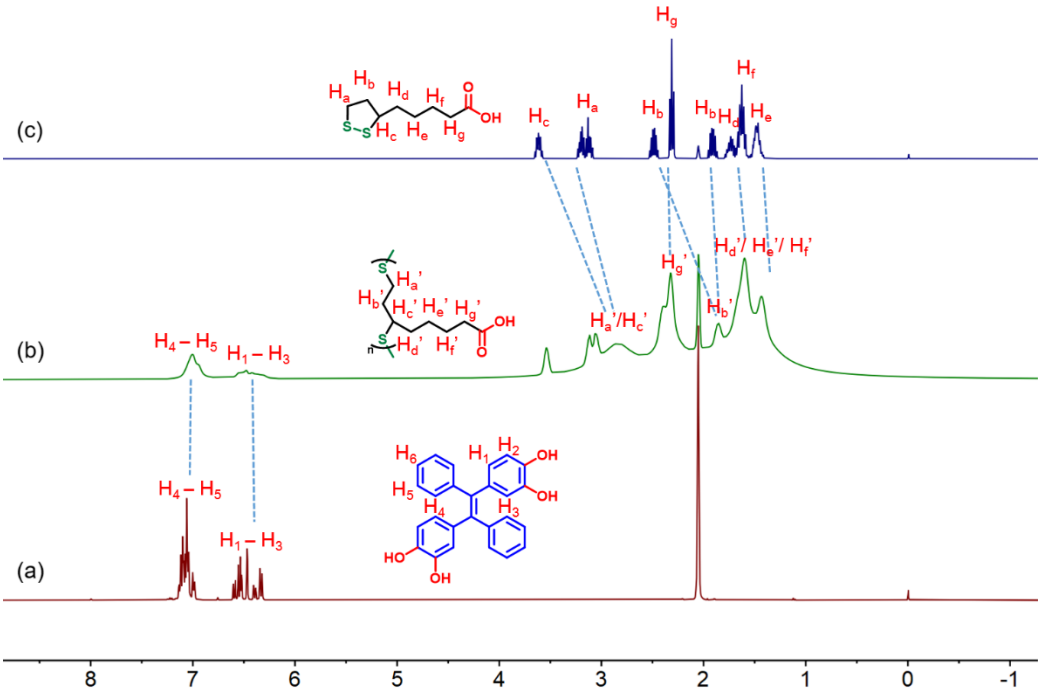

Figure S27. ^{1}H NMR spectra (400 MHz, CD_3COCD_3, room temperature): (a) **A** (30 mg/mL); (b) poly(**TA**-**A**)$_{16/1}$ (800 mg/mL); (c) **TA** (200 mg/mL).

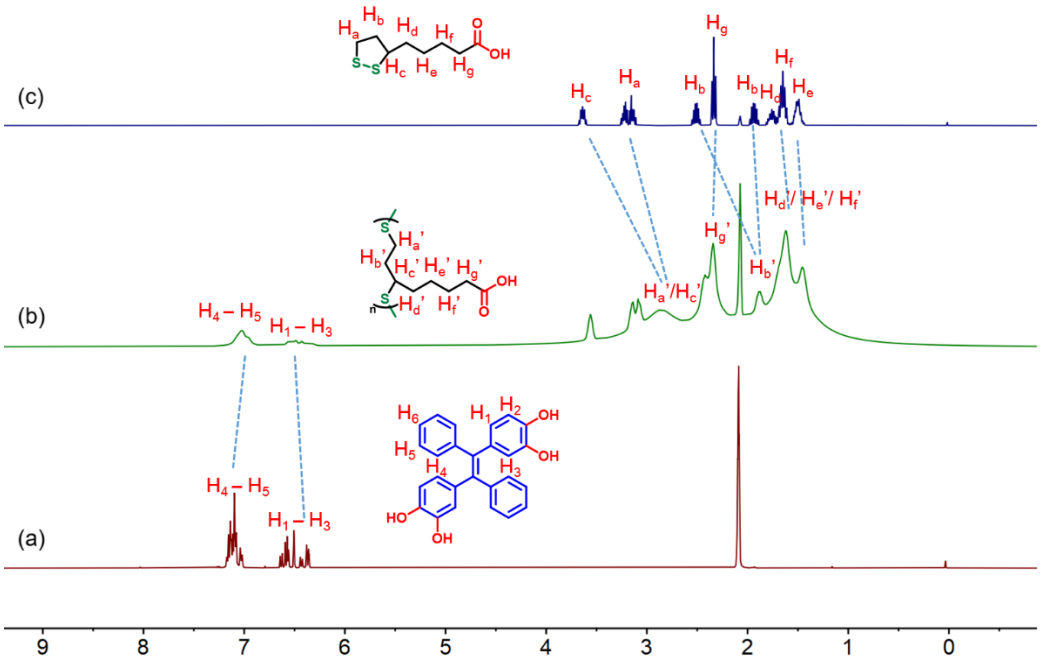

Figure S28. ^{1}H NMR spectra (400 MHz, CD_3COCD_3, room temperature): (a) **A** (30 mg/mL); (b) poly(**TA**-**A**)$_{24/1}$ (800 mg/mL); (c) **TA** (200 mg/mL).

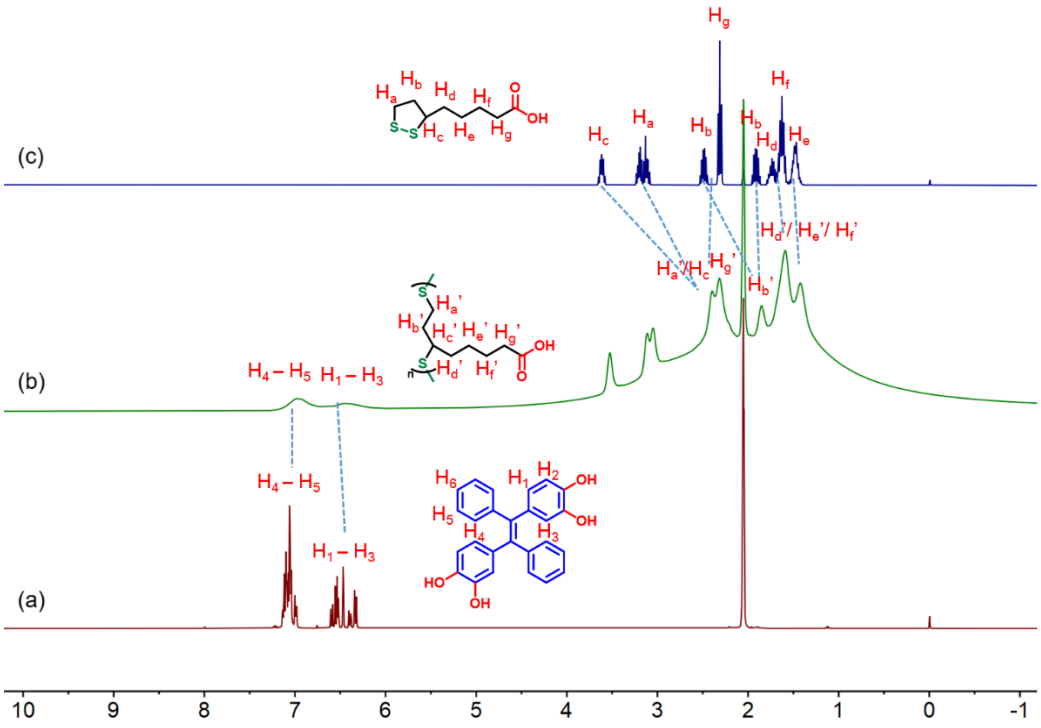

Figure S29. ^{1}H NMR spectra (400 MHz, CD_3COCD_3, room temperature): (a) **A** (30 mg/mL); (b) poly(**TA**-**A**)$_{32/1}$ (800 mg/mL); (c) **TA** (200 mg/mL).

7. High-resolution mass spectrometry (HRMS) of poly(TA-A)$_{8/1}$

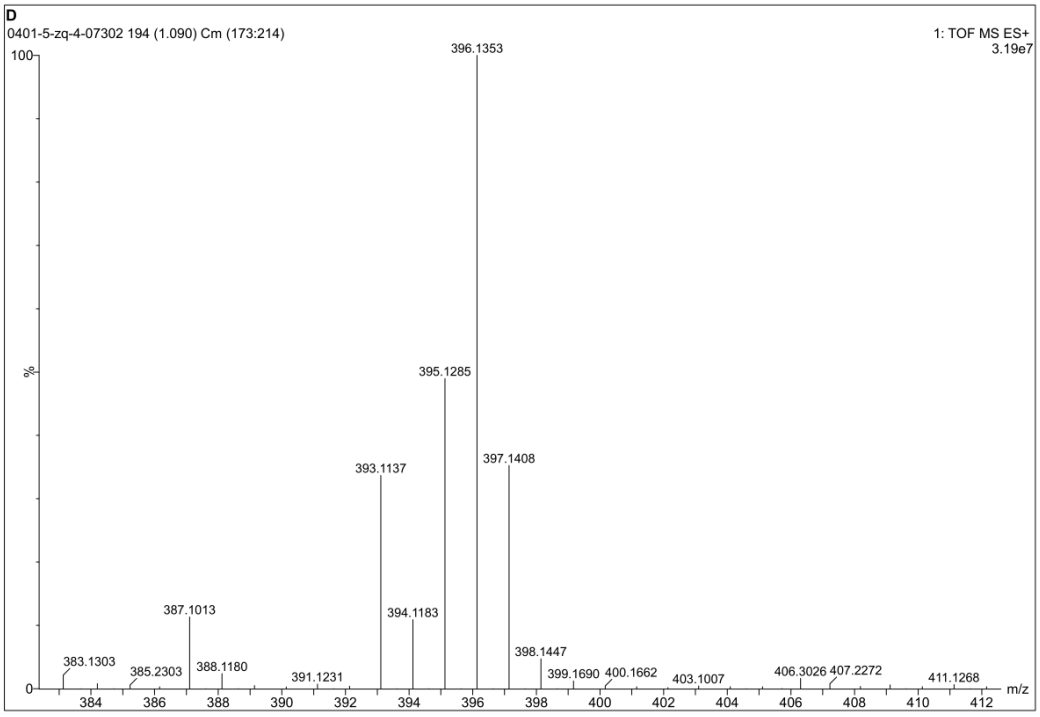

Figure S30. High-resolution mass spectrometry of poly(**TA**-**A**)$_{8/1}$.

As shown in **Figure S30**, the peak of **A** (HRESIMS: m/s calcd for [**A**]$^+$ $C_{26}H_{20}O_4$, 396.1362; found 396.1353, error 2.3 ppm) can also be observed in the high-resolution mass spectrometry of poly(**TA**-**A**)$_{8/1}$.

8. Concentration dependent ^{1}H NMR spectra of poly(TA-TPE)s

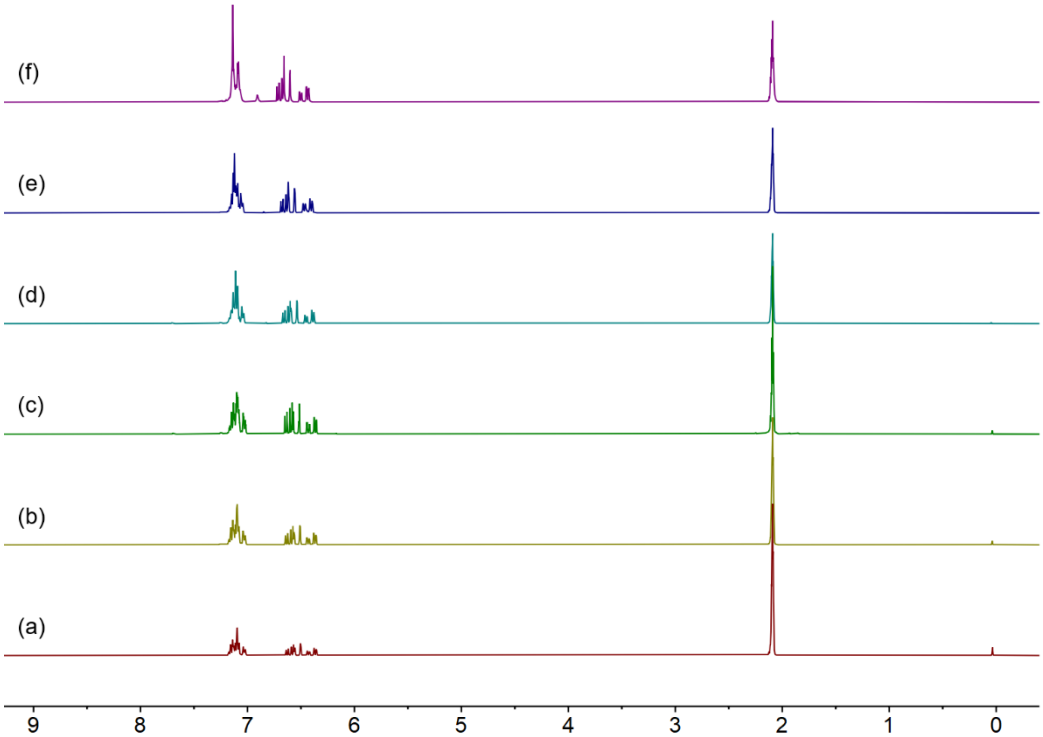

Figure S31. Concentration dependent ^{1}H NMR spectra (400 MHz, CD_3COCD_3, room temperature) of **A**: (a) 5 mg/mL; (b) 50

mg/mL; (c) 100 mg/mL; (d) 200 mg/mL; (e) 300 mg/mL; (f) 500 mg/mL.

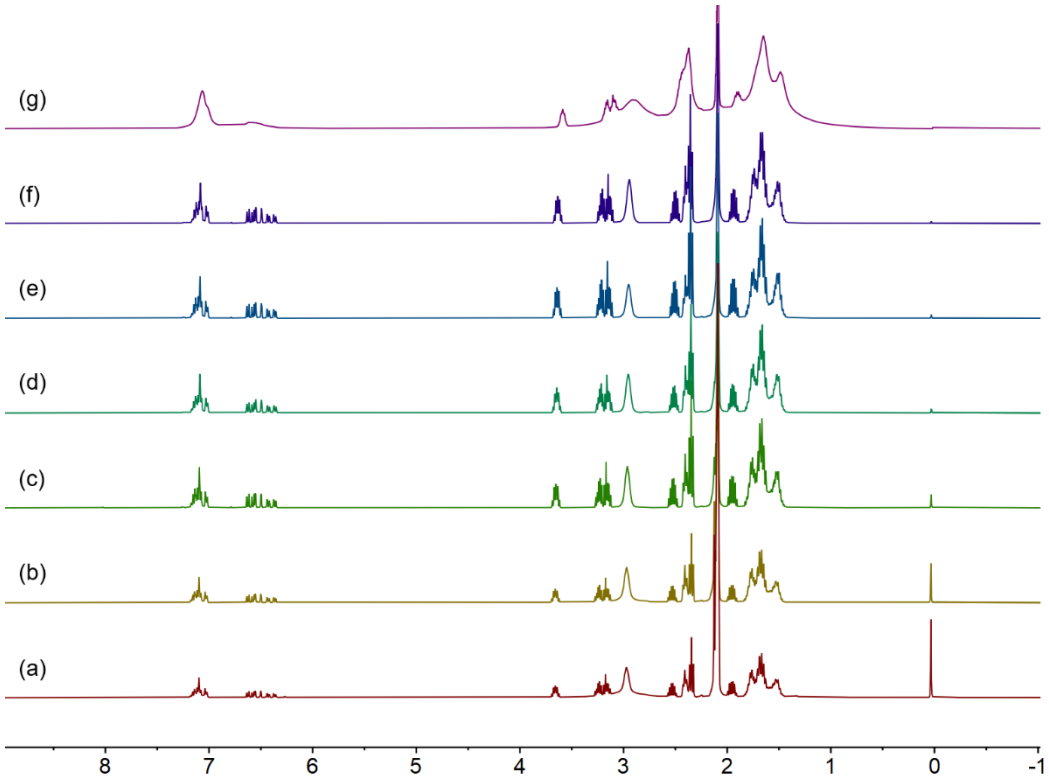

Figure S32. Concentration dependent ^{1}H NMR spectra (400 MHz, CD_3COCD_3, room temperature) of poly(**TA-A**)$_{8/1}$: (a) 5 mg/mL; (b) 50 mg/mL; (c) 100 mg/mL; (d) 200 mg/mL; (e) 300 mg/mL; (f) 500 mg/ mL; (g) 800 mg/mL.

9. COSY and NOESY spectra of poly(TA-TPE)$_S$

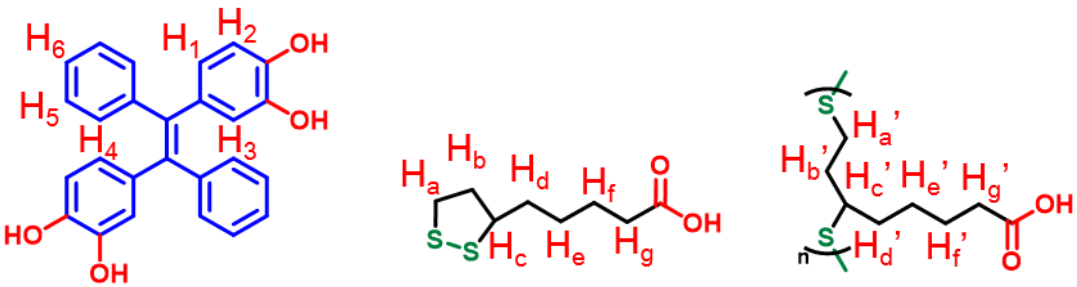

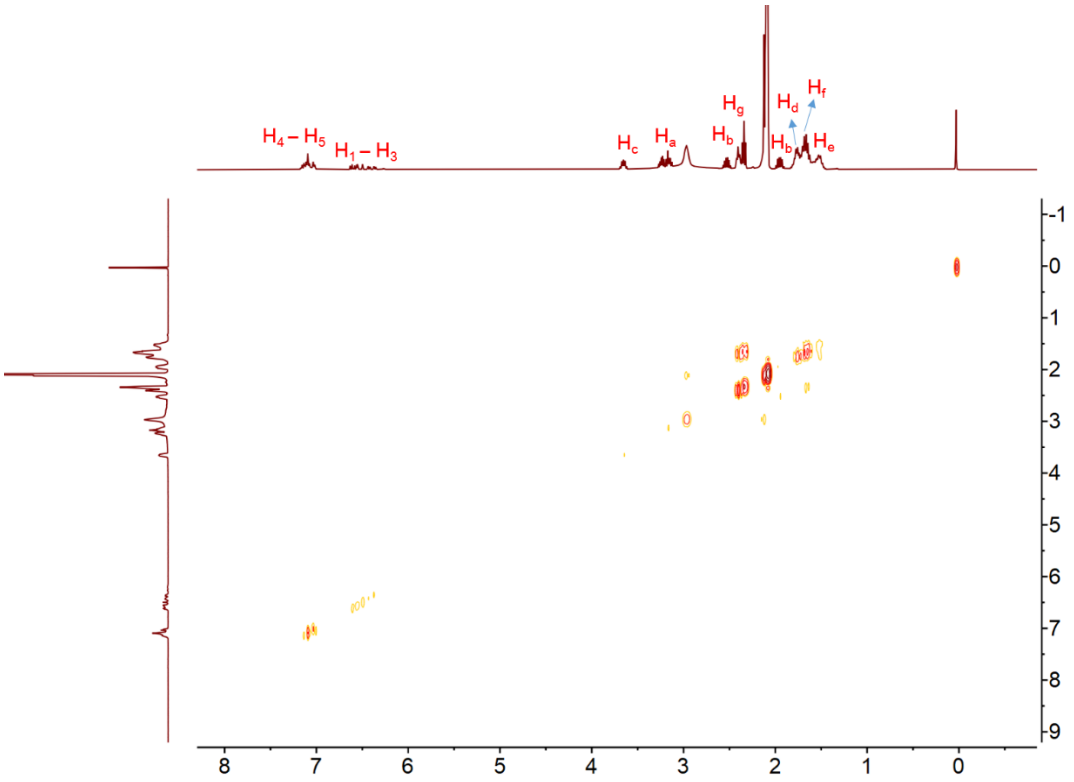

Figure S33. ^{1}H-^{1}H COSY spectra (400 MHz, CD_3COCD_3, room temperature) of poly(**TA**-**A**)$_{8/1}$ (5 mg/mL).

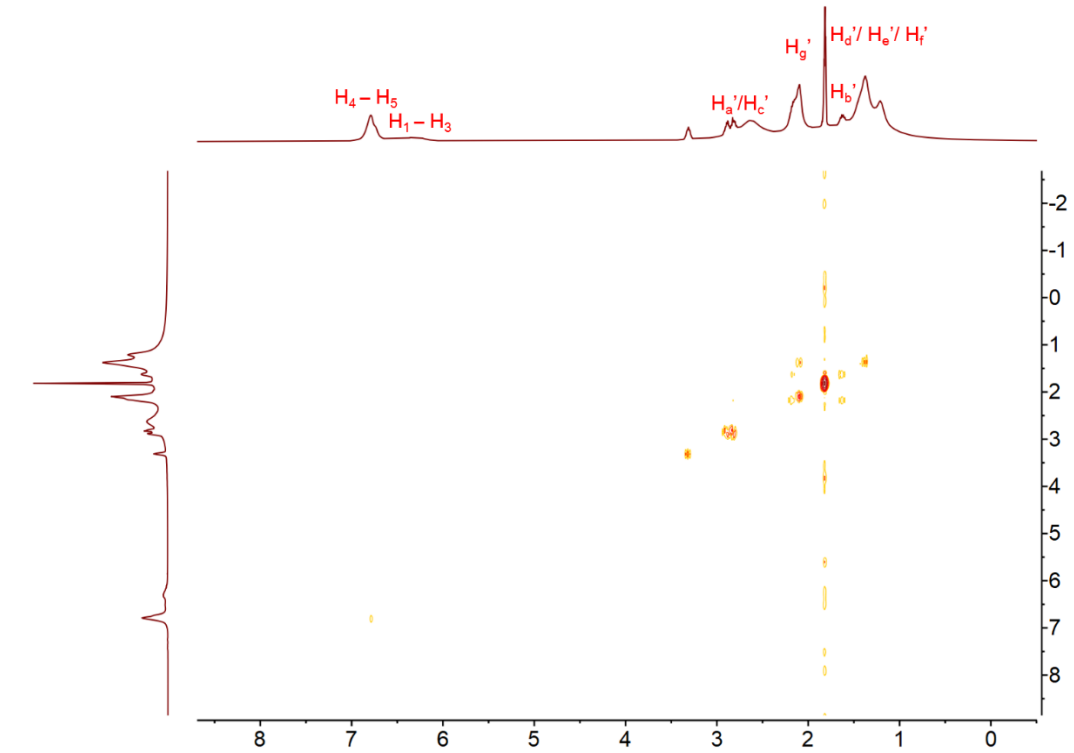

Figure S34. ^{1}H-^{1}H COSY spectra (400 MHz, CD_3COCD_3, room temperature) of poly(**TA**-**A**)$_{8/1}$ (800 mg/mL).

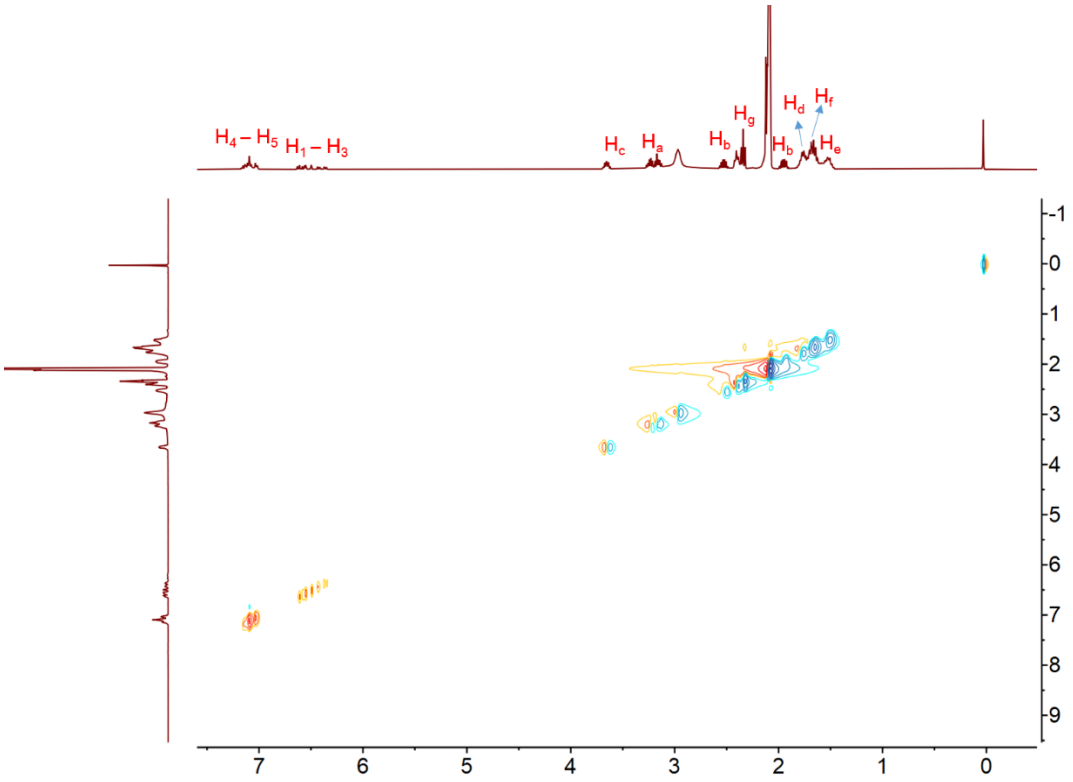

Figure S35. ^{1}H-^{1}H NOESY spectra (400 MHz, CD_3COCD_3, room temperature) of poly(**TA**-**A**)$_{8/1}$ (5 mg/mL).

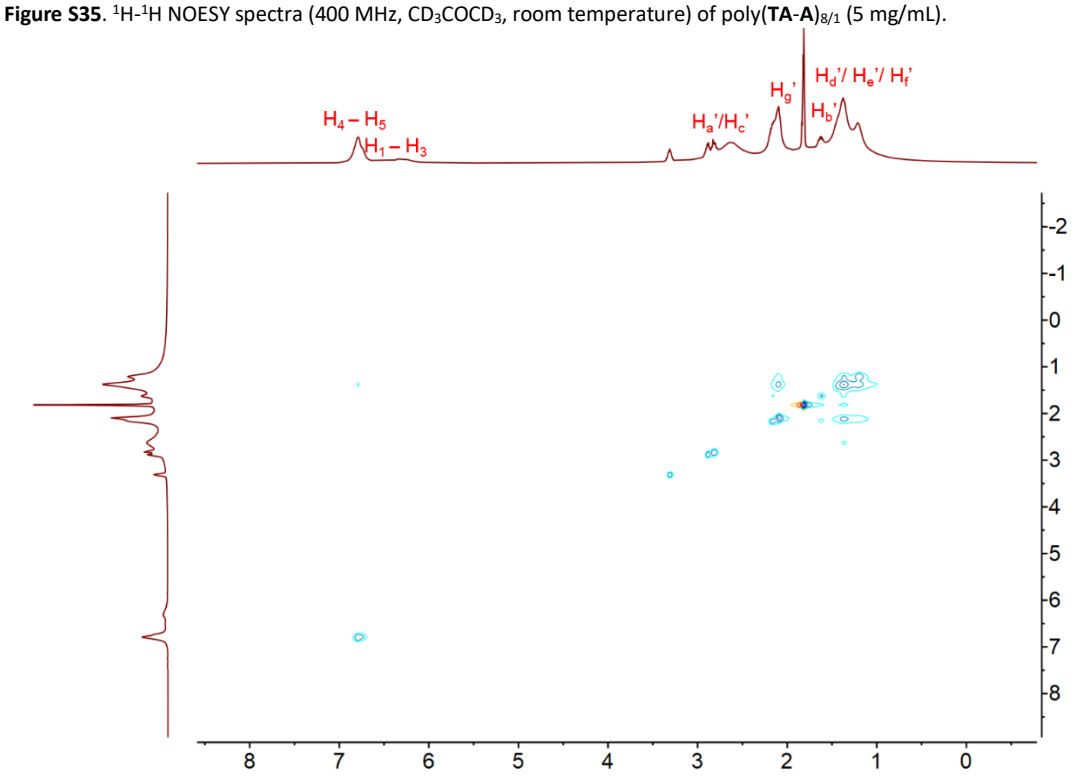

Figure S36. ^{1}H-^{1}H NOESY spectra (400 MHz, CD_3COCD_3, room temperature) of poly(**TA**-**A**)$_{8/1}$ (800 mg/mL).

10. ^{1}H NMR spectra of poly(TA-TPE)s in D_2O

After soaking poly(**TA**-**A**)$_{8/1}$ in D_2O for 24 hours, the upper clarifier was taken for ^{1}H NMR experiments. No proton peak was observed in the ^{1}H NMR spectrum, indicating that poly(**TA**-**A**)$_{8/1}$ has good water resistance.

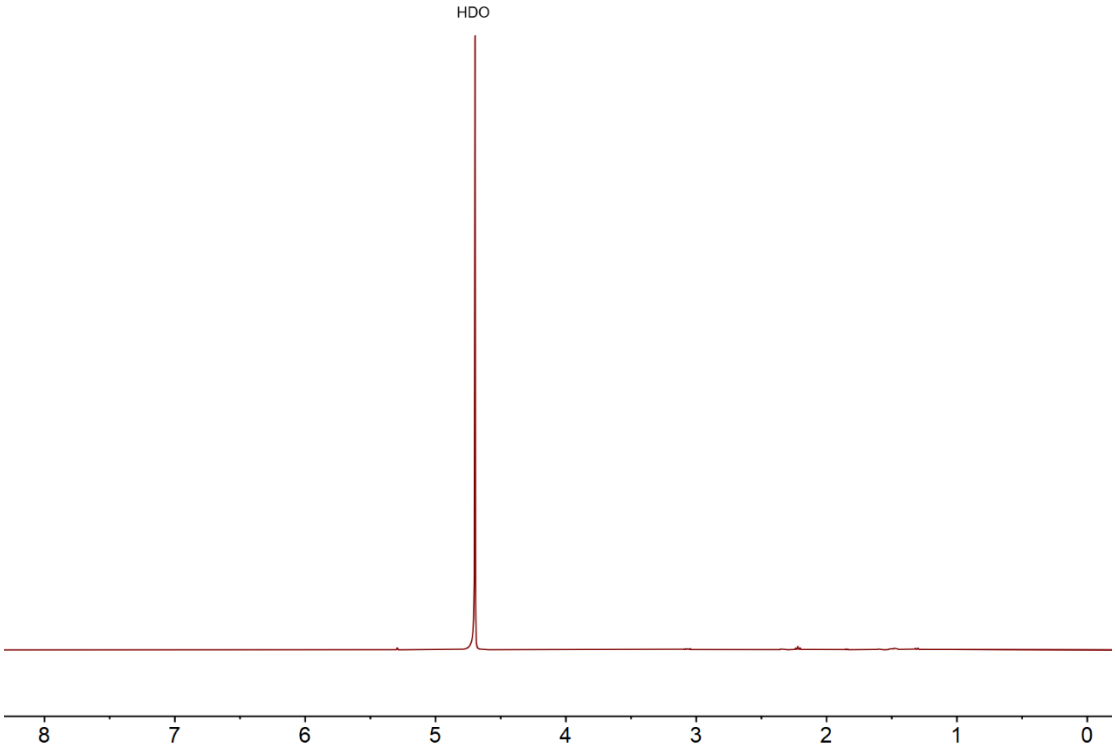

Figure S37. ^{1}H NMR spectrum of **TA** immersed in D_2O for 24h.

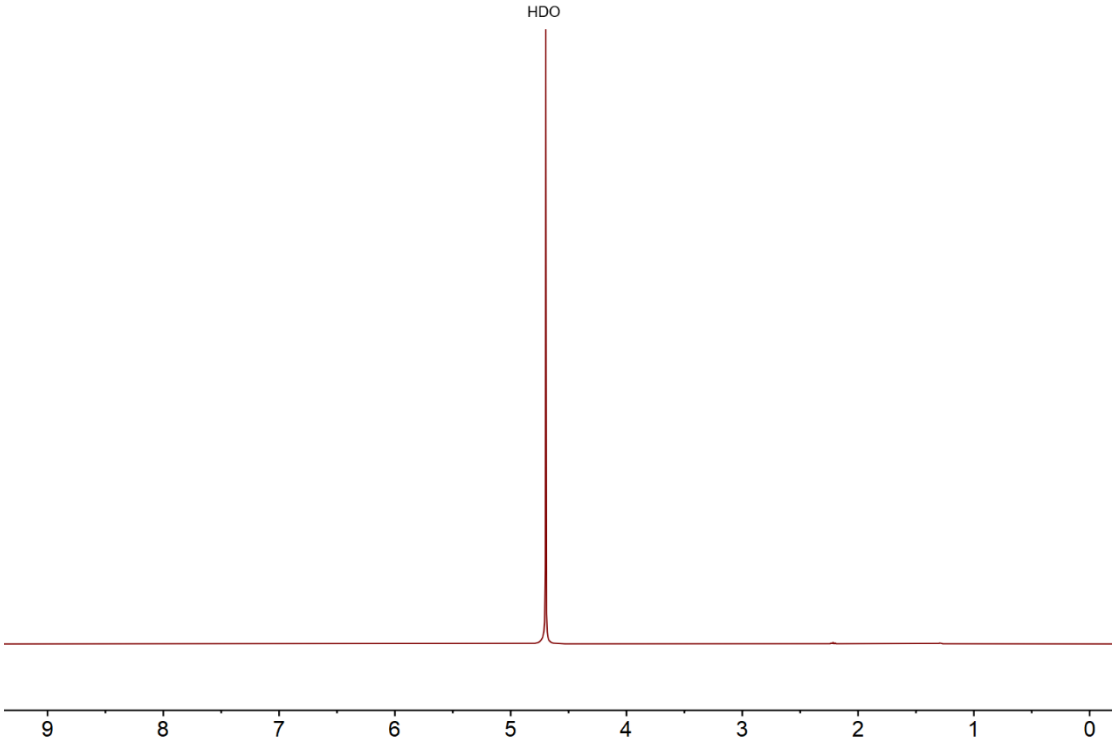

Figure S38. ^{1}H NMR spectrum of poly(**TA)** immersed in D_2O for 24h.

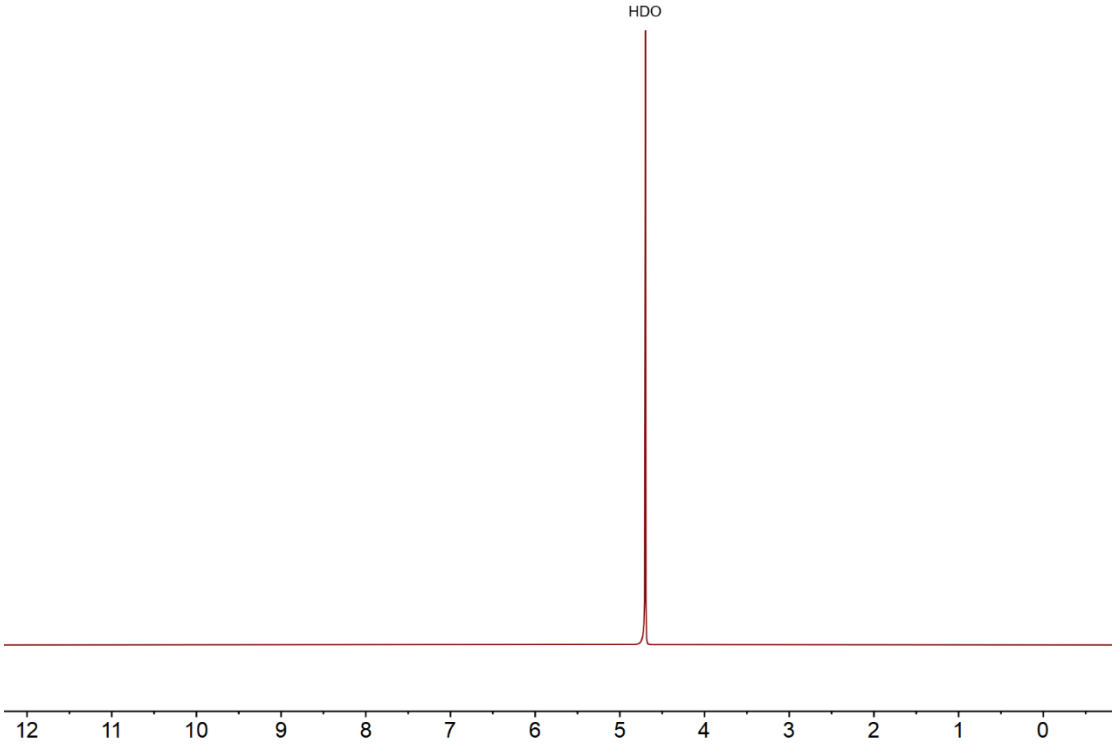

Figure S39. ^{1}H NMR spectrum of **A** immersed in D_2O for 24h.

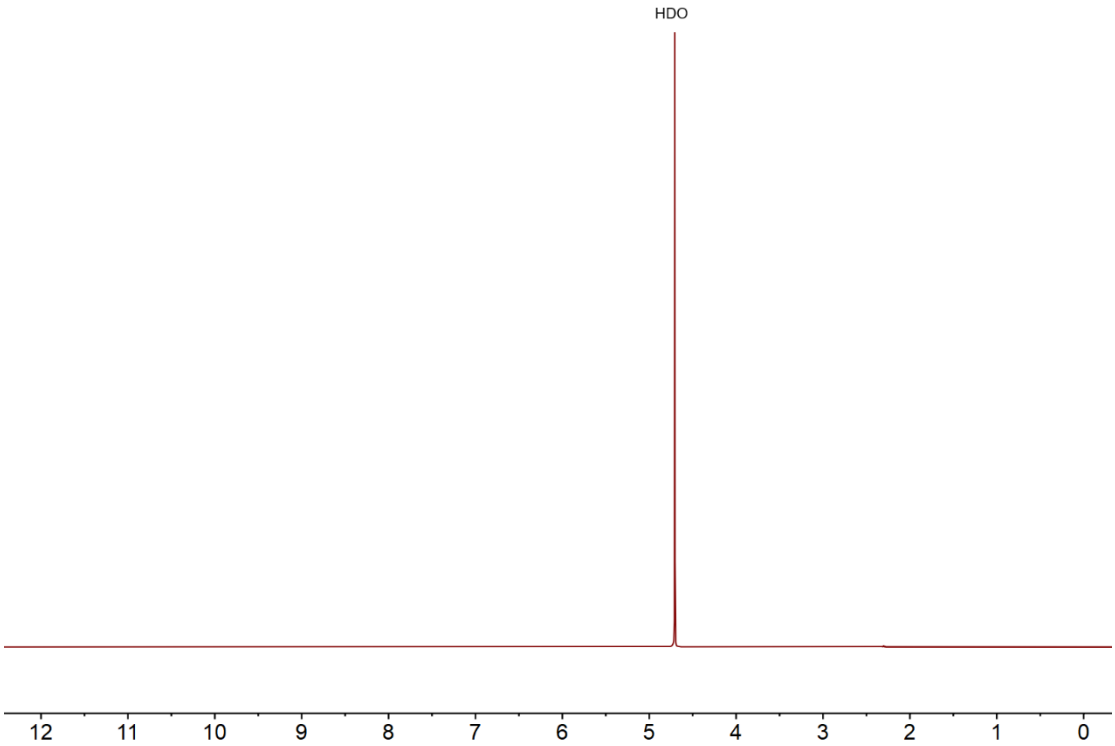

Figure S40. ^{1}H NMR spectrum of poly(**TA**-**A**)$_{8/1}$ immersed in D_2O for 24h.

11. Fourier-transform IR (FT-IR) spectra of poly(TA-TPE)s

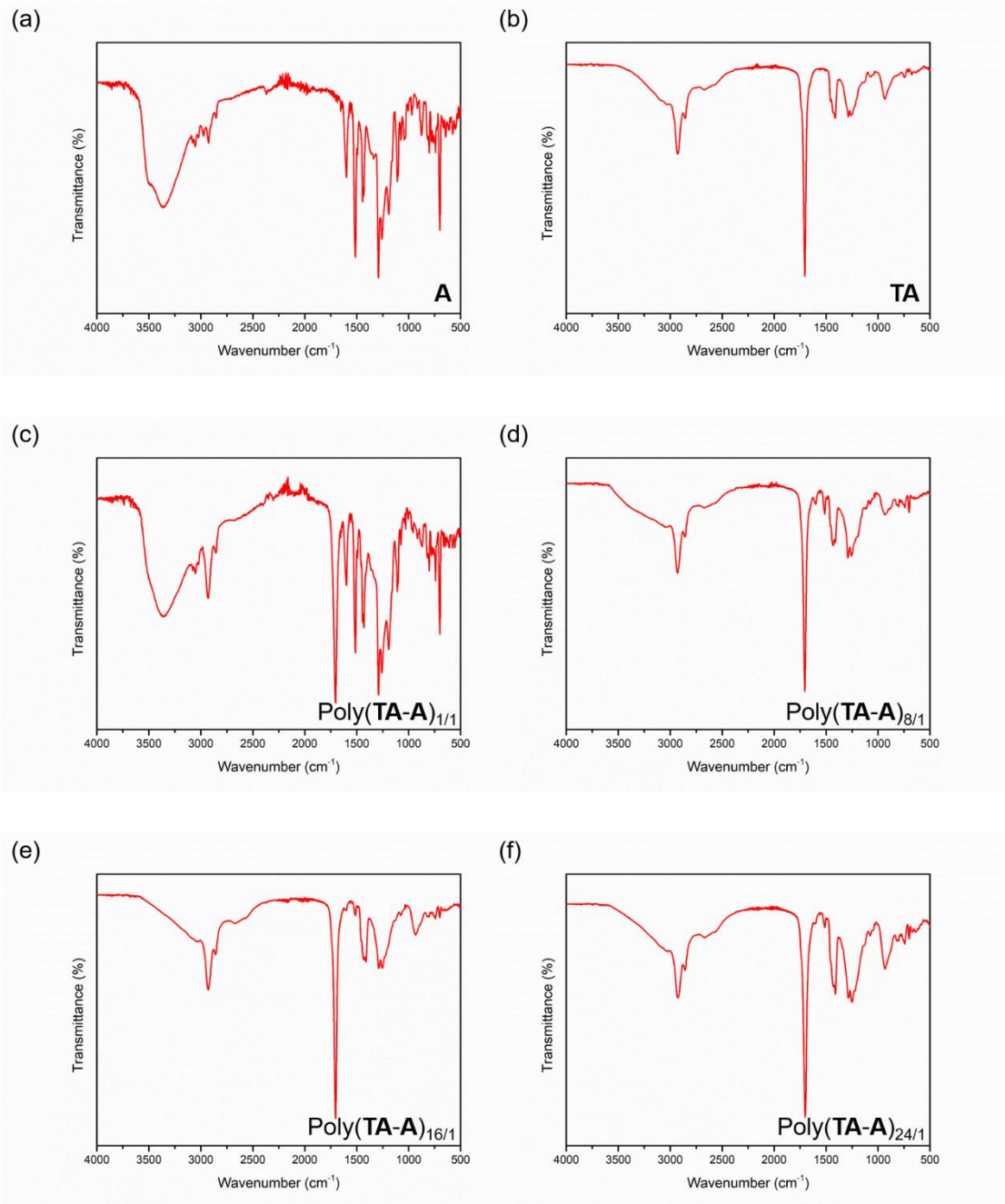

Figure S41. FT-IR spectra of **poly(TA-A)s**: (a) **A**; (b) **TA**; (c) poly(**TA**-**A**)$_{1/1}$; (d) poly(**TA**-**A**)$_{8/1}$; (e) poly(**TA**-**A**)$_{16/1}$; (f) poly(**TA**-**A**)$_{24/1}$.

12. Powder X-Ray diffraction (PXRD) patterns of poly(TA-TPE)s

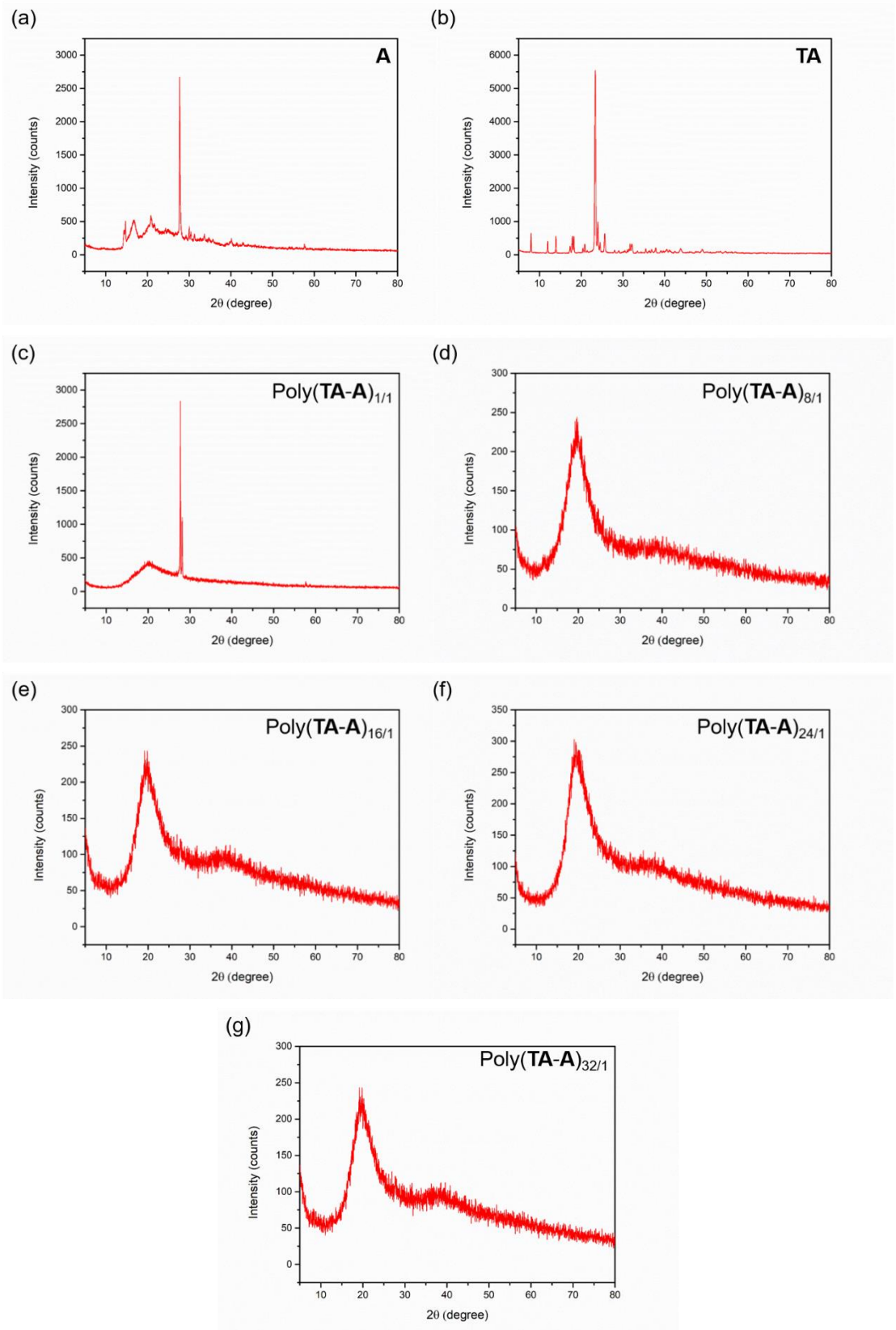

Figure S42. PXRD patterns of poly(**TA**-**A**)s: (a) **A**; (b) **TA**; (c) poly(**TA**-**A**)$_{1/1}$; (d) poly(**TA**-**A**)$_{8/1}$; (e) poly(**TA**-**A**)$_{16/1}$; (f) poly(**TA**-**A**)$_{24/1}$; (e) poly(**TA**-**A**)$_{32/1}$.

13. Thermo-gravimetric analysis (TGA) measurements of poly(TA-TPE)s

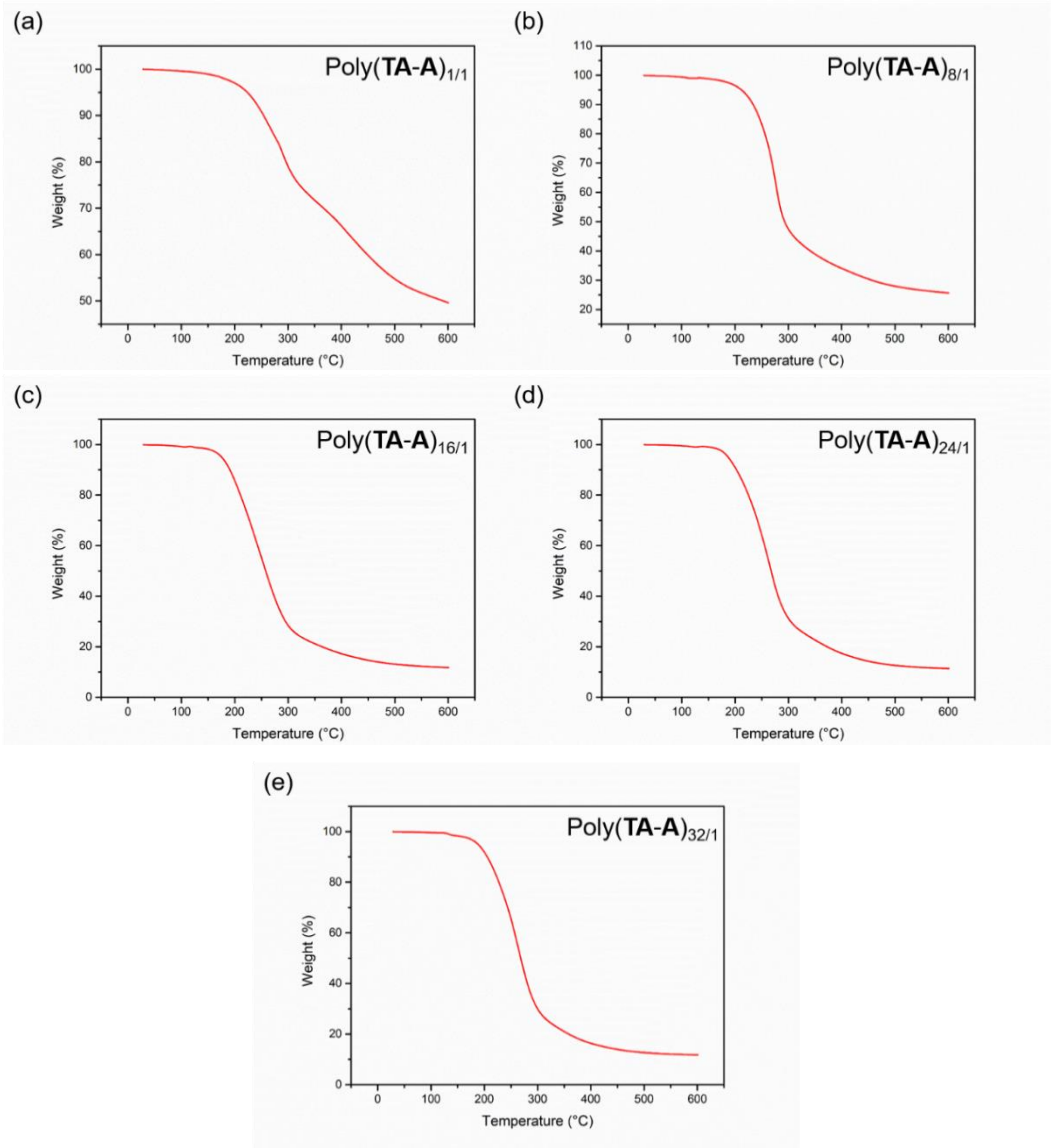

Figure S43. TGA measurements of poly(**TA**-**A**)s: (a) poly(**TA**-**A**)$_{1/1}$; (b) poly(**TA**-**A**)$_{8/1}$; (c) poly(**TA**-**A**)$_{16/1}$; (d) poly(**TA**-**A**)$_{24/1}$; (e) poly(**TA**-**A**)$_{32/1}$.

14. Differential scanning calorimeter (DSC) measurements of poly(TA-TPE)s

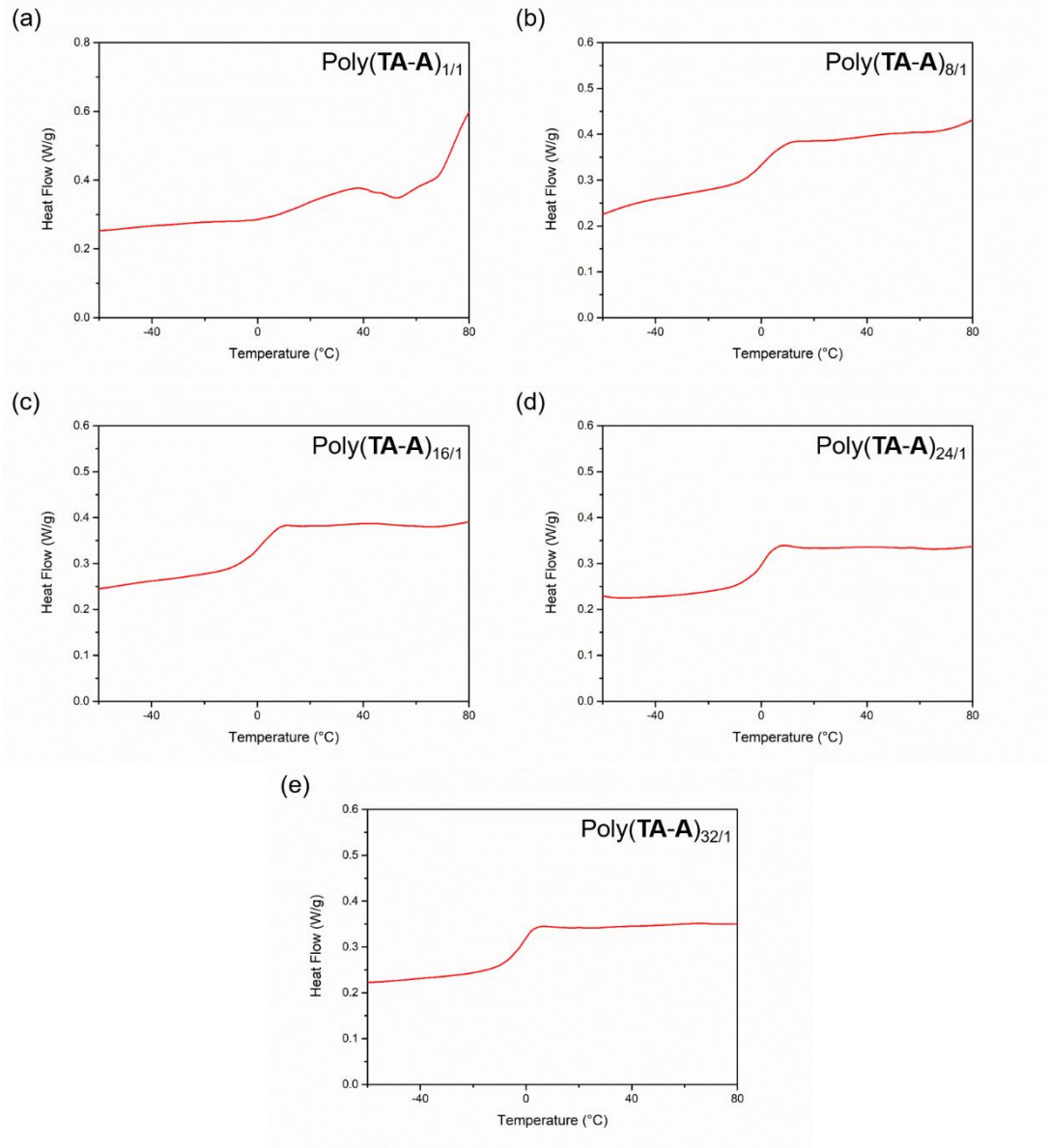

Figure S44. DSC measurements of poly(**TA-A**)s: (a) poly(**TA-A**)$_{1/1}$; (b) poly(**TA-A**)$_{8/1}$; (c) poly(**TA-A**)$_{16/1}$; (d) poly(**TA-A**)$_{24/1}$; (e) poly(**TA-A**)$_{32/1}$.

15. Scanning electron microscopy (SEM) images of poly(TA-TPE)s

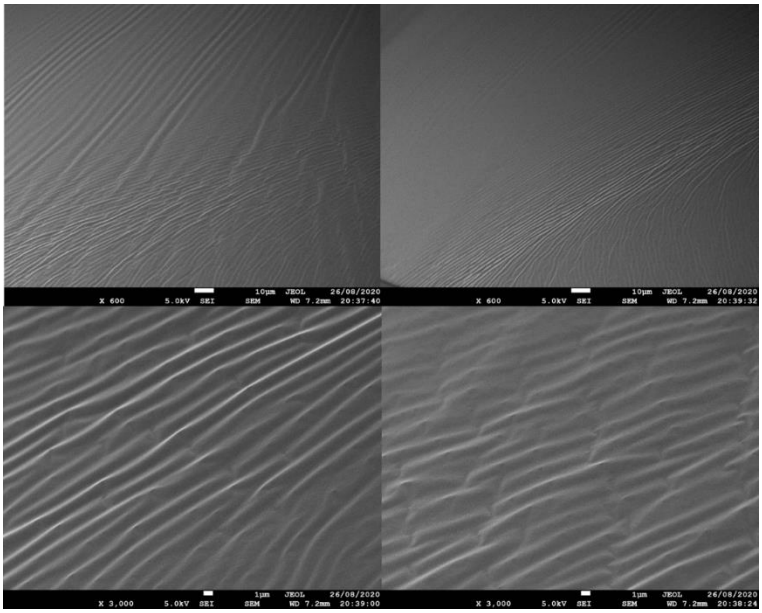

Figure S45. SEM images of poly(**TA**-**A**)$_{8/1}$.

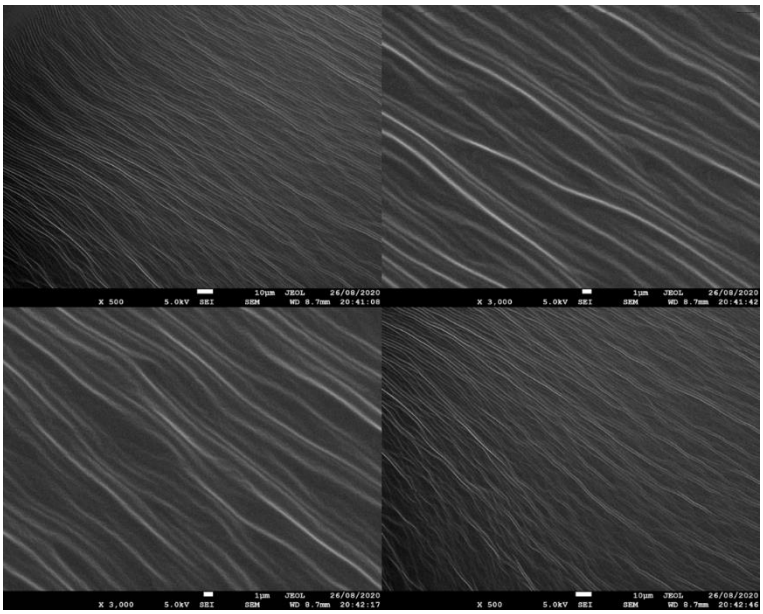

Figure S46. SEM images of poly(**TA**-**A**)$_{16/1}$.

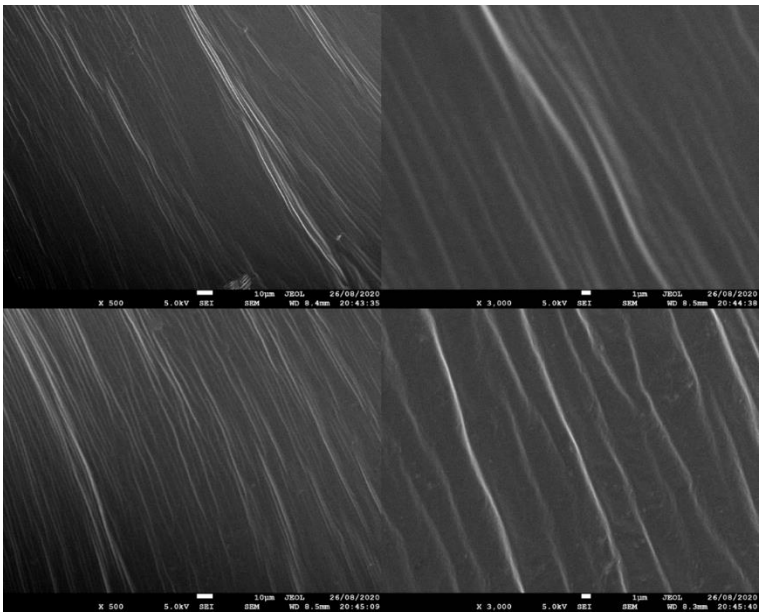

Figure S47. SEM images of poly(**TA**-**A**)$_{24/1}$.

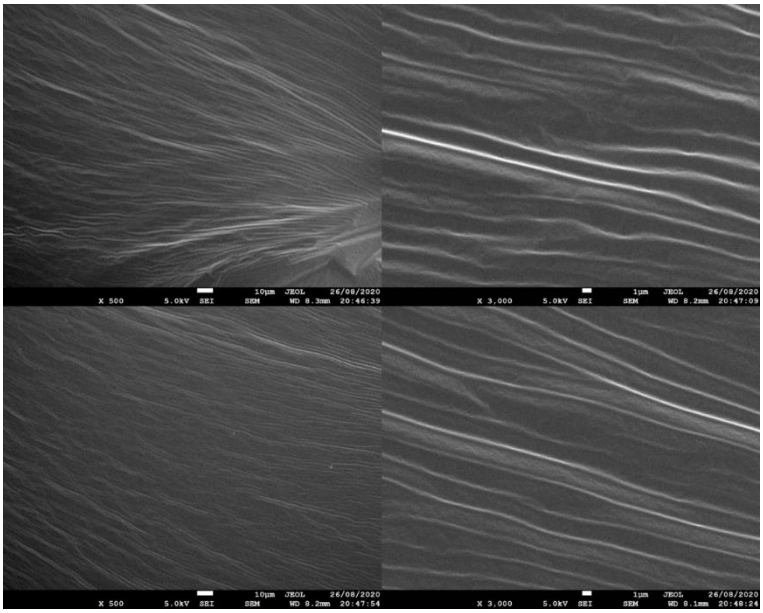

Figure S48. SEM images of poly(**TA**-**A**)$_{32/1}$.

16. DFT Calculation of poly(TA-TPE)$_S$

All DFT calculations were carried out with the Gaussian 16 software. The B3LYP functional was adopted for all calculations. For geometry optimization and frequency calculations, the 6-311G(d) basis set was used, and the optimal geometry for each compound was determined. The DFT-D3 with BJ-damping was applied to correct the weak interaction to improve the calculation accuracy.[3,4]

a) Gibbs free energy of **A**/**TA**, molar ratio 1:1: –6.74 kcal/mol (298.15 K).
Combination energy of **A**/**TA**, molar ratio 1:1: –29.07 kcal/mol (298.15 K).

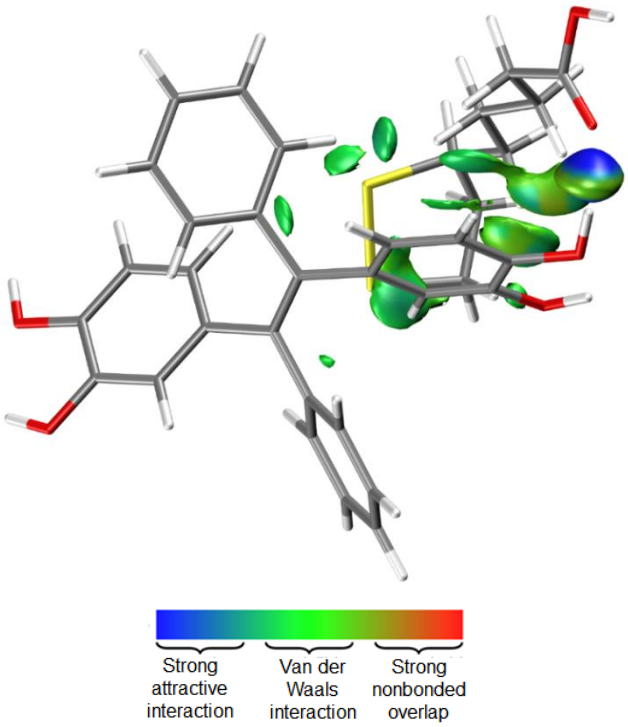

Figure S49. The independent gradient model (IGM) isosurfaces for the interaction between **A** and **TA** (molar ratio 1:1), and the color bar shows that blue, green, and red represent strong attraction interactions (hydrogen bonding), van der Waals interactions, and strong nonbonded overlap, respectively.

b) Gibbs free energy of **B**/**TA**, molar ratio 1:1: –9.64 kcal/mol (298.15 K).

Combination energy of **B**/**TA**, molar ratio 1:1: –32.21 kcal/mol (298.15 K).

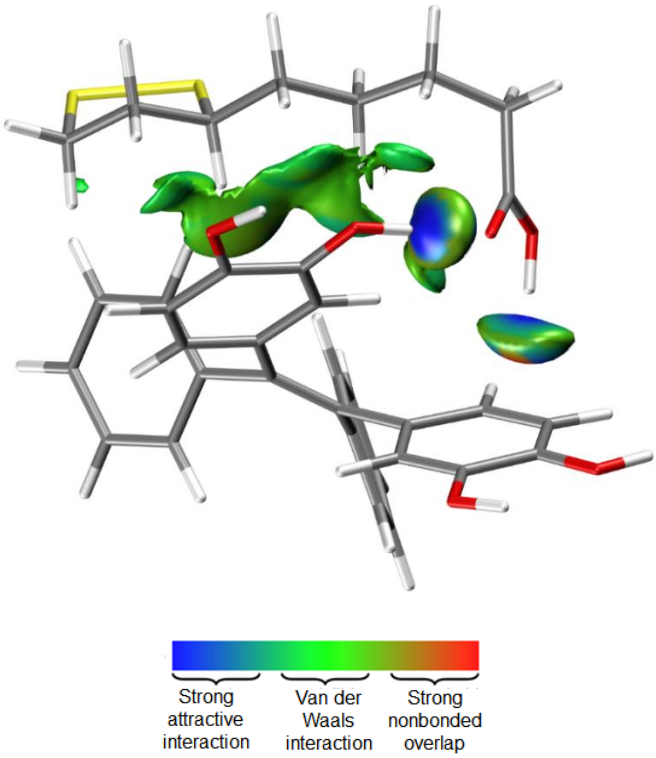

Figure S50. The independent gradient model (IGM) isosurfaces for the interaction between **B** and **TA** (molar ratio 1:1), and the color bar shows that blue, green, and red represent strong attraction interactions (hydrogen bonding), van der Waals interactions, and strong nonbonded overlap, respectively.

c) Gibbs free energy of **C**/**TA**, molar ratio 1:1: –7.62 kcal/mol (298.15 K).

Combination energy of **C**/**TA**, molar ratio 1:1: –27.68 kcal/mol (298.15 K).

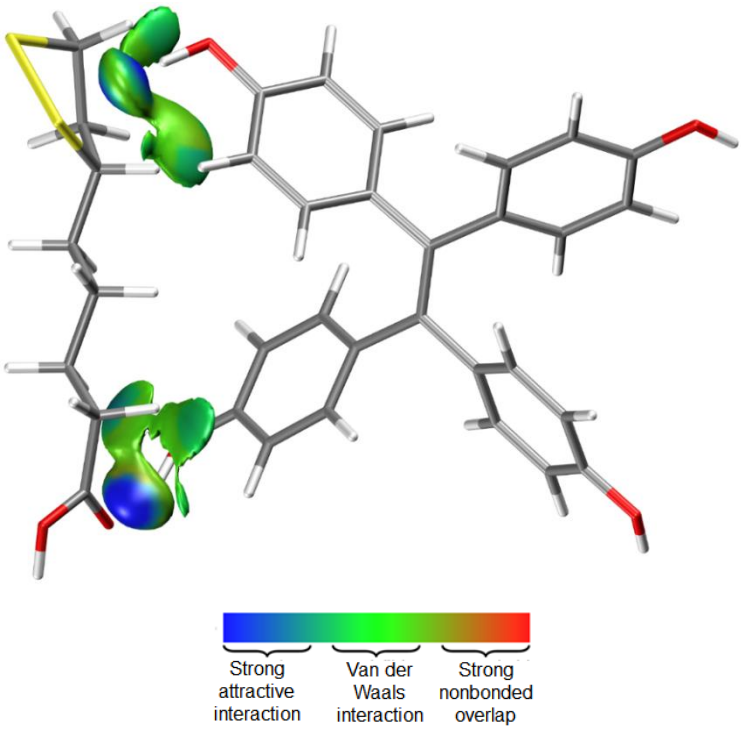

Figure S51. The independent gradient model (IGM) isosurfaces for the interaction between **C** and **TA** (molar ratio 1:1), and the color bar shows that blue, green, and red represent strong attraction interactions (hydrogen bonding), van der Waals interactions, and strong nonbonded overlap, respectively.

d) Gibbs free energy of **D**/**TA**, molar ratio 1:1: –9.36 kcal/mol (298.15 K).

Combination energy of **D**/**TA**, molar ratio 1:1: –32.06 kcal/mol (298.15 K).

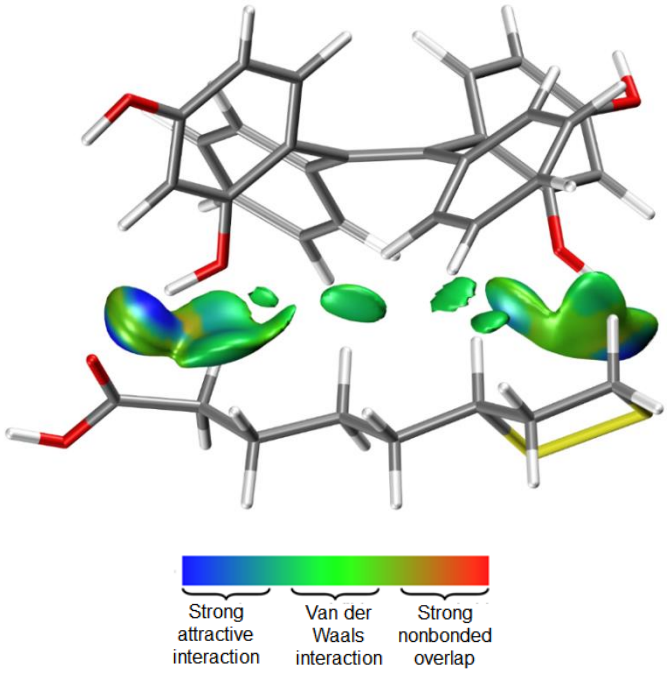

Figure S52. The independent gradient model (IGM) isosurfaces for the interaction between **D** and **TA** (molar ratio 1:1), and the color bar shows that blue, green, and red represent strong attraction interactions (hydrogen bonding), van der Waals interactions, and strong nonbonded overlap, respectively.

17. Films prepared by poly(TA-TPE)s

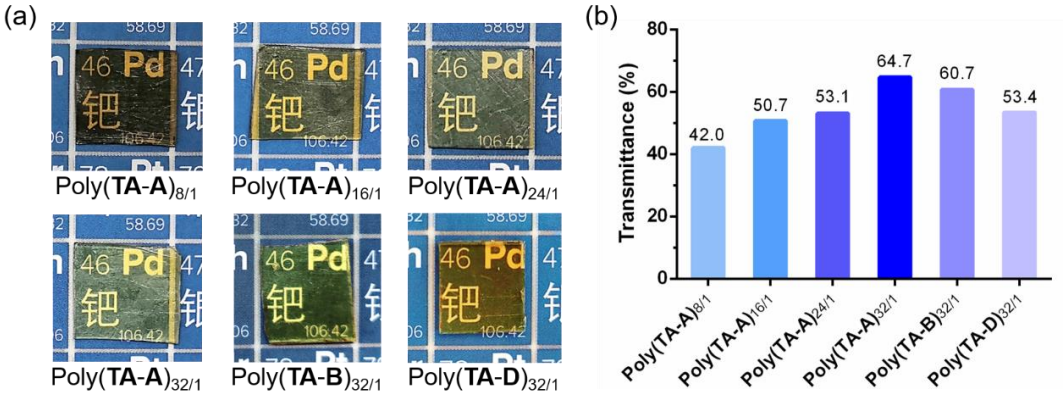

Figure S53. (a) Films prepared by poly(**TA**-**TPE**)s (15×15×0.8 mm^3) and (b) their transmittances at wavelength of 550 nm.

18. Contact angles of poly(TA-TPE)$_S$

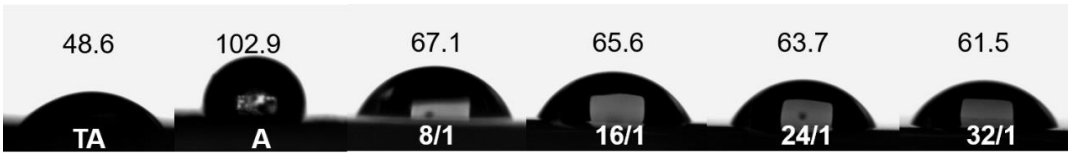

Figure S54. Contact angles of **A**, **TA** and poly(**TA**-**A**)s.

19. Stress–strain curves of poly(TA-TPE)s

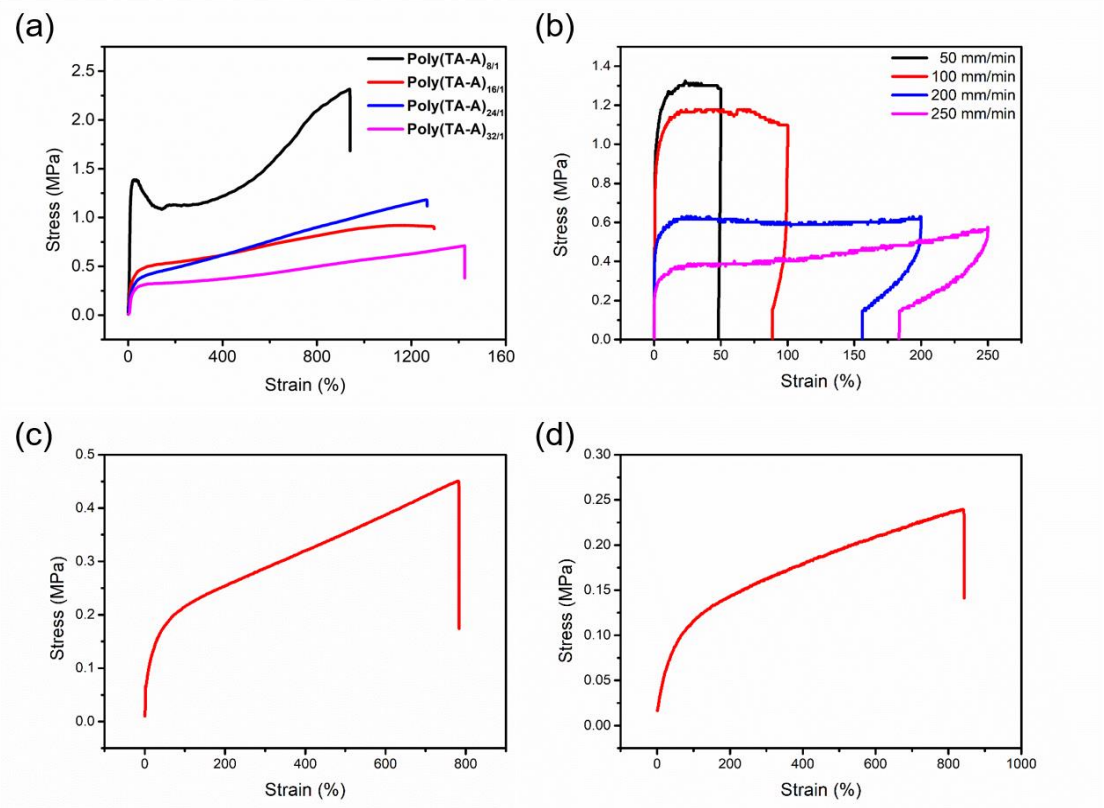

Figure S55. (a) Stress–strain curves of poly(**TA**-**A**)s at a loading rate of 50 mm/min; (b) sequential loading-unloading stress–strain curves of poly(**TA**-**A**)$_{8/1}$ with no resting internals at a loading rate of 50 mm/min; (c) stress–strain curve of poly(**TA**-**B**)$_{32/1}$ at a loading rate of 50 mm/min; (d) stress–strain curve of poly(**TA**-**D**)$_{32/1}$ at a loading rate of 50 mm/min.

20. Macroscopic views of poly(TA-TPE)s at different temperatures

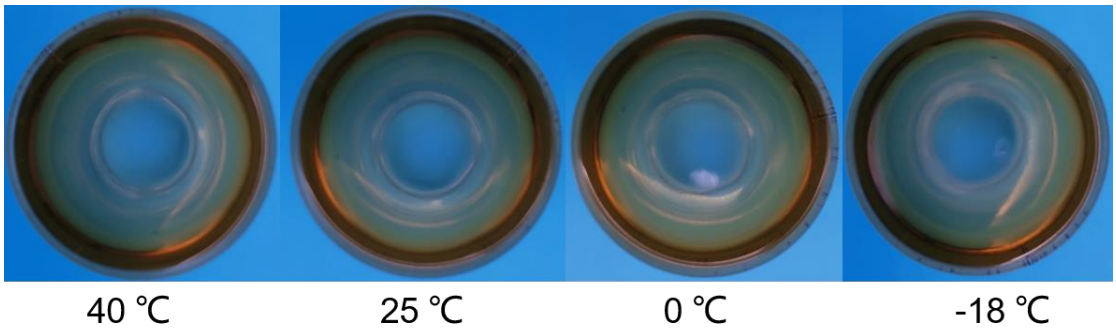

Figure S56. Macroscopic views of poly(**TA**-**A**)$_{8/1}$ at different temperatures.

21. Rheology measurements of poly(TA-TPE)$_S$

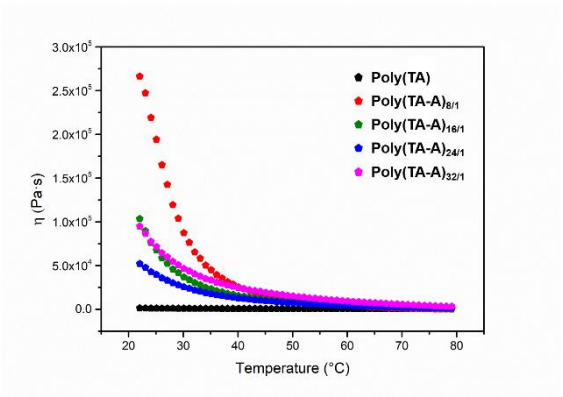

Figure S57. Temperature-dependent composite viscosity (η) of poly(**TA**-**A**)s.

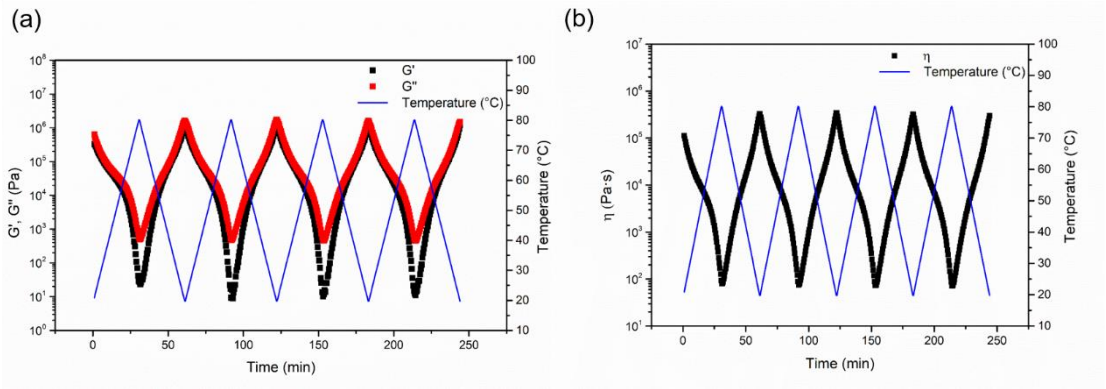

Figure S58. Reversible temperature-dependent rheological tests of poly(**TA**-**A**)$_{8/1}$: (a) storage modulus (*G'*) and loss modulus (*G''*) values; (b) composite viscosity (η) values.

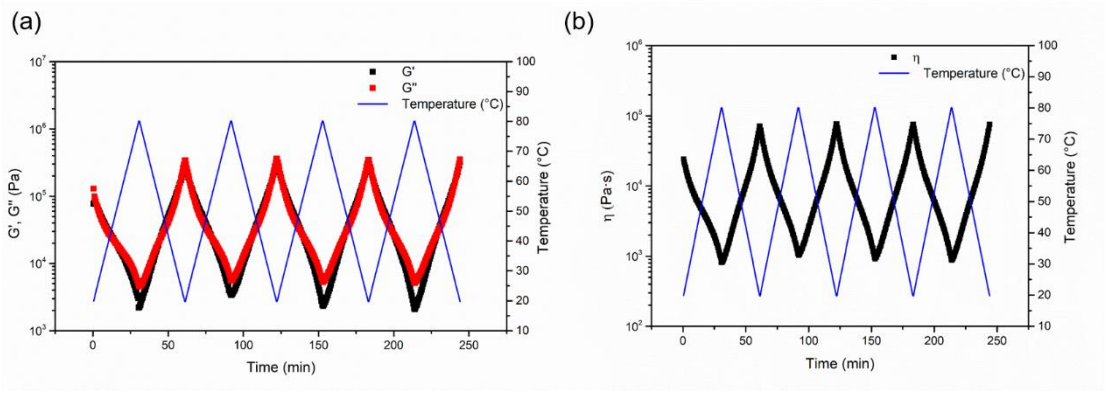

Figure S59. Reversible temperature-dependent rheological tests of poly(**TA**-**A**)$_{16/1}$: (a) storage modulus (*G*') and loss modulus (*G*'') values; (b) composite viscosity (η) values.

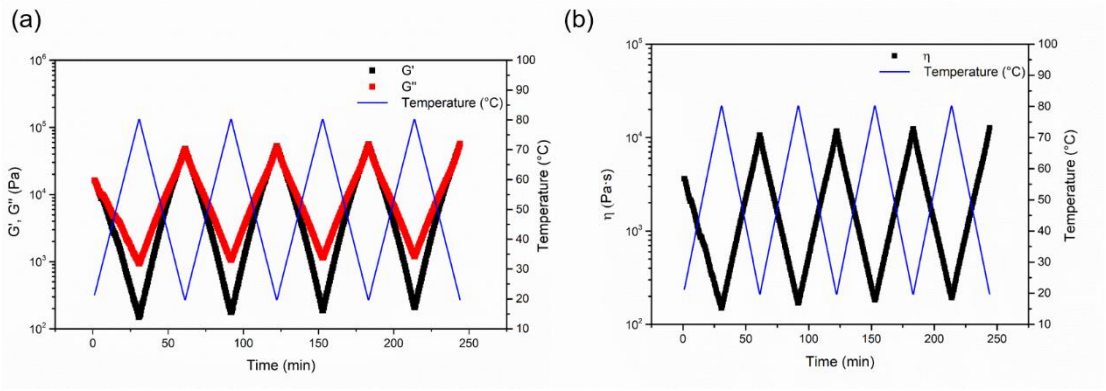

Figure S60. Reversible temperature-dependent rheological tests of poly(**TA**-**A**)$_{24/1}$: (a) storage modulus (*G*') and loss modulus (*G*'') values; (b) composite viscosity (η) values.

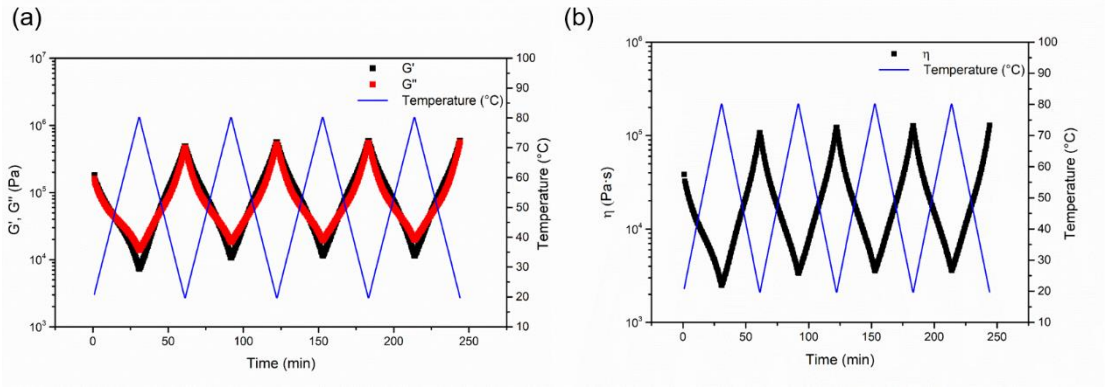

Figure S61. Reversible temperature-dependent rheological tests of poly(**TA**-**A**)$_{32/1}$: (a) storage modulus (*G*') and loss modulus (*G*'') values; (b) composite viscosity (η) values.

22. Concentration-dependent rheology measurements of poly(TA-TPE)s

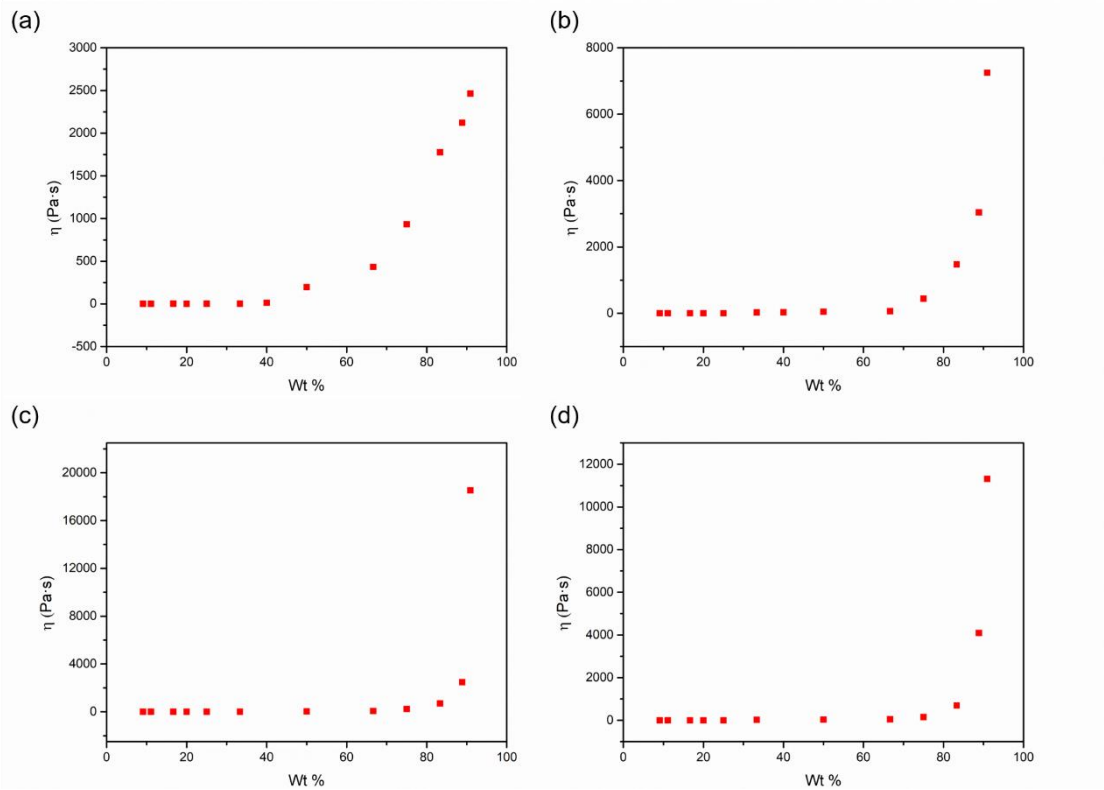

Figure S62. Concentration-dependent composite viscosity (η) at 25 °C: (a) poly(**TA**-**A**)$_{8/1}$, (b) poly(**TA**-**A**)$_{16/1}$, (c) poly(**TA**-**A**)$_{24/1}$, (d) poly(**TA**-**A**)$_{32/1}$. The solvent is CH_3CH_2OH.

23. Dynamic mechanical analyzer (DMA) measurement of poly(TA-A)$_{8/1}$

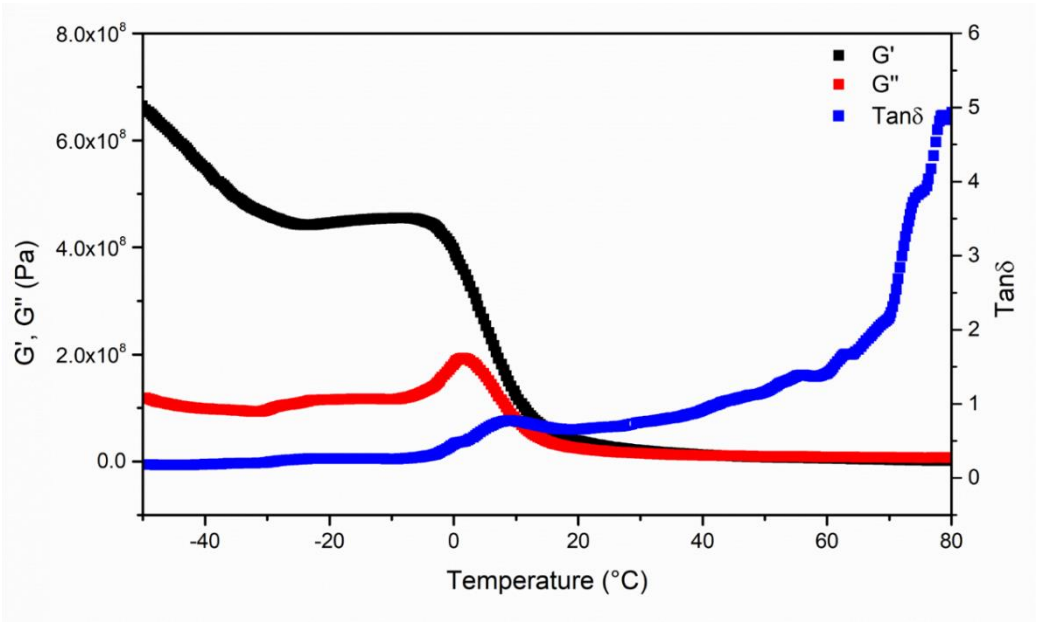

Figure S63. DMA measurement of poly(**TA**-**A**)$_{8/1}$.

24. Self-healing properties of poly(TA-A)$_{32/1}$

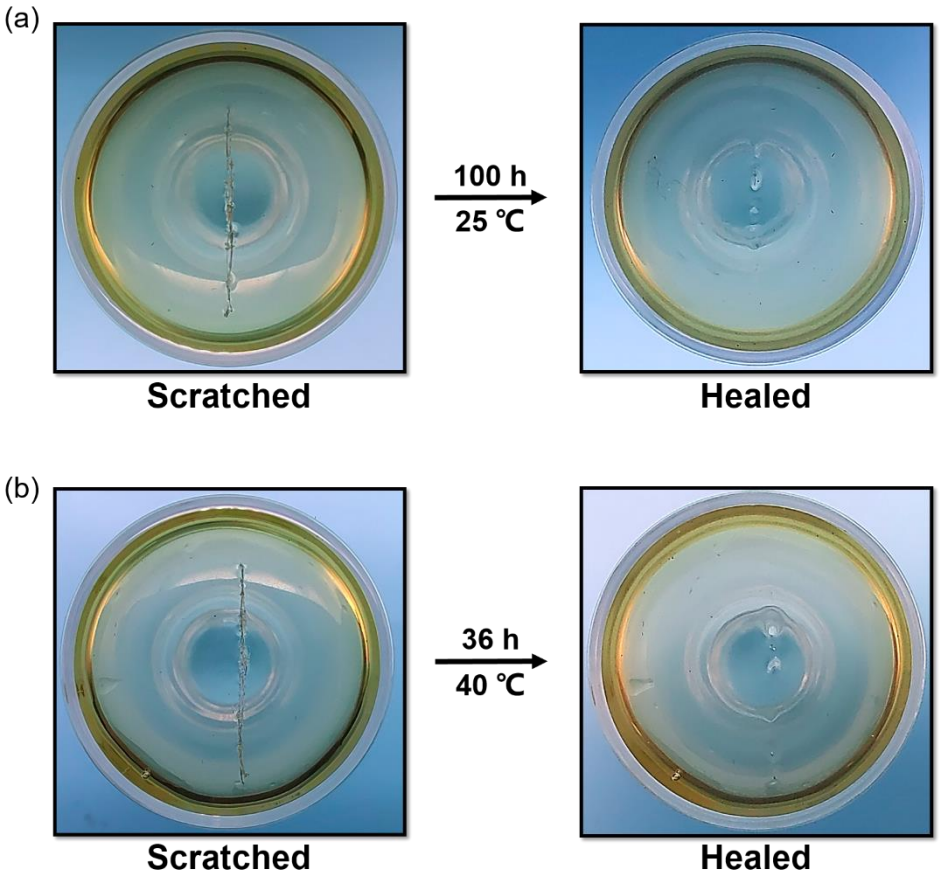

Figure S64. Self-healing properties of poly(**TA-A**)$_{32/1}$ at different temperatures: (a) 25 °C; (b) 40 °C.

25. UV-Vis spectra of TPEs

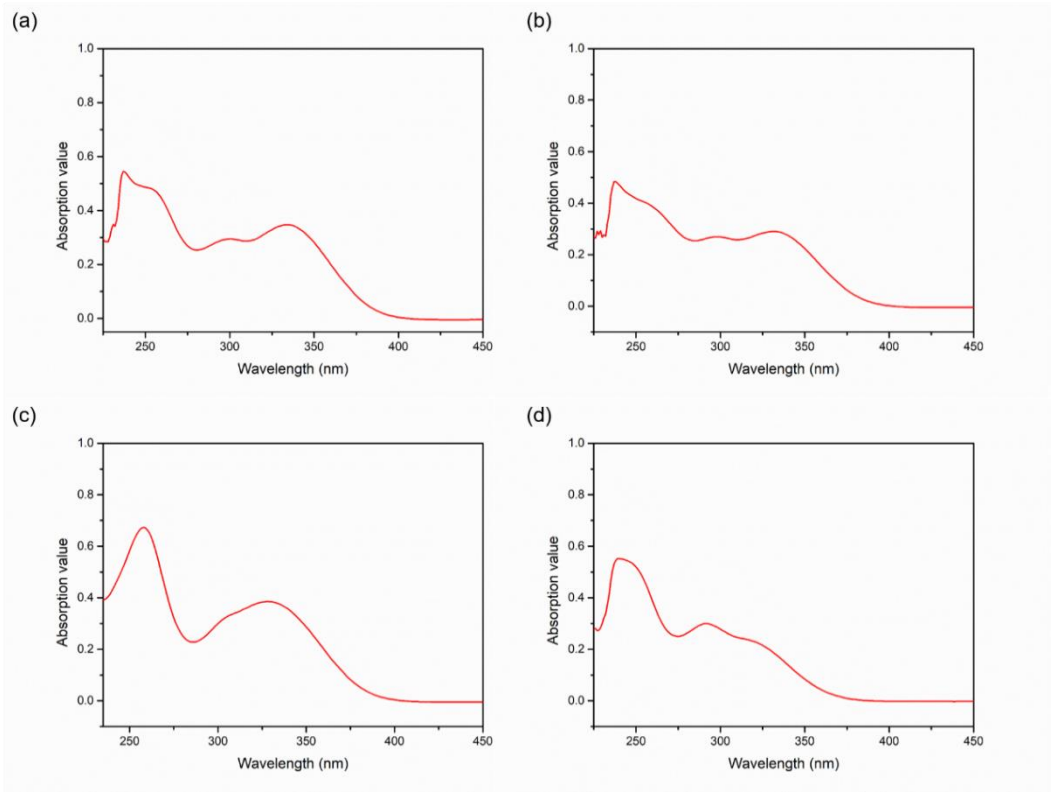

Figure S65. UV-Vis spectra of **TPE**s in CH_3CH_2OH (0.01 mg/mL): (a) **a**; (b) **b**; (c) **c**; (d) **d**.

26. Fluorescent emission spectra of TPEs

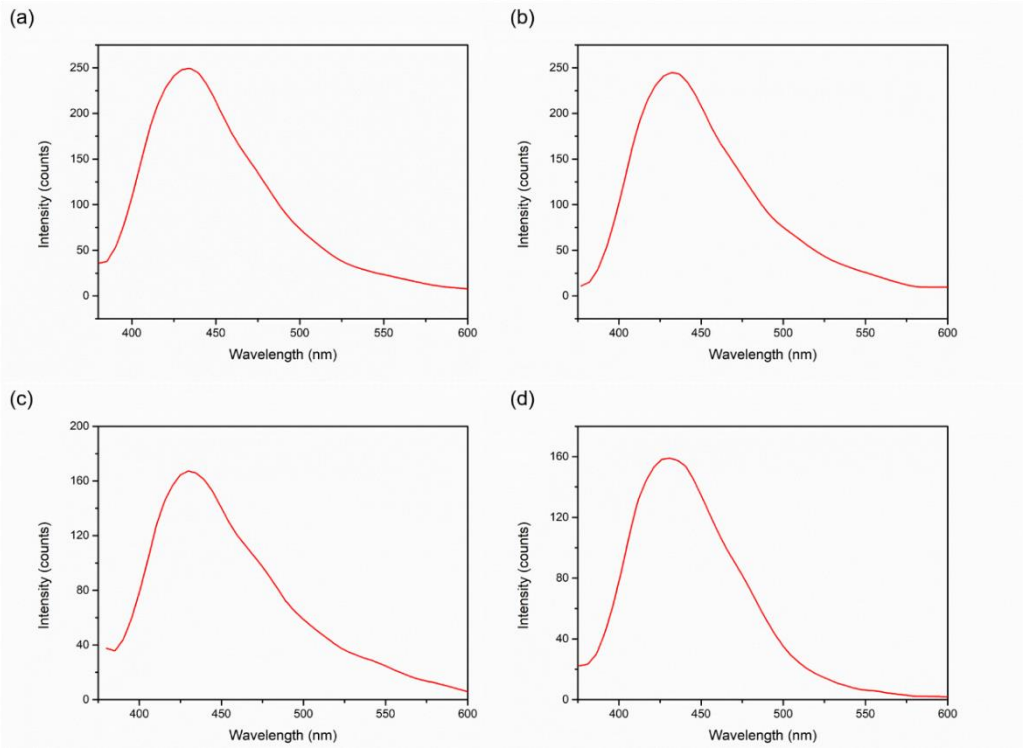

Figure S66. Fluorescent emission spectra of **TPE**s in CH_3CH_2OH (0.01 mg/mL): (a) **a** (excitation wavelength: 371 nm); (b) **b** (excitation wavelength: 367 nm); (c) **c** (excitation wavelength: 371 nm); (d) **d** (excitation wavelength: 366 nm).

27. UV-Vis spectra of poly(TA-TPE)s

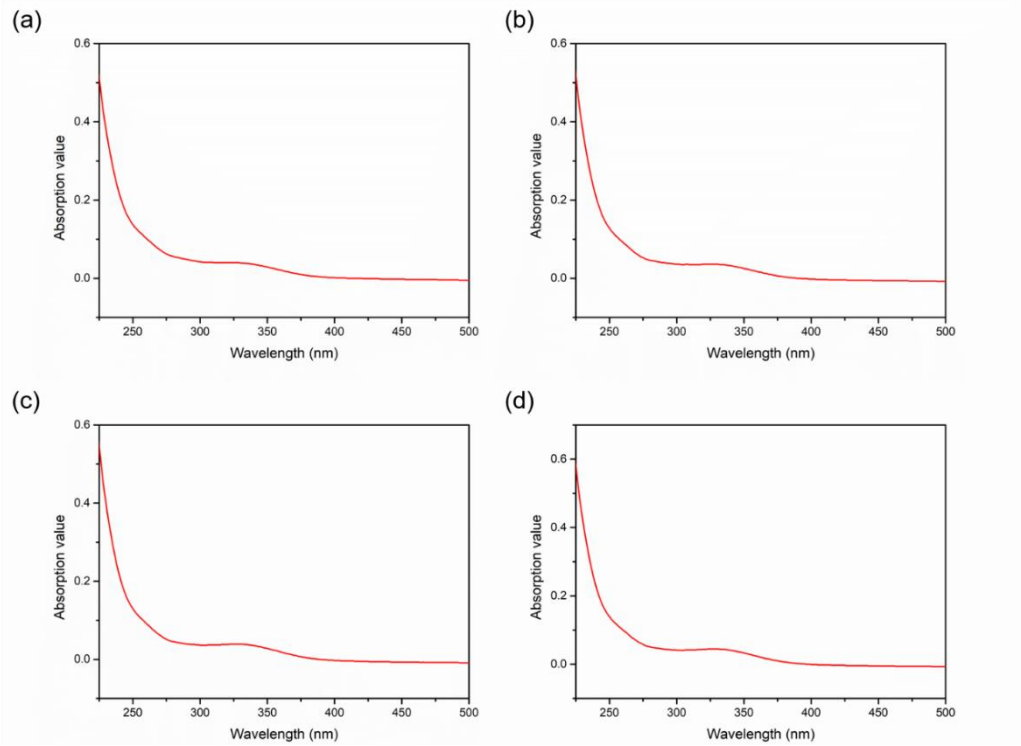

Figure S67. UV-Vis spectra of poly(**TA**-**A**)s in CH_3CH_2OH (0.001 mg/mL): (a) **A**; (b) poly(**TA**-**A**)$_{8/1}$; (c) poly(**TA**-**A**)$_{16/1}$; (d) poly(**TA**-**A**)$_{24/1}$.

28. Fluorescent emission spectra of poly(TA-TPE)s

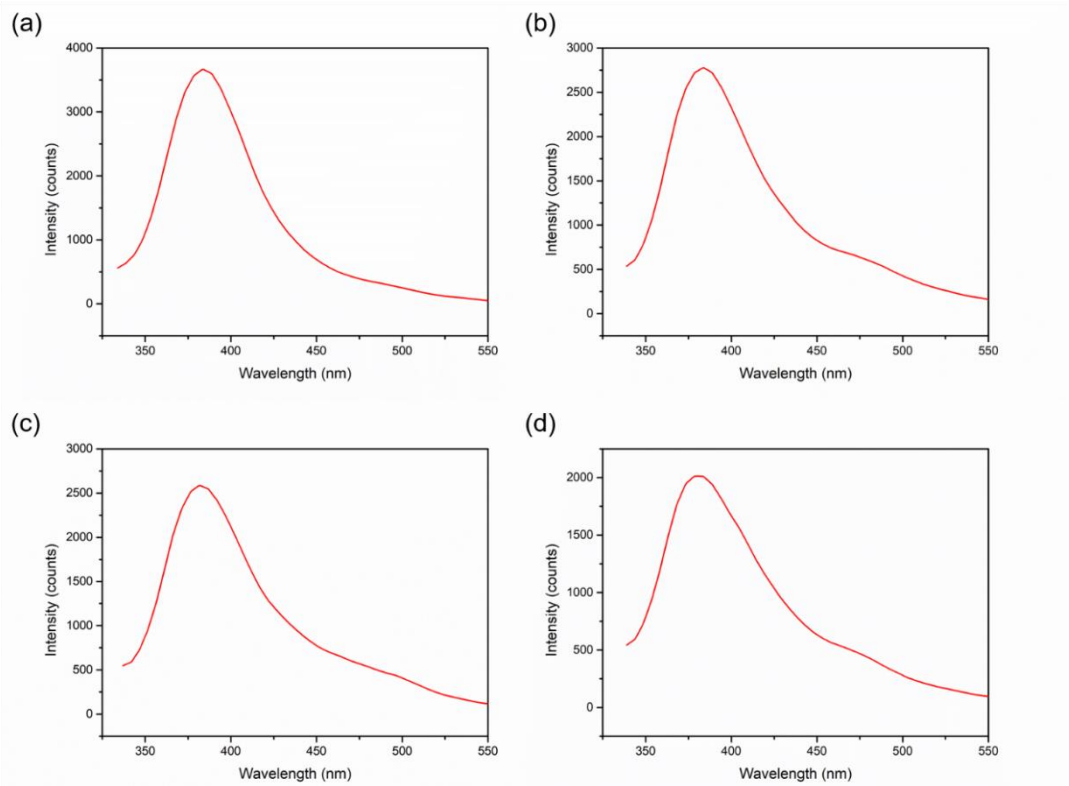

Figure S68. Fluorescent emission spectra of poly(**TA**-**A**)s in CH_3CH_2OH (0.001 mg/mL): (a) **A** (excitation wavelength: 324 nm); (b) poly(**TA**-**A**)$_{8/1}$ (excitation wavelength: 329 nm); (c) poly(**TA**-**A**)$_{16/1}$ (excitation wavelength: 329 nm); (d) poly(**TA**-**A**)$_{24/1}$ (excitation wavelength: 329 nm).

29. Absolute fluorescence quantum yields of poly(TA-TPE)s

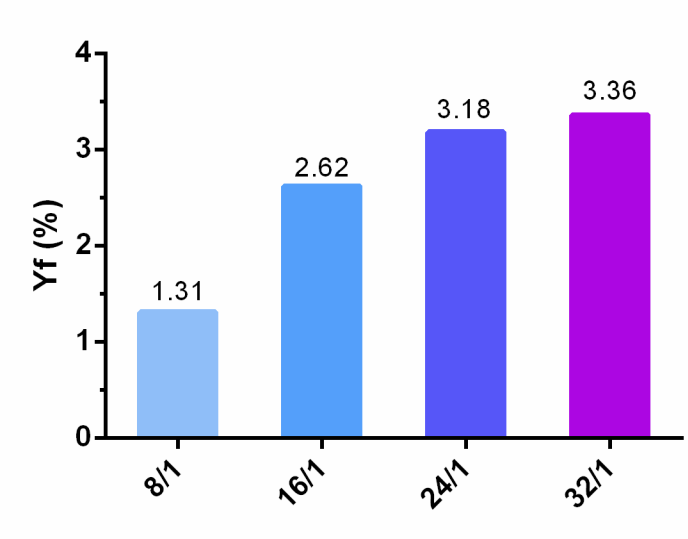

Figure S69. Absolute fluorescence quantum yields of poly(**TA**-**A**)s.

30. Underwater luminescence of poly(TA-TPE)s under different conditions

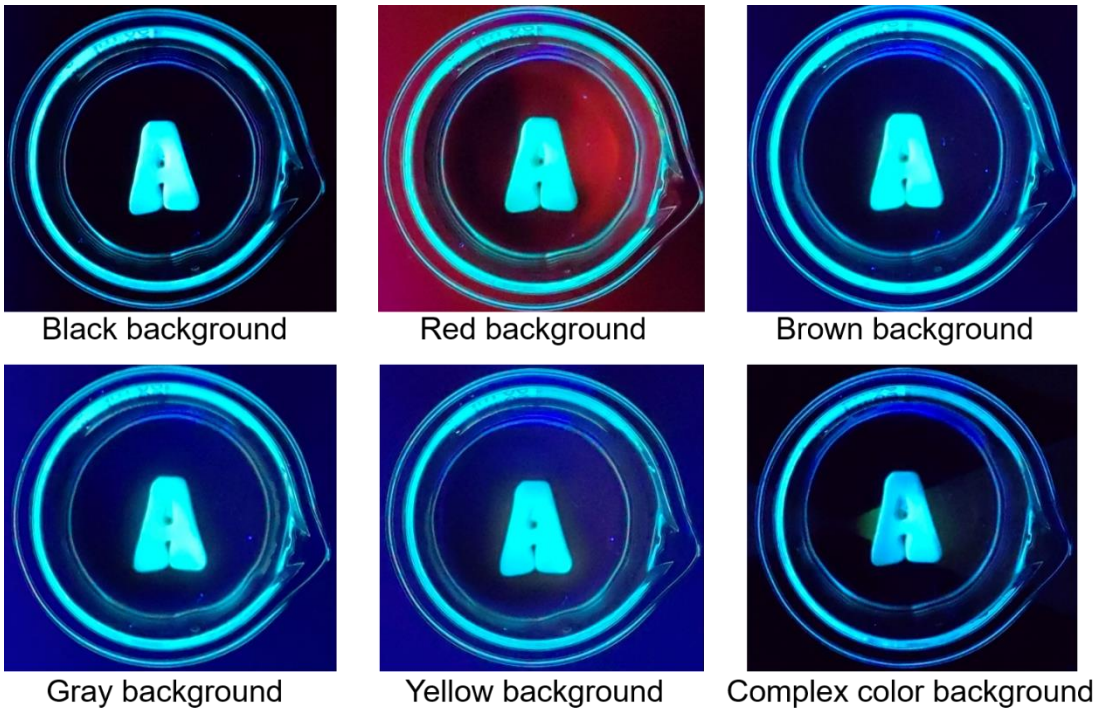

Figure S70. Underwater luminescence of poly(**TA**-**A**)$_{8/1}$ was placed above colorful background.

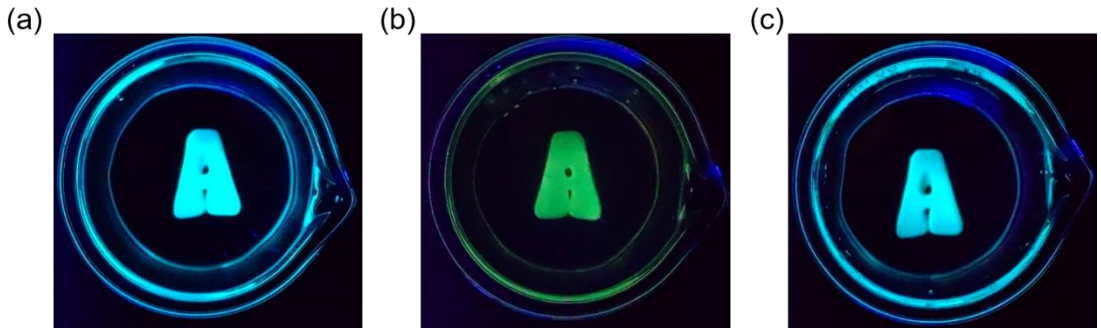

Figure S71. Luminescence of poly(**TA**-**A**)$_{8/1}$ in contaminated water: (a) methyl blue aqueous solution; (b) methyl orange aqueous solution; (c) $CuSO_4$ aqueous solution.

31. Quantitative adhesion experiments of poly(TA-TPE)s

Preparation of adhesive layer: molten poly(**TA**-**TPE**)s were quickly coated on the surface of the test substrate, and then covered with a new test substrate. Press and stand for 2 hours (unless the time is specially specified) under the test conditions, and then conduct the lap-shear test.

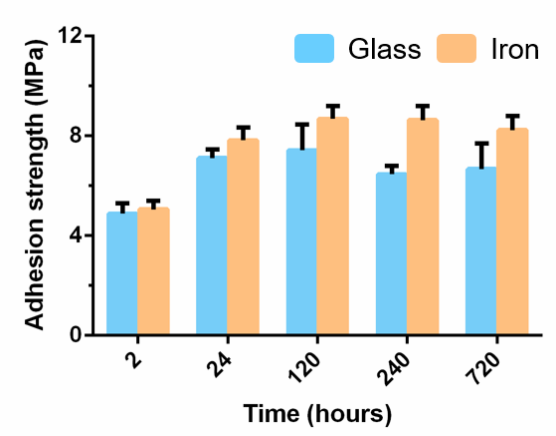

Figure S72. Time-dependent adhesion strengths of poly(**TA**-**A**)$_{8/1}$ under ambient conditions (25 ℃, RH: 50%).

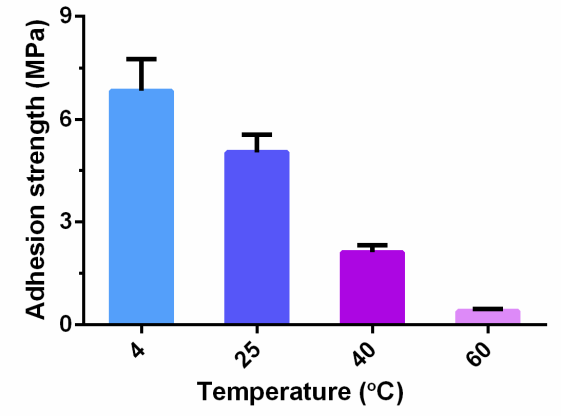

Figure S73. Adhesion strengths of poly(**TA**-**A**)$_{8/1}$ to glass in water at different temperatures.

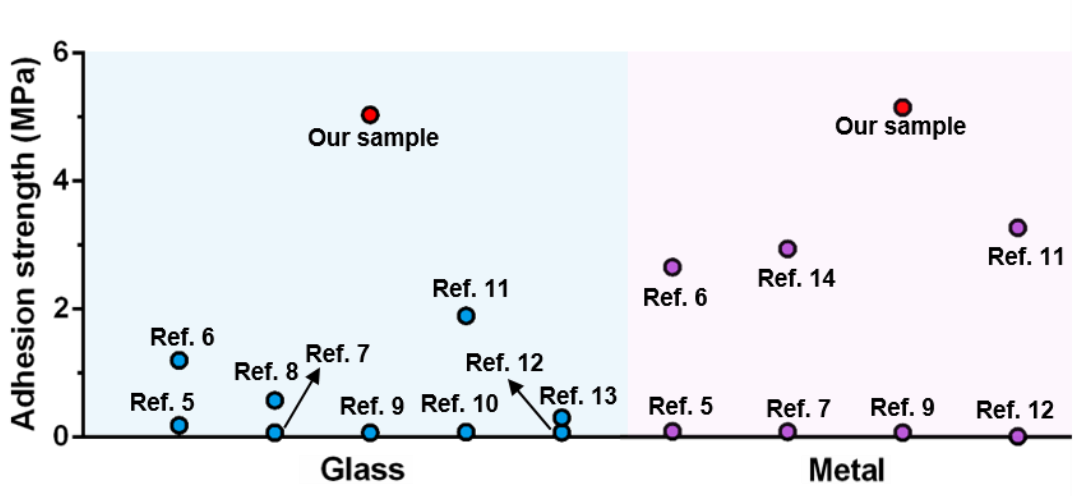

Figure S74. Underwater adhesion strengths of poly(**TA**-**A**)$_{8/1}$ adhesives compared to other adhesives reported in the literature.

Magnitude comparison of underwater adhesion strengths between poly(**TA**-**A**)$_{8/1}$ adhesive and other kinds of adhesives reported by the literature on glass/metel, as the **Figure S74** in the revised supporting information as well as below. It can be clearly seen that the adhesion strength of the poly(**TA**-**A**)$_{8/1}$ adhesive is superior to the performance of many adhesives in the wet condition.

32. Macroscopic adhesion tests of poly(TA-TPE)s

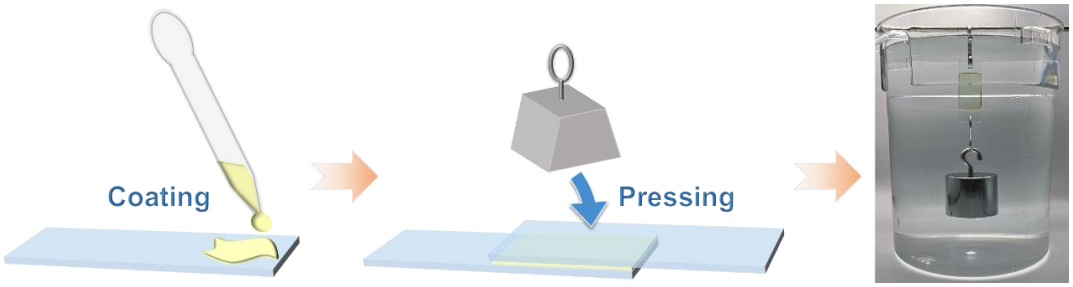

Figure S75. Adhesion process of poly(**TA**-**TPE**)s.

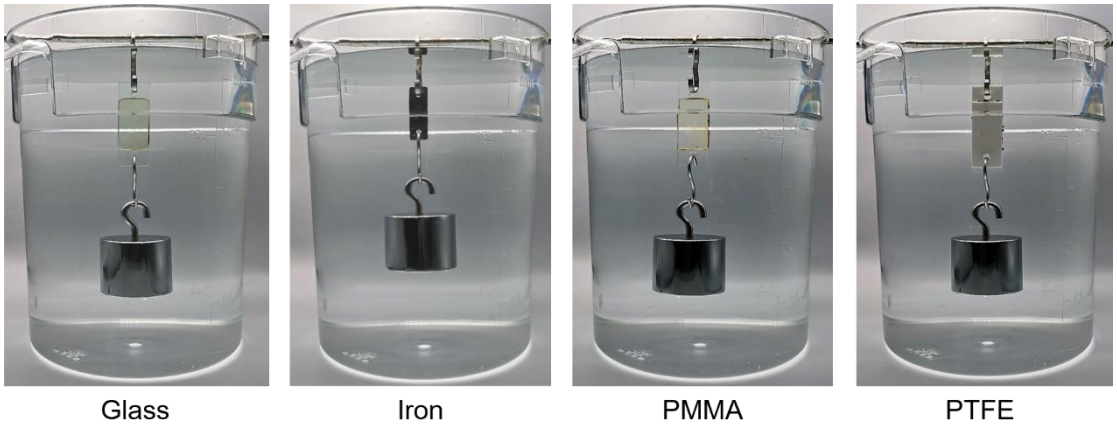

Figure S76. Water-resistant adhesion tests of poly(**TA**-**A**)$_{8/1}$ on different surfaces.

Figure S77. Underwater adhesion test of poly(**TA**-**A**)$_{8/1}$.

Figure S78. Water blasting (2 bar, 10 min) test of poly(**TA**-**A**)$_{8/1}$.

33. Molecular dynamics study of poly(TA-TPE)s

In order to study the intermolecular interaction of poly(**TA**-**TPE**)s, the cohesive energy density (CED) was calculated by Molecular Dynamics Simulation.[5,6] In this work, molecular models of poly(**TA**-**TPE**)s were respectively built using Materials Studio (V.8.0, Accelrys, San Diego, USA) as shown in **Figure S79**. The Condensed-Phase Optimized Potentials for Atomistic Simulation Studies (COMPASSII) force field was used. The COMPASSII force field, the first ab initio force-field, is commonly used to provide the atomic interactions. Then, the Ewald method and the atom-based method were employed for analyzing the Coulomb interactions and the van der Waals (VDW) interactions of poly(**TA**-**TPE**)s. In order to obtain a reasonable interaction configuration, a geometry optimization using smart method with an energy convergence criterion of 10^{-5} kcal/mol and force convergence criteria of 10^{-4} kcal/mol/Å was used to get a global minimum energy configuration. To further equilibrate the model, a 3-cycles thermal annealing from 25 °C and 227 °C was processed, then back to 25 °C with 50 °C intervals. In the annealing process, the construct was further relaxed to obtain a stable state with a local energy minimum. The cell was followed by 800 ps process under the constant pressure and the constant temperature (NPT ensemble) at a room temperature of 25 °C and atmospheric pressure of 101 kPa with 1 ps time step. During the simulation, Nose thermostat and Berendsen barostat algorithm were applied in the temperature and pressure control. The Ewald summation method was applied to calculate the electrostatic interactions with an accuracy of 10^{-3} kcal/mol.

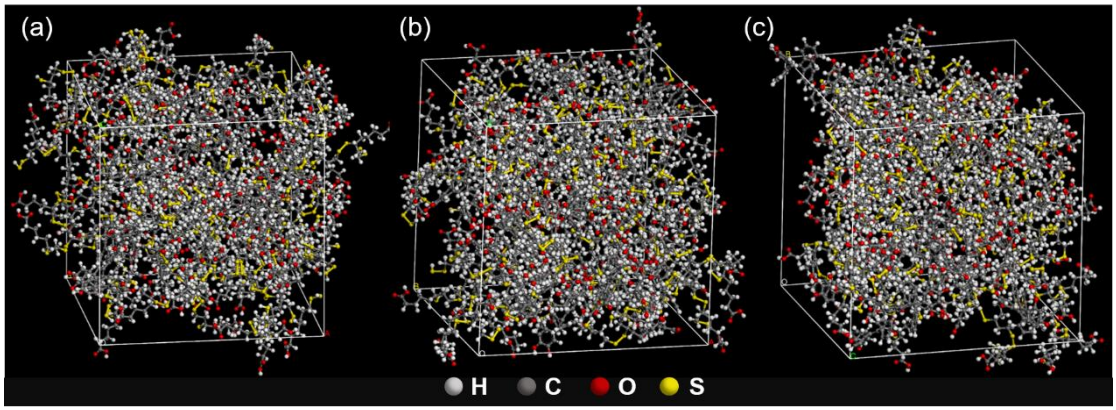

Figure S79. (a) Configurations of molecular models of poly(**TA**-**A**)$_{8/1}$ cluster (4.0×4.0×4.0 nm^3); (b) Configurations of molecular models of poly(**TA**-**B**)$_{8/1}$ cluster (4.0×4.0×4.0 nm^3); (c) Configurations of molecular models of poly(**TA**-**D**)$_{8/1}$ cluster (4.0×4.0×4.0 nm^3).

Table S2. The cohesive energy density (CED) of poly(**TA**-**TPE**)s.

Adhesive	CED (J/m^3)
poly(**TA**-**A**)$_{8/1}$	4.74×10^8
poly(**TA**-**B**)$_{8/1}$	5.21×10^8
poly(**TA**-**D**)$_{8/1}$	4.74×10^8

To further explore the adhesion behavior of poly(**TA**-**TPE**)s to glass, the interaction mechanisms were studied using molecular dynamics simulations from an atomic level. Firstly, two periodical layers molecular model of poly(**TA**-**TPE**)s and glass were built in Materials Studio (V.8.0, Accelrys, San Diego, USA), as shown in **Figure S80**. The geometry optimization was subjected with smart algorithm under the COMPASSII forcefield which enables precise calculation for adhesives with glass in a wide range. To further reduce energy and abtain reasonable configuration, a 3-cycles thermal annealing from 25 °C and 227 °C was processed, then back to 25 °C with 50 °C intervals. The configuration corresponding to minimum energy was extracted for further dynamics simulation. Then, an NVT dynamic balance was carried out at 25 °C for 800 ps. Finally, the interaction potential energy ($E_{interfacial}$) of the interfacial region between adhesive and glass were calculated based on the following equation:

$$E_{interfacial}=E_{total}-(E_{adhesive}+E_{glass})$$

$E_{interfacial}$: Interaction energy between adhesive and glass, minus means adsorption.

E_{total}: The total potential energy of system.

$E_{adhesive}$: The potential energy of adhesive.

E_{glass}: The potential energy of glass.

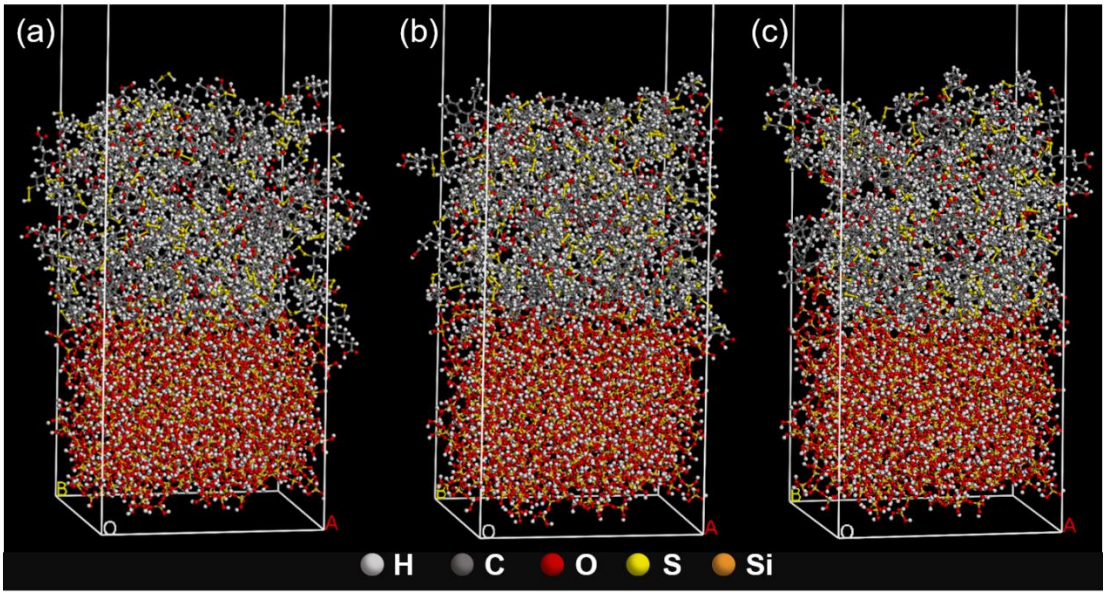

Figure S80. (a) Configurations of molecular models of poly(**TA-A**)$_{8/1}$ clusters (4.0× 4.0×4.0 nm^3) and glass (with $(HO)_3SiOSi(OH)_2OSi(OH)_3$ as model, 4.0×4.0×2.7 nm^3); (b) configurations of molecular models of poly(**TA-B**)$_{8/1}$ (4.0×4.0×4.0 nm^3) and glass (with $(HO)_3SiOSi(OH)_2OSi(OH)_3$ as model, 4.0×4.0×2.7 nm^3); (c) Configurations of molecular models of poly(**TA-D**)$_{8/1}$ (4.0×4.0×4.0 nm^3) and glass (with $(HO)_3SiOSi(OH)_2OSi(OH)_3$ as model, 4.0×4.0×2.7 nm^3).

Table S3. Interaction energy between SPs and glass at 25 °C.

E(kcal/mol) / Adhesive	E_{total}	$E_{adhesive}$	E_{glass}	$E_{interfacial}$
poly(**TA-A**)$_{8/1}$	–43251.7	–32193.3	–10455.8	–602.6
poly(**TA-B**)$_{8/1}$	–43702.9	–32492.1	–10637.1	–573.8
poly(**TA-D**)$_{8/1}$	–41168.9	–29645.4	–10938.7	–584.9

34. Underwater labeling of poly(TA-TPE)s

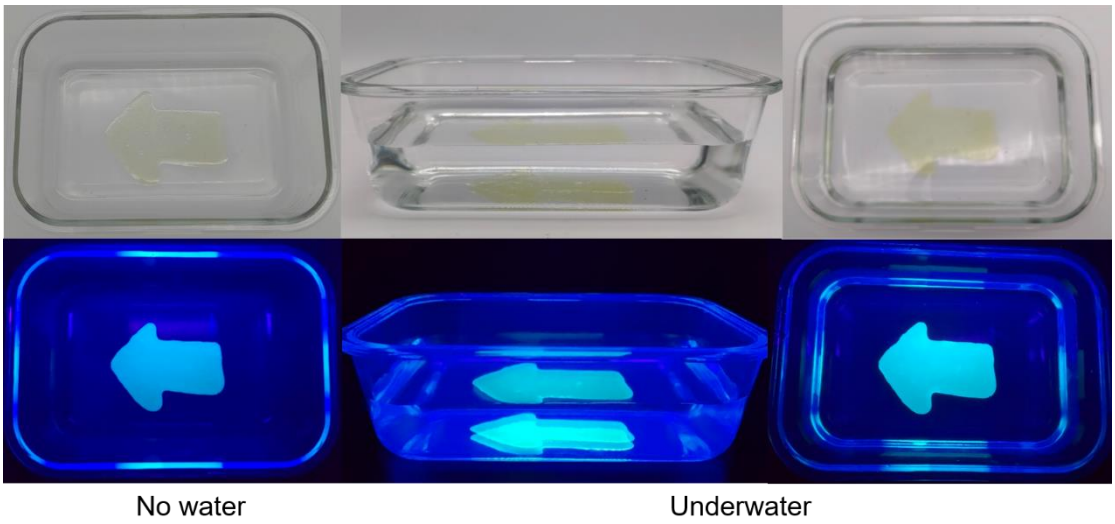

Figure S81. Macroscopic views of poly(**TA-A**)$_{8/1}$ for underwater labeling.

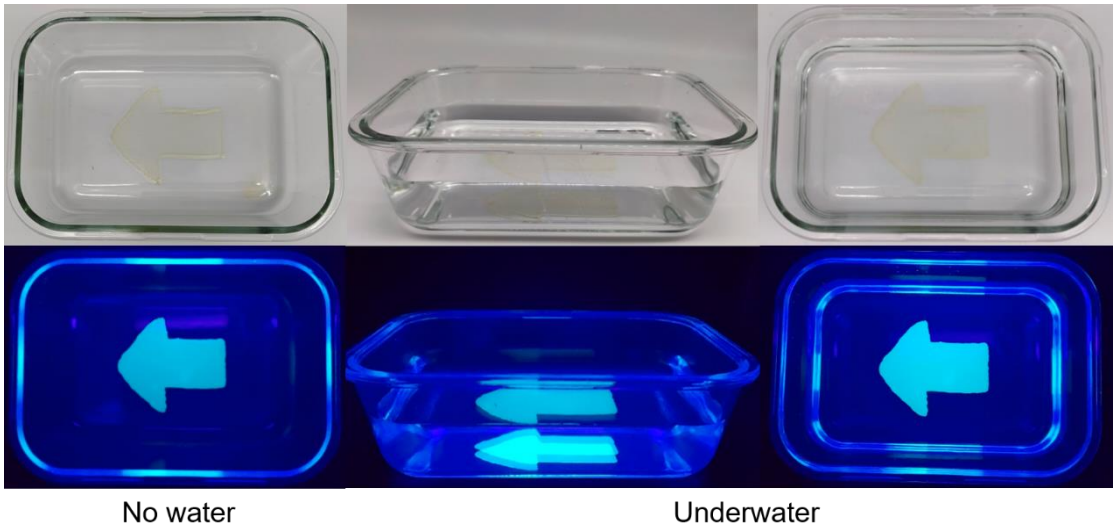

Figure S82. Macroscopic views of poly(**TA**-**B**)$_{8/1}$ for underwater labeling.

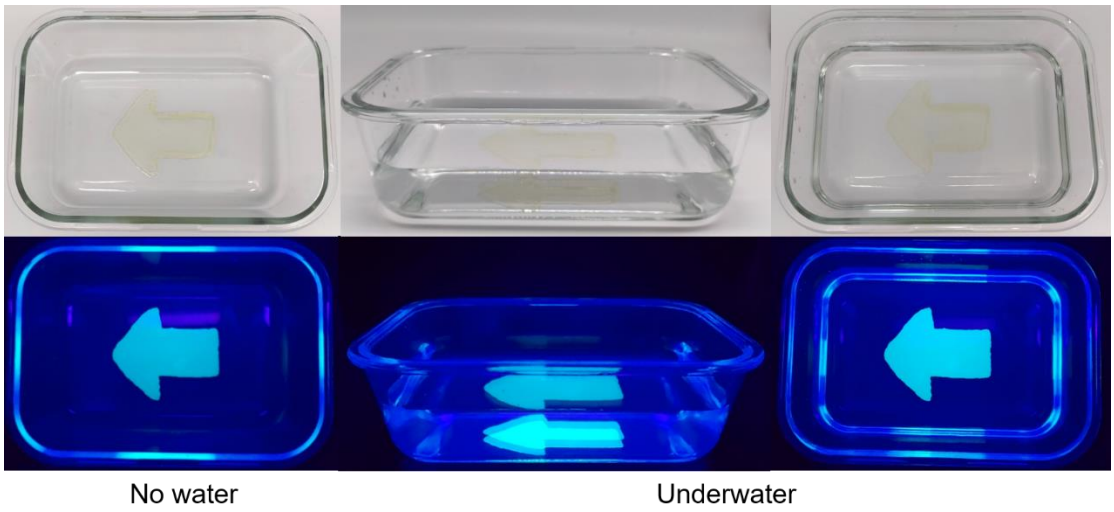

Figure S83. Macroscopic views of poly(**TA**-**D**)$_{8/1}$ for underwater labeling.

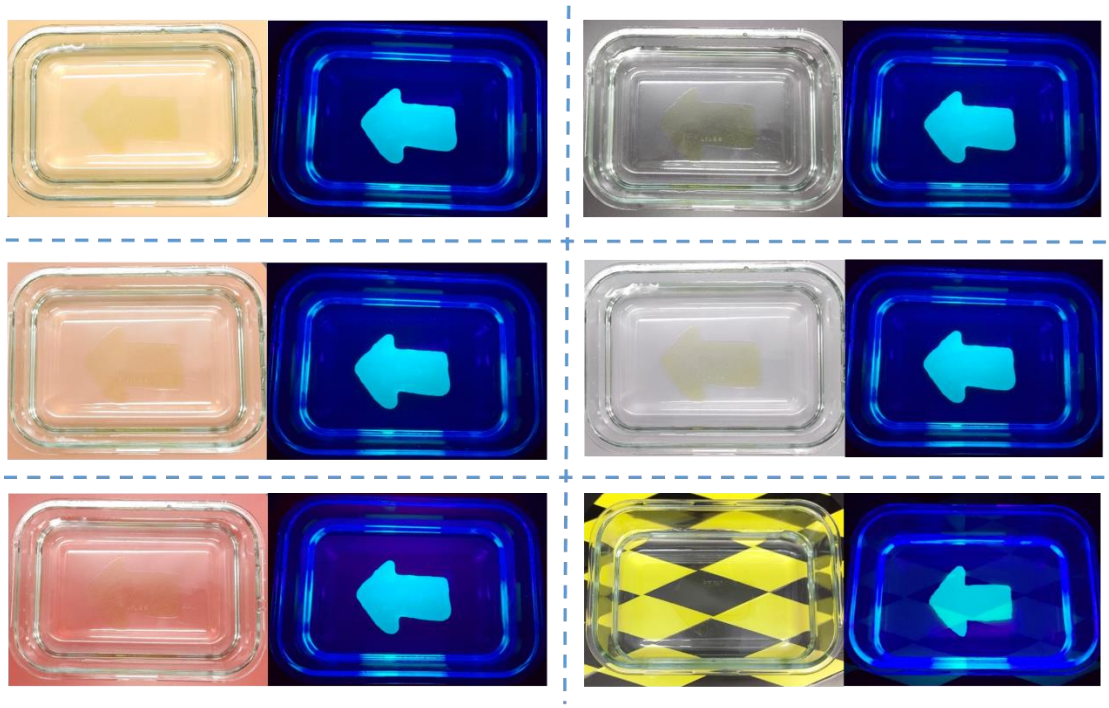

Figure S84. Macroscopic views of poly(**TA**-**A**)$_{8/1}$ above different backgrounds.

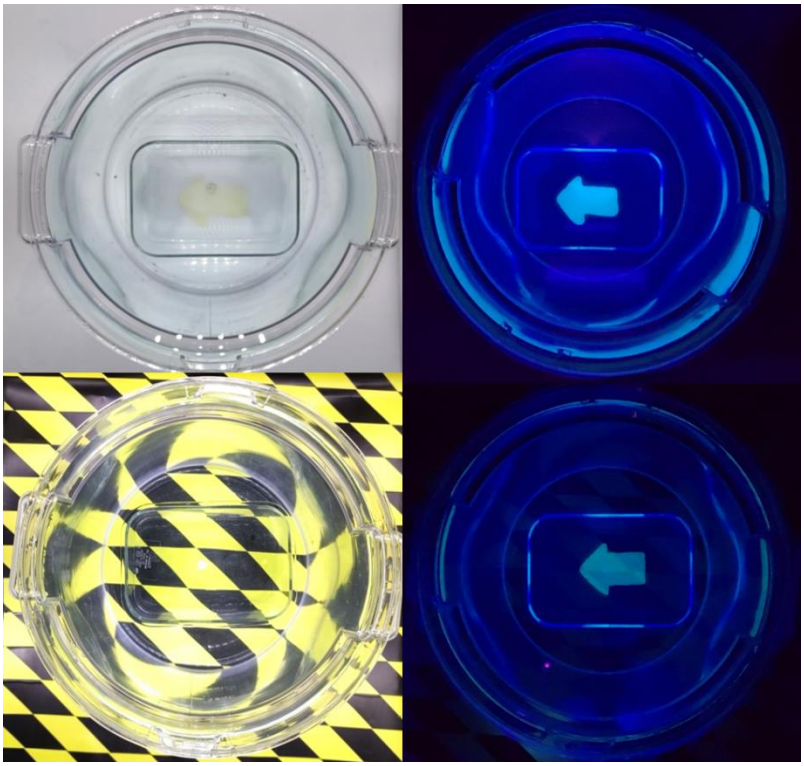

Figure S85. Macroscopic views of poly(**TA**-**A**)$_{8/1}$ in deep water (depth: 0.6 m).

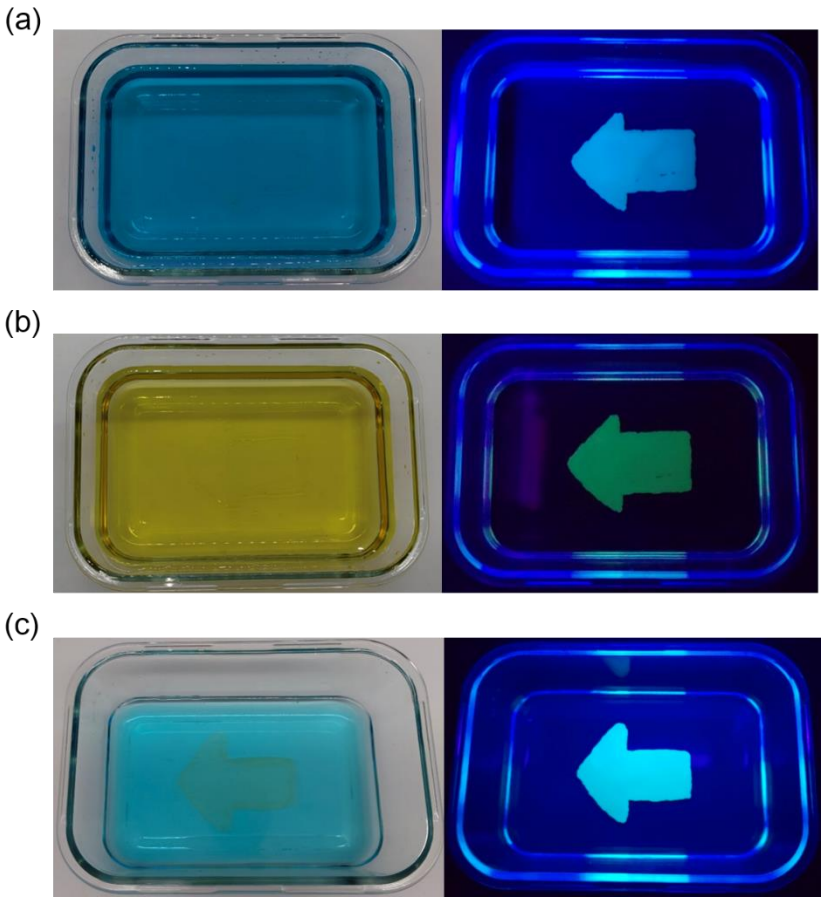

Figure S86. Macroscopic views of poly(**TA**-**A**)$_{8/1}$ in polluted water: (a) methyl blue aqueous solution; (b) methyl orange aqueous solution; (c) $CuSO_4$ aqueous solution.

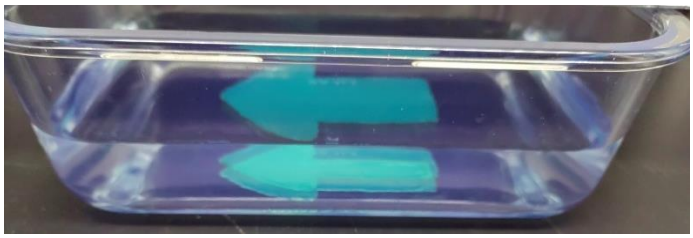

Figure S87. Luminescence of poly(**TA**-**A**)$_{8/1}$ in sunlight

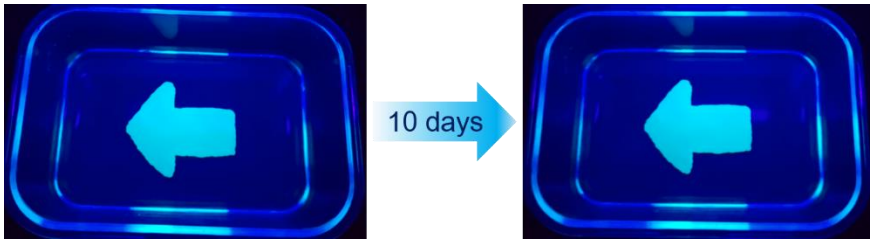

Figure S88. Long-time underwater labeling of poly(**TA**-**A**)$_{8/1}$.

The label can be prepared by coating the ethanol solution of poly(**TA**-**TPE**)s on the substrate to the target shape, and then removing the solvent. The label can be applied to various conditions.

35. Quick response (QR) codes coated with poly(TA-TPE)s

The QR code model of glass was coated with the ethanol solution of poly(**TA**-**A**)$_{8/1}$, and the QR code with luminescence was obtained after the ethanol was evaporated.

Figure S89. Luminescence of QR codes coated with poly(**TA**-**A**)$_{8/1}$ above colorful backgrounds.

Figure S90. Luminescence of QR codes coated with poly(**TA**-**A**)$_{8/1}$ in deep water (depth: 0.8 m).

36. Poly(TA-A)$_{32/1}$ as the coating material of white LEDs (WLEDs)

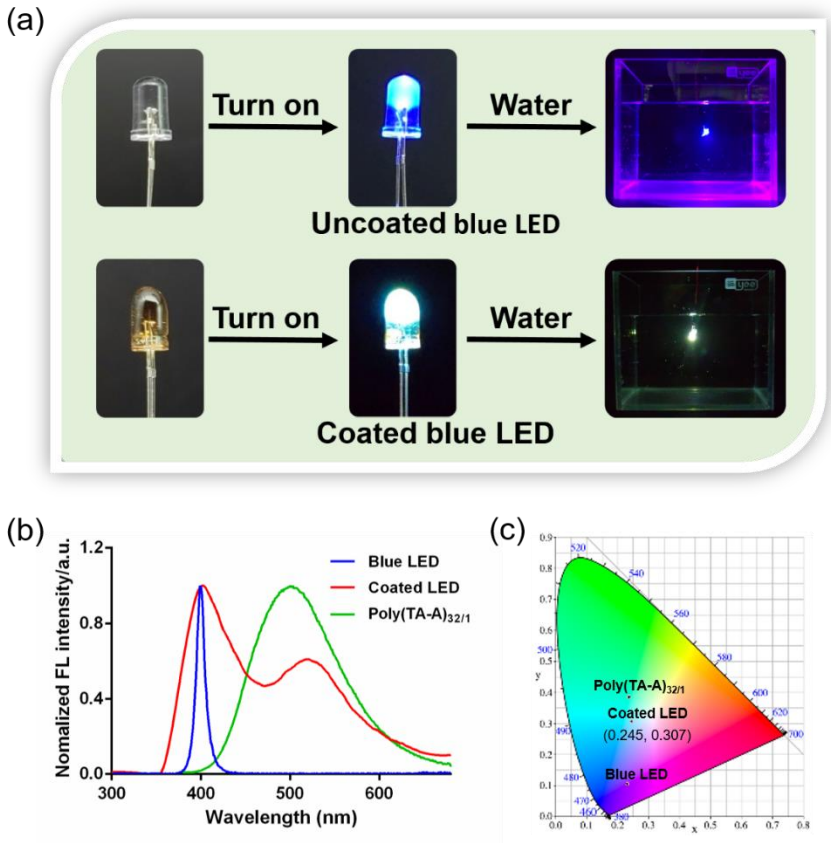

Figure S91. (a) Poly(**TA**-**A**)$_{32/1}$ as the coating to achieve WLEDs, (b) emission spectra of blue LED, coated LED with poly(**TA**-**A**)$_{32/1}$ and poly(**TA**-**A**)$_{32/1}$, (b) their corresponding CIE chromaticity coordinates in solid state.

The emission color of poly(TA-A)$_{32/1}$ is in the green-yellow region (**Figure S91b-c**), which is complementary with blue color. Combining adhesion and luminescent properties, poly(**TA**-**TPE**)s as the coating to achieve white LEDs (WLEDs) (as shown in **Figure S91**). Considering its good thermal processing performance, it was coated on a blue LED bulb to prepare WLEDs (**Figure S91a**). The blue LED bulb was simply immersed in the molten poly(**TA**-**A**)$_{32/1}$ and then a thin and uniform film was formed on the surface of the bulb. When the power (3 V) is turned on, bright white light can be generated. Because poly(**TA**-**A**)$_{32/1}$ has strong adhesion in water, WLEDs can also be applied in water. From the emission spectrum of coated LED with poly(**TA**-**A**)$_{32/1}$, two emission bands centered at 400 nm and 521 nm were found, which covered the entire visible region to produce white light emission (**Figure S91b**). According to the 1931 Commission Internationale deL'Eclairage chromaticity diagram, the coordinate is (0.245, 0.307), locating at the white-light zone.

37. References

[1] X. Ma, I. Pinnau, *Polym*. *Chem*., 2016, **7**, 1244–1248.
[2] M.-K. Chung, G. Qi, J. M. Stryker, *Org*. *Lett*., 2006, **8**, 1491–1494.
[3] R. Krishnan, J. S. Binkley, R. Seeger, J. A. Pople, *J. Chem*. *Phys*., 1980, **72**, 650–654.
[4] S. Grimme, S. Ehrlich, L. Goerigk, *J. Comp*. *Chem*., 2011, **32**, 1456–1465.
[5] H. Fan, J. Wang, J. P. Gong, *Adv*. *Funct*. *Mater*., 2021, **31**, 2009334.
[6] F. Pan, S. Ye, R. Wang, W. She, J. Liu, Z. Sun, W. Zhang, *Mater*. *Horiz*., 2020, **7**, 2063–2070
[7] Z. Wang, S. Zhang, S. Zhao, H. Kang, Z. Wang, C. Xia, Y. Yu, J. Li, *Chem*. *Eng*. *J*., 2021, **404**, 127069.
[8] Z. Wang, L. Guo, H. Xiao, H. Cong, S. Wang, *Mater*. *Horiz*., 2020, **7**, 282–288.
[9] C. Cui, C. Fan, Y. Wu, M. Xiao, T. Wu, D. Zhang, X. Chen, B. Liu, Z. Xu, B. Qu, W. Liu, *Adv*. *Mater*. , 2019, **31**, 1905761.

[10] Z. Wang, J. Zhao, W. Tang, T. He, S. Wang, X. He, Y. Chen, D. Yang, S. Peng, *ACS Appl*. *Mater*. *Interfaces*, 2021, **13**, 3435–3444.
[11] X. Li, Y. Deng, J. Lai, G. Zhao, S. Dong, *J*. *Am*. *Chem*. *Soc*., 2020, **142**, 5371–5379.
[12] L. Han, M. Wang, L. O. Prieto-López, X. Deng, J. Cui, *Adv*. *Funct*. *Mater*., 2020, **30**, 1907064.
[13] L. Xu, S. Gao, Q. Guo, C. Wang, Y. Qiao, D. Qiu, *Adv*. *Mater*., 2020, **32**, 2004579.
[14] L. Gao, S. Ma, L. Bao, X. Zhao, Y. Xiang, Z. Zhang, Y. Ma, Z. Ma, Y.-m. Liang, F. Zhou, *ACS Appl*. *Mater*. *Interfaces*, 2022, **14**, 12684–12692.
[15] H. Sun, *J. Phys*. *Chem*. *B*., 1998, **102**, 7338–7364.
[16] Y. Li, S. Wang, Q. Wang, *Carbon* 2017, **111**, 538–545.